MASTER

Direct numerical simulations of hydrogen addition in premixed turbulent methane-air flames

Wessels, Jeroen T.H.

Award date:
2018

Technische Universiteit
Eindhoven
University of Technology

Department of Multiphase and Reactive Flows

Direct numerical simulations of hydrogen addition in premixed turbulent methane-air flames

Master thesis

Jeroen Wessels - 0778324

Exam committee:

Dr. ir. J.A van Oijen
Dr. ir. R.J.M. Bastiaans
Dr. ir. A.J.H. Frijns

Supervisors:

Dr. ir. J.A van Oijen
S. Karaca MSc

Eindhoven, February 2018

Abstract

By blending small amounts of hydrogen with methane, a flame can burn leaner. As a result the flame temperature and the NO emissions are reduced in laminar premixed flames. Due to the difference in the species diffusion rates, the flame encounters a preferential diffusion effect of hydrogen. Therefore, the methane-hydrogen-air mixture might be locally richer in the positively curved and strained regions of the flame, which results in local higher temperatures. Hence, addition of hydrogen might have a negative impact on NO emissions.

The effects of hydrogen addition to lean premixed turbulent methane-air flames in the thin reaction zone regime is studied by performing direct numerical simulations with detailed chemistry. Hydrogen is blended to methane at a level of 40% by volume and premixed with air in a lean environment of $\phi = 0.7$. The case of pure methane is used as reference case. The DNS code is developed by [2, 37, 16], where a constant Lewis number approach is used to model transport of species. Simulations are performed in a two- and three-dimensional domain, which consist of a cold turbulent fuel/air core surrounded by a hot stream of burnt products flowing with a velocity difference. This velocity difference creates Kelvin-Helmholtz instabilities which triggers mixing between the layers.

The turbulent flames are compared with respect to flame stability, preferential diffusion effects and NO formation. It is shown that the effect of turbulence to the turbulent burning velocity per unit area in the results of the three-dimensional simulations agree well with the results of two-dimensional simulations. It is seen that the turbulent burning velocity per unit area of the hydrogen-enriched flame is enhanced due to preferential diffusion effects. Flame stability is analyzed in terms of sensitivity of the mass burning rate to flame stretch. The relation between the change of mass burning rate to flame stretch is captured by the Markstein number. It was found that the hydrogen-enriched case resulted in a decrease of the Markstein number and thus a less stable flame. However, due to the turbulent environment this decrease was weaker than for the steady laminar flame. Furthermore, the hydrogen-enriched flame showed an increase in NO emissions in the positively curved regions in the flame. As a result the amount of NO produced in the methane-hydrogen-air flame is enhanced compared to the methane-air flame. However, this might be offset by the ability to burn leaner.

Contents

List of symbols

English symbols		
A	Flame surface area	-
a_t	Strain rate	s^{-1}
C	Courant number	-
c	Traveling velocity of acoustic waves	m s^{-1}
c	Normalized temperature	-
c_p	Specific heat capacity at constant pressure	J (kg K)^{-1}
$c_{p,i}$	Specific heat capacity at constant pressure of specie i	J (kg K)^{-1}
$\mathcal{D}_{ij}$	Binary diffusion coefficient of species i and element j	$\text{m}^2 \text{ s}^{-1}$
D_{ij}	Generalized diffusion coefficient of species i and element j	$\text{m}^2 \text{ s}^{-1}$
D_{im}	Mixture averaged diffusion coefficient	$\text{m}^2 \text{ s}^{-1}$
D_i^T	Thermal diffusion coefficient of specie i	kg (m s)^{-1}
E_a	Activation energy	J mol^{-1}
h	Specific enthalpy	J kg^{-1}
h_i	Specific enthalpy of specie i	J kg^{-1}
$h_{i,ref}$	Specific enthalpy of formation of species i	J kg^{-1}
I	Turbulent intensity	-
I	Turbulent influences on s_T per unit area	m^{-1}
K	mass-based flame stretch rate	s^{-1}
K_A	area-based flame stretch rate	s^{-1}
Ka	Karlovitz number	-
Ka_i	Karlovitz integral	-
Le	Lewis number	-
Le_i	Lewis number of specie i	-
L_T	Integral length scale	m
L_x	Length in x-direction	m
L_y	Length in y-direction	m
l_δ	Thickness of reaction layer	m
M	Mass contained in volume element	kg
m	Mass	kg
M_i	Molar mass of species i	kg mol^{-3}
$\overline{M}$	Average molar mass	kg mol^{-3}
$\mathcal{M}$	Markstein number	(-)
$\mathcal{M}_i$	species i in reaction j	(-)
n	Number of moles	-
N_s	Number of species	-
N_e	Number of elements	-
p	Pressure	Pa

Q_i	Unsteady effects in reference frame and diffusive transport processes along the flame front of specie i	kg m^{-3} s^{-1}
Re_T	Turbulent Reynolds number	-
$\mathcal{R}$	Universal gas constant	J (mol K)$^{-1}$
R_i	Gas constant of specie i	J (mol K)$^{-1}$
r	Reaction rate	mole m^{-3} s^{-1}
s	Arclength coordinate along flamelets	m
s_i	location of the inner layer	m
s_L	Laminar burning velocity	m s^{-1}
s_d	Flame displacement speed	m s^{-1}
s_T	Turbulent burning velocity	m s^{-1}
t	Time	s
t_L	Large eddy turnover time	s
T	Temperature	K
T_{ad}	Adiabatic flame temperature	K
u	Velocity in streamwise direction	m s^{-1}
u'_{rms}	root mean square of velocity fluctuations	m s^{-1}
$\overline{u}$	mean velocity in streamwise direction	m s^{-1}
ΔU	Velocity difference in streamwise direction	m s^{-1}
V	Volume	m^3
v'	velocity fluctuations in transverse direction	m s^{-1}
$w_{j,i}$	mass fraction of element j in species i	-
x	Cartesian coordinate	m
X_i	Mole fraction of species i	-
y	Cartesian coordinate	m
$\mathcal{Y}$	Progress variable	-
Y_i	Mass fraction of species i	-
z	Cartesian coordinate	m
Z_j	Element mass fraction of element j	-

Greek symbols

δ_f	thermal flame thickness	m
δ	spacial resolution	m
ϵ	Dissipation rate	m^2 s^{-3}
η	Kolmogorov length scale	m
κ	Curvature	m^{-1}
λ	Thermal conductivity	W (m K)$^{-1}$
μ	Dynamic viscosity	kg (m s)$^{-1}$
ν	Kinematic viscosity	m^2 s^{-1}
$\nu_{k,l}$	Stoichiometric number of moles of species k in reaction l	-
ρ	Density	kg m^{-3}
σ	Factor of area elements at flame surfaces	(-)
τ_f	Characteristic flame time scale	-
ϕ	Equivalence ratio	-
ψ	Enthalpy and element mass fraction vector	-
$\dot{\omega}_i$	Source term of species i	kg m^{-3} s^{-1}

Vectors and tensors

$\mathcal{D}_b$	Diffusion flux of $\mathcal{Y}$	kg m^{-2}s^{-1}

$\boldsymbol{J}_F$	Diffusion flux of one single specie	kg m^{-2}s^{-1}
$\boldsymbol{J}_T$	Diffusion flux of thermal energy	W m^2
$\boldsymbol{I}$	Unit tensor	-
$\vec{n}$	Unit normal vector	-
$\boldsymbol{\tau}$	Stress tensor	Pa
$\vec{V}_i$	Diffusion velocity of species i	m s^{-1}
$\vec{v}$	fluid velocity	m/s
$\vec{v}_f$	Velocity of flame surface	m/s
$\vec{q}$	Heat flux vector	W m^2
$\vec{x}$	Cartesian space coordinates	m

Subscript

b	at the burnt side of the flame front	-
i	at the inner layer	-
j	element j	-
0	at initial conditions	-
u	at the unburnt side of the flame front	-
$\|\|$	tangential to the flame front	-

Superscript

0	Stretchless reference condition	-

Chapter 1

Introduction

Introduction

Combustion is vital in our daily life as our main source of energy. Combustion processes are present in major industrial systems for power generation, transportation industry and in house-hold applications for heating. The growing energy demand and the changing climate requires the need of more efficient combustion processes that lead to lower emissions and reduce the fuel consumption. Lean premixed combustion has the potential to produce power with low emissions of oxides of nitrogen (NO_x) due to the relative low flame temperatures. In most industrial applications the combustion occurs in the turbulent regime, which leads to the importance to study turbulent lean premixed flames.

One of these industrial applications are power plants, which generate energy by burning natural gas in a gas turbine. Usually gas turbines operate in a turbulent lean premixed combustion mode. Natural gas consists mainly out of methane (CH_4). To further reduce the NO_x emissions and thus flame temperature, methane must be burned leaner close to the lean flammability limit [40]. As a result the flame is more sensitive to the turbulent flow. This may lead to local extinction and quenching that can result in elevated levels of carbon monoxide (CO) and unburned hydrocarbons (UHC). In addition, the combustion efficiency is reduced due to incomplete combustion. To avoid these problems small amounts of hydrogen can be added to the fuel.

Adding hydrogen to the methane-air mixture has the potential to extend the lean operating limit and enhance the flame stability [19, 20, 15]. However, a light specie as hydrogen has a much higher mass diffusion velocity compared to heat diffusion velocity. Moreover, each specie in the flame has a different diffusion rate (preferential diffusion). Turbulent flow structures cause the flame to be curved and stretched. This results in a redistribution of heat and stoichiometry in the flame and therefore a change in flame temperature, which has a large influence on the flame structure and behaviour. Besides the flame influences the flow due to expansion in the flame. These local changes influences the local mass burning rate, which can lead to unstable flame [11]. In order to operate a gas turbine efficiently with reduced emissions and to control flame stability, fundamental understanding of the effects of replacing a part of natural gas by hydrogen is required .

For a methane-air flame the mass diffusion and heat diffusion rate do not differ much. However, when the highly diffusive specie hydrogen is added to the methane-air mixture, the flame encounters a preferential diffusion effect of hydrogen due to flame stretch in a turbulent flow [26, 38]. In some regions the mixture is locally richer, which increases the burning velocity and temperature of the flame. Therefore, addition of H_2 might have a negative impact on NO_x emissions due to local higher flame temperatures [31]. However, this may be offset by the ability to burn in an leaner environment.

Interactions of preferential diffusion and the influence of turbulence on the flame make it useful to study the flame behaviour of turbulent premixed CH_4-H_2 flames. For fundamental investigations the interaction between small scale flow structures and the flame are important. Therefore all scales in the flow have to be solved by using Direct Numerical Simulation (DNS). The DNS has high computational costs, since a fine grid is required to solve for all flow scales. Furthermore, all species are necessary to model the preferential diffusion effect accurately. This means that a transport equation is solved for each specie, which is often referred to as detailed chemistry. In this way the individual diffusion rates of each specie is included. However, a detailed chemical reaction mechanism consists of many species and reaction. As a result a large number of equations need to be solved.

Therefore, the combination of DNS with detailed chemistry is not feasible in simulations of industrial applications in which combustion takes place. Though theoretical understanding can be gained by performing DNS simulations in an academic case setup of turbulent mixing layers. In this thesis the fundamental behaviour of turbulent methane-hydrogen-air flames are studied using DNS.

Objective

The objectives of this study are to investigate

- the impact of mixing hydrogen with methane-air on preferential diffusion.

  Performing simulations of flame turbulence interaction reveals preferential diffusion effects. The results from simulations of two methane-air mixtures with and without hydrogen addition are compared.

- the effect of hydrogen-addition to the methane-air flame on the NO formation.

  A study is performed on the effect of hydrogen in the fuel on NO formation in turbulent flames. This shows the influence of preferential diffusion on NO formation. This is done by performing simulations with two different turbulent intensities in order to study the interaction between turbulent intensity and the generated flame area, which enhances NO formation.

- the influence of preferential diffusion on the local mass burning rate and flame stability.

  The local mass burning rate changes due preferential diffusion and this affects the stability of the flame. The flame stability is analysed in terms of sensitivity of mass burning rate to flame stretch.

Outline

In the following Chapters these research question are answered. In the second Chapter an introduction to combustion is given, where flame stretch and preferential diffusion are explained. After that the conservation equations solved by DNS are presented followed by an introduction of laminar methane-hydrogen-air flames using the 1D flamelet code CHEM1D [35]. In Chapter 3 the DNS code is introduced. This code will be used to simulate turbulent flames. The geometry is presented and the code is validated by performing simulations of laminar flames. After that the turbulent case setup is given.

Then, in Chapter 4 the flame turbulence interaction is investigated by comparing the two fuel-air mixtures in terms of turbulent burning velocity, generated flame surface area and NO formation. It is shown that the two-dimensional case results are fairly accurate compared with the three-dimensional cases. Therefore, the 2D results are used in the remainder of the thesis. After that,

results from simulations at different turbulent intensity levels are given. It is shown that higher turbulent intensities results in more flame surface area. Finally, the influence of hydrogen addition on NO formation is investigated.

In Chapter 5, the flame stretch and stability effects are investigated of turbulent flames. First the strong stretch theory of De Goey and Ten Thije Boonkkamp [8] is introduced. It is shown that the theory relates the mass burning rate with the mass burning rate of an unstretched flame and the dimensionless stretch rate. After that, an expression is derived for weakly stretched flames. The accuracy of the model is compared with weakly stretched laminar one-dimensional flames using CHEM1D. Afterwards, turbulent flamelets are extracted from the DNS solutions and investigated. It is shown that hydrogen addition results in a different response of the mass burning rate to flame stretch, which affect flame stability.

Finally, the conclusions and recommendations are given.

Chapter 2

Background

In this chapter an introduction to turbulent combustion is given. First, the basis of combustion are explained followed by an introduction to flame stretch and preferential diffusion effects. After that, the effect of hydrogen addition to stretched one-dimensional methane-air flames are presented. Finally, the relevant equations describing the combustion process are given.

2.1 Turbulent combustion

Combustion is the process where fuel is oxidized by a large set of exothermal chemical reactions. First, the fuel breaks up into smaller molecules. Several intermediate species are formed and subsequently consumed again. In the end, the final products are formed. The heat released is usually enough to keep the combustion of fuel and air to proceed. All the reactions together results in a global reaction equation. For the combustion of methane with air, this results in the following global reaction equation

$$CH_4 + 2\,O_2 \rightarrow 2\,H_2O + CO_2, \tag{2.1}$$

where nitrogen N_2 present in air is neglected, since it does not participate in the basic reaction. However, nitrogen reacts with oxygen O_2 at high temperatures present in the flame and forms a relative small amount of NO.

Combustion can take place in different forms depending on the flow type and the type of mixing. There are two types of flames categorized on the type of mixing: premixed and non-premixed (or diffusion) flames. A premixed flame is a flame where the fuel and oxidizer are premixed and burned. The time scale at which the reactions occur in a premixed flame is the chemical time scale. The combustion process is controlled by the initial temperature, T_u, pressure p_u and the equivalence ratio, ϕ of the initial mixture of fuel and oxidizer. The equivalence ratio is defined as the ratio fuel-to-oxidizer ratio to the stoichiometric fuel-to-oxidizer ratio

$$\phi = \frac{m_{fuel}/m_{ox}}{(m_{fuel}/m_{ox})_{st}} = \frac{n_{fuel}/n_{ox}}{(n_{fuel}/n_{ox})_{st}}, \tag{2.2}$$

where m represents the mass and n the number of molecules of fuel and oxidiser. The combustion is stoichiometric when the equivalence ratio is one. The global reaction equation 2.1 is an example of stoichiometric combustion of methane. If the equivalence ratio is smaller than one, the combustion occurs with an excess of air. This is called lean combustion. The global reaction equation of lean combustion with $\phi = 0.7$ for the combustion of methane with air can be given as

$$CH_4 + 2.85\,O_2 \rightarrow 2\,H_2O + CO_2 + 0.85\,O_2. \tag{2.3}$$
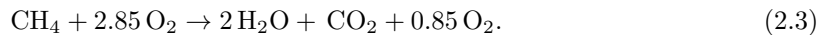
If the equivalence ratio is larger than one, the combustion is rich and incomplete. Hence, fuel is left after combustion. In this thesis we focus on lean combustion of methane and hydrogen with premixed with air.

A premixed flame can be divided in three zones. This is indicated in Figure 2.1, where the preheating zone, the reaction layer (inner layer), and the oxidation layer of a premixed methane-air flame with $\phi = 0.7$ is shown. In the preheating zone almost no reactions take place and the cold unburned gas is preheated by the flame. As a result the temperature increases in the preheating zone, which can be seen in Figure 2.2. Chemical reactions take place in the inner layer and the unburned mixture starts to break up into other species. Finally, the slower reactions are taken place in the oxidation zone, where the final products are formed. A typical reaction in this zone is the oxidation reaction from CO to CO_2. The location of the inner layer s_i is defined as the position in the flame where the chemical source term $\dot{\omega}_{CH_4}$ is maximal. The chemical source terms of the major species are given in Figure 2.3. It can be seen that the maximum of the chemical source term $\dot{\omega}_{CH_4}$ is positioned at $s = s_i$, which is close to the burnt side of the flame and close to the location of maximum heat release. Furthermore, it can be seen that CO is an intermediate species. The chemical source term of CO is first positive. Hence, CO is created and it appears in the reaction layer in Figure 2.1. Further downstream in the flame, the chemical source term of CO becomes negative. As a result the species CO is consumed.
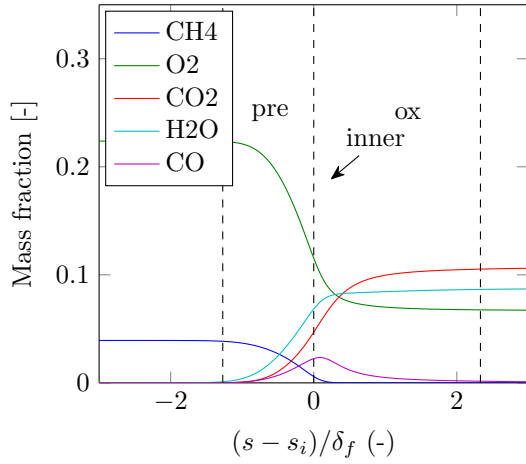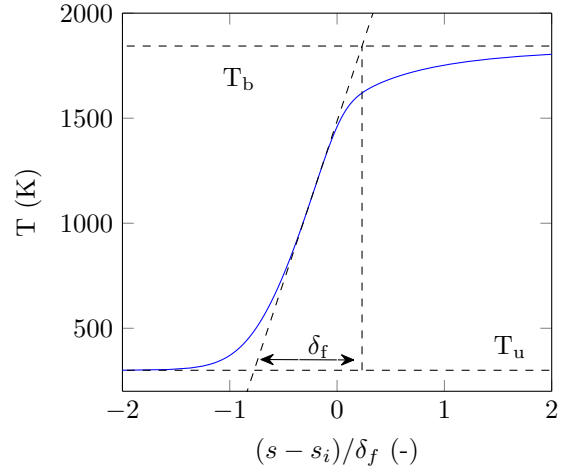

Figure 2.1: Structure of a premixed flame
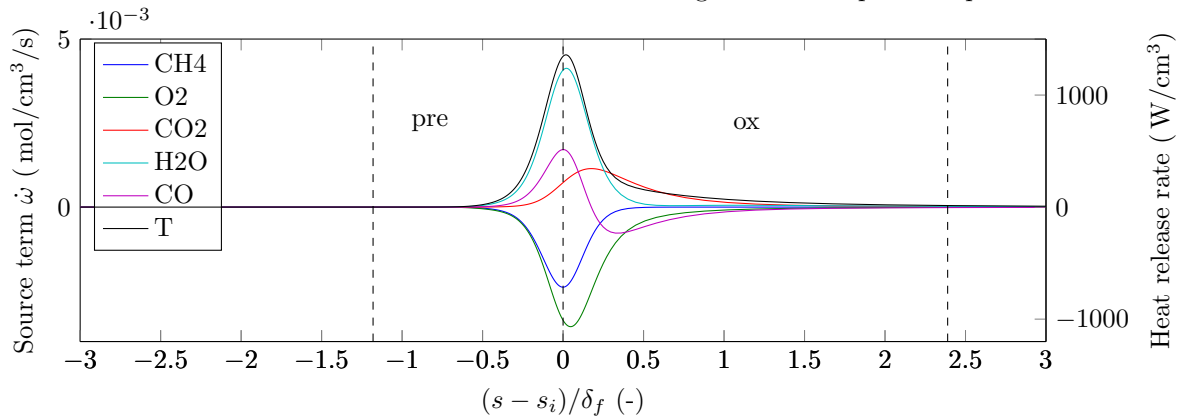

Figure 2.2: Temperature profile

Figure 2.3: Source terms in a premixed flame

The thermal flame thickness δ_f is defined as

$$\delta_f = \frac{T_b - T_u}{|\partial T / \partial s|_{max}},\tag{2.4}$$

where T is temperature, s is the coordinate in the flame and T_b indicates the burnt temperature. At the burnt side of the flame all variables no longer changer. In Figure 2.2 the temperature profile in the flame is presented. The maximum gradient of the temperature is displayed, which is used to define the flame thickness. Another property of premixed combustion is the unstretched adiabatic burning velocity s_L^0, which is the speed the flame will propagate through a premixed mixture. The adiabatic burning velocity for a laminar flame is a function of the conditions of the unburnt mixture, $s_L^0 = s_L^0(p_u, T_u, \phi)$. Whether a flame is laminar or turbulent depends on the length and time scales in the flame front and the flow field. To categorize the different regimes in premixed flames the Borghi diagram can be used [28].
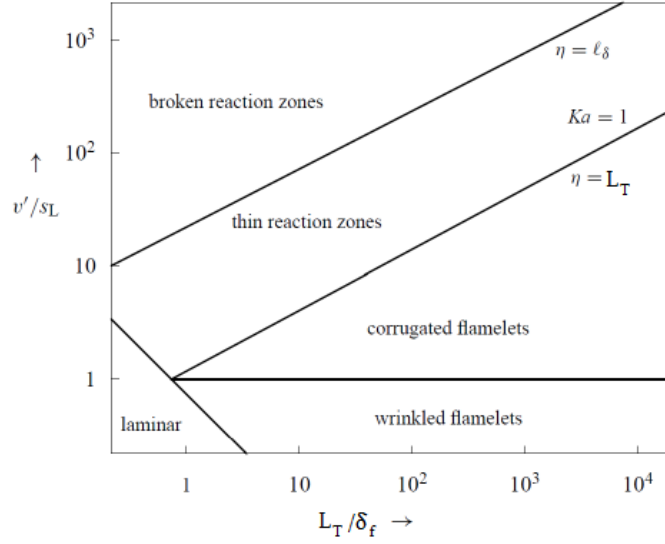

Figure 2.4: Borghi-diagram for premixed combustion [28]

The combustion regimes are in this diagram defined in terms of the ratio of the velocity scales, v'/s_L and length scales L_T/δ_f. It can be seen that for small velocity fluctuations v' compared to the adiabatic burning velocity and for smallest flow structures L_T compared to the flame thickness δ_f the flame is laminar. If $L_T/\delta_f > 1$ and $v'/s_L < 1$, the wrinkled flamelets regime is entered and the laminar flame front is wrinkled by the turbulent flow. If the velocity fluctuations are increased above the adiabatic burning speed, $v'/s_L > 1$, the burning velocity can no longer smoothen the fluctuations and the corrugated flamelets regime is entered. Further increasing the fluctuations lead to the thin reaction zone, where the smallest eddies in the flow with length η become smaller than the flame thickness. The combustion takes place in the reaction layer, which has a thickness l_δ that is an order of magnitude smaller than δ_f. In the thin reaction zone regime the smallest flow structures are larger than the reaction zone thickness, the eddies cannot penetrate the reaction layer and this remains undisturbed. When the flow structures become smaller, eddies can penetrate the reaction zone and the combustion takes place in the broken reaction zone regime.

2.2 Flame stretch

Flame stretch is an important property that can influence the burning speed, shape and stability of a premixed flame. In this section two different definitions of flame stretch are discussed. The definition of flame stretch by Chung and Law [3] is based on an infinity thin flame assumption. Hence, flame stretch can be defined as the fractional rate of change of area of an infinitesimal surface element of the flame surface A, derived by Chung and Law [3]

$$K_A = \frac{1}{A}\frac{dA}{dt} = \nabla \cdot \vec{v}_{||} + (\vec{v}_f \cdot \vec{n})\nabla \cdot \vec{n}, \tag{2.5}$$

with $\vec{v}_{||}$ the tangential component of the flow velocity, $\vec{v}_f$ the flame velocity and $\vec{n}$ the unit normal vector to the flame front. The first term represents stretch due to flow straining and the later due to unsteady flame curvature. In Figure 2.5 stretch caused by flow straining and curvature of a moving flame front is presented. It can be seen that in case of a strained flow, the flow velocity $\vec{v}$ change along the flame sheet. Hence, it can be split in a component $\vec{v}_{||}$ parallel to the flame front and a component perpendicular to the flame $(\vec{v}_f \cdot \vec{n})\vec{n}$. Flow straining is assumed positive when a diverging flow impacts on the flame, as shown in Figure 2.5. A curved flame contributes to stretch when to flame surface is moving $(\vec{v}_f \neq 0)$. An expanding spherical flame results in a positive stretch rate.
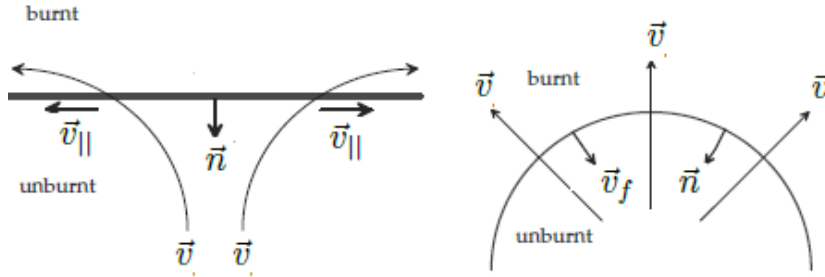

Figure 2.5: Flow straining (left), curvature (right) of an infinitely thin flame sheet. The arrows represent the flow and the thick black lines indicates the moving flame sheet. This figure is directly taken from de Swart [11].

The second definition of flame stretch assumes a finite flame thickness and is derived by De Goey and Ten Thije Boonkkamkp [8]. This definition is based on a flame volume element $V(t)$ instead of an small surface area element. In Figure 2.6 such a small volume in the flame area is displayed. De Goey and Ten Thije Boonkkamp derived the following expression for flame stretch rate

$$K = \frac{1}{M}\frac{dM}{dt}, \tag{2.6}$$

where M is the mass contained in control volume $V(t)$ moving with the flame velocity $\vec{v}_f$ in the flame region, given by

$$M(t) = \int_{V(t)} \rho dV. \tag{2.7}$$

In this definition stretch is no longer related to the change of flame surface area as in Equation 2.5, but is responsible for the change of mass along flame paths. By following the derivation of De Goey en Ten Thije Boonkkamp [8], where Reynolds' transport theorem is applied, the rate of change of mass can be written as

$$\frac{dM}{dt} = \int_{V(t)} \partial\rho/\partial t + \nabla \cdot (\rho\vec{v}_f)dV = \int_{V(t)} \rho K dV. \tag{2.8}$$

Substituting the relation $d\rho/dt = \partial\rho/\partial t + \vec{v}_f \cdot \nabla\rho$ in Equation 2.8, results in

$$K = \frac{1}{\rho}\frac{d\rho}{dt} + \nabla \cdot \vec{v}_f. \tag{2.9}$$

The flame velocity can be decomposed in a component normal and tangential to the flame front, $\vec{v}_f = (\vec{v}_f \cdot \vec{n})\vec{n} + \vec{v}_{||}$. Hence, the mass-based flame stretch definition can be written as

$$K = \nabla \cdot \vec{v}_{||} + (\vec{v}_f \cdot \vec{n})\nabla \cdot \vec{n} + \vec{n} \cdot \nabla(\vec{v}_f \cdot \vec{n}) + \frac{1}{\rho}\frac{d\rho}{dt}, \tag{2.10}$$

where ρ is the density. Compared to the stretch definition in Equation 2.5, this mass-based stretch definition has also included a third and fourth term, which denotes the flame stretch due to flame thickness variations and the density variations with respect to time [11].

Due to flame stretch, the mass in a volume element parallel surrounding the flamelet (1D flame path) is not conserved. Positive stretch results to mass leaking out the volume element. This can be seen in Figure 2.6, where a positive strained flame is presented. The blue lines indicate different iso-levels of a progress variable $\mathcal{Y}$ enclosed by a red-dashed volume element. The combustion of fuel with air in the reaction layer leads to a diffusion flux $\mathcal{D}_b$ of $\mathcal{Y}$ from the reaction layer into the preheating layer. Furthermore, the diffusion flux of fuel from the preheating layer to the reaction zone is indicated with J_F and J_T represents the thermal diffusion flux of heat. For equal thermal J_T and mass diffusivity fluxes J_F, the enthalpy and stoichiometry do not change. As a result flame temperature T_{ad} and fuel consumption rate inside the reaction layer remain unchanged. Therefore, the diffusion flux $\mathcal{D}_b$ of $\mathcal{Y}$ attains the same. Because of the diverging flow field, mass is leaking out of the volume element. Hence, the mass burning rate $m = \rho s_L$ is decreased in the flamelet [26]. The flame encounters then a direct stretch effect, which is the effect of mass loss along flame path. It occurs even if the flame temperature and element composition stay the same.
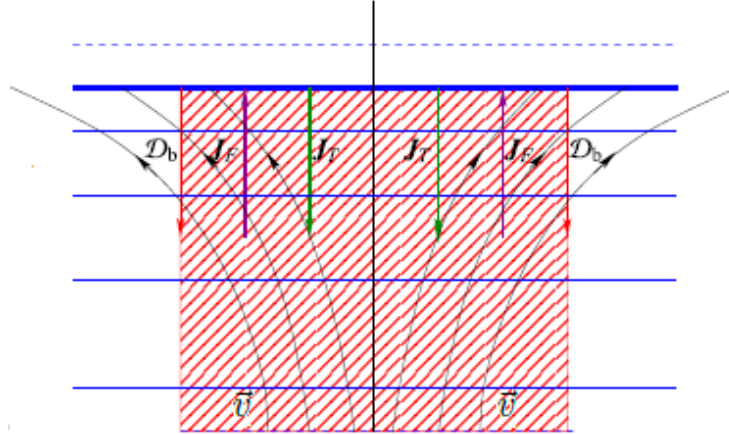

Figure 2.6: Flat flame in strained flow with unity Lewis numbers. The red-dashed area is the volume element. The blue thin lines are the iso-contour levels of $\mathcal{Y}$ and black the flow stream lines. The blue thick line represents the reaction layer. This figure is directly taken from van Oijen [26].

Thermal-diffusive effects and preferential diffusion

Thermal-diffusive effects occur when the mass diffusivity and the thermal diffusivity fluxes are not equal. The Lewis number, Le, is a dimensionless number defined as the ratio of thermal diffusivity flux $\boldsymbol{J}_T$ and mass diffusivity flux $\boldsymbol{J}_F$, given by

$$Le = \frac{\boldsymbol{J}_T}{\boldsymbol{J}_F}. \tag{2.11}$$

A unity Lewis number means the mass diffusivity and thermal diffusivity fluxes are equal. In a mixture with a non-unity Lewis number the diffusive fluxes are of unequal magnitude. In stretched flames ($K \neq 0$, $Le \neq 1$) the amount of mass leaking away due to direct stretch is the same. However, the difference in diffusivity fluxes give rise to a difference of enthalpy and element composition in the preheating zone. Due to flame stretch the enthalpy and elements are no longer conserved in a flamelet.

This can be seen in Figure 2.7, where the enthalpy in a flamelet is presented. It can be seen that no local deviations arise for flames with unity Lewis numbers. However, for non-unity Lewis numbers the enthalpy locally differs within the flamelet. In case of unstretched flames the enthalpy is conserved within the flamelet ($h_u = h_b$), but enthalpy is lost within the flamelet for positive stretched flames ($h_b < h_u$). Note that enthalpy is always conserved in the flame, the enthalpy lost/gained in one flamelet is gained/lost in the neighbouring flamelets. The same results apply for element composition. Figure 2.8 shows the element mass fraction H as function of the flame path. It can be seen that for non-unity Lewis numbers the element composition differs within the flamelet. For positively stretched flames this results in more H elements in the flamelet. As a result the mixture is richer, the flame temperature increases and therefore also more mass of fuel is consumed in the flame front. The flame encounters then a preferential diffusion effect besides the direct stretch effect.
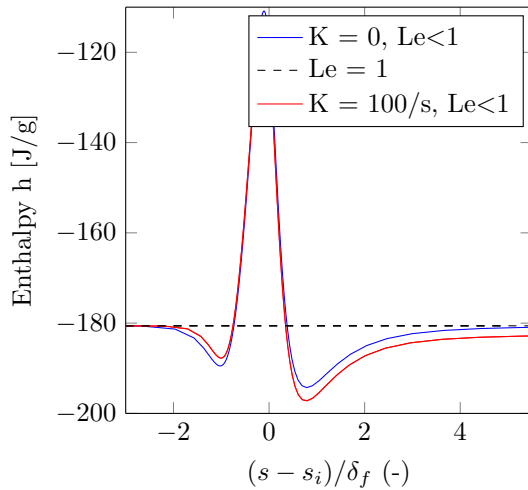

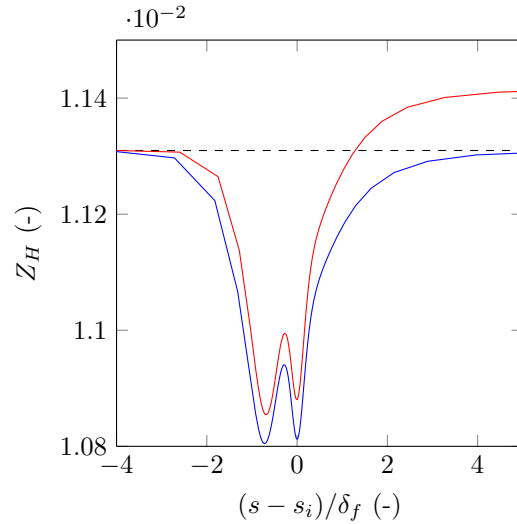Figure 2.7: Local enthalpy h in the flame

Figure 2.8: Element mass fraction H in the flame

In Figure 2.9 the case of a mixture with non-unity Lewis number with a curved flame front in a homogeneous flow is presented. The flame is stretched, since a curved flame front introduces a non-homogeneous flow component along the flame front. The left and right flamelet are respectively negatively and positively stretched. Hence, mass is gained in the left flamelet and lost in the right flamelet due to the direct stretch effect. The two diffusive fluxes $\boldsymbol{J}_F$ and $\boldsymbol{J}_T$ have a different magnitude ($Le > 1$), resulting in a local increase of enthalpy in the preheating zone of a flamelet. The enthalpy and elements are not conserved in the flamelet. The non-homogeneous

flow parallel to the flame front is responsible for the change of enthalpy and elements flowing in or out the volume element. This results in an increase of enthalpy and a temperature above the adiabatic flame temperature in the left flamelet and decrease of enthalpy and temperature in the right flamelet.
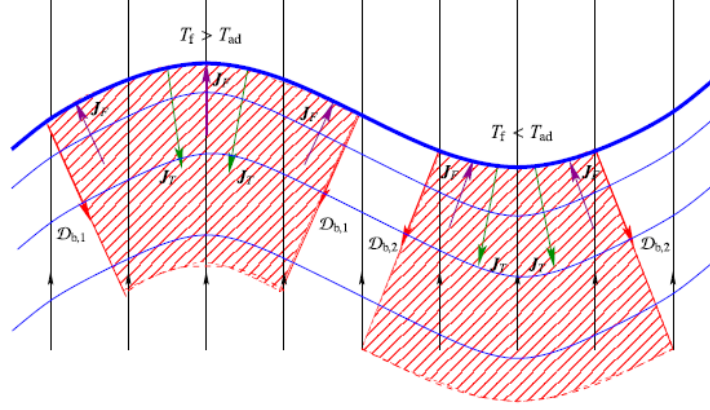

Figure 2.9: Curved flame with non-unity Lewis number. The red area represents a volume element around a flamelet. The blue lines are iso-contour levels and the thick blue represents the flame front. The black lines are the flow streamlines. The figure is taken from [26].

This effect of a redistributing of enthalpy and elements in a flame is called preferential diffusion, which results for $Le > 1$ in an increase of the local burning velocity in the left flamelet where the flame is negatively stretched, while it is decreased in regions of positive stretch as shown in the right flamelet. When the Lewis number of the fuel is smaller than one, positive stretch increases the local burning velocity s_d and negative stretch decreases the local burning velocity s_d. The sensitivity of the response of the mass burning rate (ρs_d) on flame stretch is important for the flame stability. In Chapter 5 of more detailed analyses of flame stretch and stability is performed with the mass-based stretch definition.

2.3   Governing equations

The physics of turbulent flames can be described by governing equations of fluid dynamics and of chemical composition. The non-reacting part can be described by the conservation equations for mass m, velocity $\vec{v}$ and enthalpy h. The reacting part is described by a conversation equation for each species i. This system of equations is completed by an equation of state for pressure and enthalpy. The conservation equations are presented in fully compressible form. This results for the conservation of mass in

$$\frac{\partial \rho}{\partial t} + \nabla \cdot (\rho \vec{v}) = 0, \tag{2.12}$$

where ρ the mass density and $\vec{v}$ the flow velocity and t the time. The conservation of momentum is covered by the Navier-Stokes equation, given by

$$\frac{\partial \rho \vec{v}}{\partial t} + \nabla \cdot (\rho \vec{v} \vec{v}) = -\nabla p - \nabla \cdot \boldsymbol{\tau}, \tag{2.13}$$

with p the pressure and $\boldsymbol{\tau}$ the stress tensor, given by

$$\boldsymbol{\tau} = \mu \left(\nabla \vec{v} + (\nabla \vec{v})^T + \frac{2}{3}(\nabla \cdot \vec{v})\boldsymbol{I} \right), \tag{2.14}$$

with μ the viscosity. In the conservation of momentum is the gravitational body force neglected. The conservation of energy is described in terms of enthalpy by

$$\frac{\partial \rho h}{\partial t} + \nabla \cdot (\rho \vec{v} h) = -\nabla \cdot \vec{q} - \boldsymbol{\tau} : (\nabla \vec{v}) + \frac{dp}{dt}, \tag{2.15}$$

where $\vec{q}$ denotes the heat flux vector. The heat flux is modelled by a term describing the heat transport due to conduction and due to mass diffusion (Dufour effect). This results in the following heat flux vector

$$\vec{q} = -\frac{\lambda}{c_p} \nabla h + \sum_{i=1}^{N_s} \rho \vec{V}_i h_i, \tag{2.16}$$

where λ is the thermal conductivity, c_p is the specific heat at constant pressure. The conservation equation for species i is solved for $N_s - 1$ species, since the mass fraction Y_{N_2} follows from $\sum_{i=1}^{N_s} Y_i = 1$. Hence, the $N_s - 1$ number of species are described in terms of mass fraction Y_i by

$$\frac{\partial \rho Y_i}{\partial t} + \nabla \cdot (\rho \vec{v} Y_i) = -\nabla \cdot (\rho \vec{V}_i Y_i) + \dot{\omega}_i \qquad \text{for} \quad i = 1, ..., N - 1, \tag{2.17}$$

where $\dot{\omega}_i$ is the chemical source term and $\vec{V}_i$ represents the diffusion velocity. The first term on the right hand side describes the diffusion of species. This is further explained in section 2.5. The second term in the conservation equation for mass 2.12, momentum 2.13, enthalpy 2.15 and species 2.17 represents transport due to convection. To close the set Equations (2.12)-(2.17) it is assumed that all species behave as an ideal gas. Hence, the thermodynamic pressure p follows from the sum of the partial pressures. The ideal gas law is used to solve for pressure p, which is given by

$$p = \rho \Re T \sum_{i=1}^{N_s} Y_i / M_i, \tag{2.18}$$

with M_i the molar mass of species i and $\Re$ the universal gas constant. The enthalpy h and isobaric heat capacity c_p of the gas mixture are obtained by a mass fraction weighted summation of the individual enthalpies h_i and specific heats $c_{p,i}$ of species, which yields

$$h = \sum_{i=1}^{N_s} Y_i h_i, \tag{2.19}$$

$$c_p = \sum_{i=1}^{N_s} Y_i c_{p,i}. \tag{2.20}$$

In which h_i depends on the enthalpy of formation h_i^{ref} with a temperature T^{ref} and a thermal part, given by

$$h_i = h_i^{ref} + \int_{T_{ref}}^{T} c_{p,i}(T^*) dT^*. \tag{2.21}$$

The isobaric heat capacity and enthalpy of each specie is tabulated by the NASA polynomials as function of the temperature, in the form [1]

$$\frac{c_{p,i}}{\mathcal{R}} = \sum_{n=1}^{5} a_{n,i} T^{n-1}, \tag{2.22}$$

$$\frac{h_i}{\mathcal{R}T} = \sum_{n=1}^{5} \frac{a_{n,i}}{n} T^{n-1} + \frac{a_{0,i}}{T}. \tag{2.23}$$

The thermal conductivity λ is modelled by applying a semi-empirical formulation [35]

$$\lambda = \frac{1}{2} \left(\sum_{i=1}^{N_s} X_i \lambda_i + \left(\sum_{i=1}^{N_s} X_i / \lambda_i \right)^{-1} \right), \tag{2.24}$$

with X_i the molar fraction of species i. The individual thermal conductivities tabulated in a form given by the NASA database [1]

$$\ln \lambda_i = \sum_{i=1}^{4} a_{n,i} \ln T^{n-1}. \tag{2.25}$$

The dynamic viscosity μ is given by

$$\mu = (0.523 + 1.93 \cdot 10^{-5} T) \cdot \frac{\lambda}{c_p}. \tag{2.26}$$

In this section almost the full set of equation to model turbulent combustion are presented. However in conservation equation of species 2.17 a chemical source term $\dot{\omega}_i$ appears. This term is related by the creation and consumption of species and is part of the chemistry modelling, which is discussed in the next section. Furthermore, the species diffusion velocity $\vec{V}_i$ also appears in the species transport equation 2.17. This term is discussed in section 2.5 about diffusion models.

2.4 Chemistry modelling

In the previous section the governing equations are presented. The chemical source terms ω_i in the species transport equations are given by the chemical reaction mechanism. The combustion a fuel with air consists of many elementary reactions steps. In general a chemical reaction j consisting of N_s species can be written as

$$\sum_{i=1}^{N} \nu'_{ij} \mathcal{M}_i \Leftrightarrow \sum_{i=1}^{N} \nu''_{ij} \mathcal{M}_i, \tag{2.27}$$

where $\mathcal{M}_i$ represents species i in the reaction j and $\nu_{ij} = \nu''_{ij} - \nu'_{ij}$ the stoichiometric coefficients. The reaction rate of reaction (2.27) is given by

$$r_i = k_{fj} \prod_{i=1}^{N} [\mathcal{M}_i]^{\nu'_{ij}} - k_{rj} \prod_{i=1}^{N} [\mathcal{M}_i]^{\nu''_{ij}}, \tag{2.28}$$

in which k_f is the forward reaction rate coefficient in modified Arrhenius form [39]

$$k_f = A T^{\beta} \exp\left(-E_a / RT\right), \tag{2.29}$$

with A and β reactions constants and E_a the activation energy. The reversed reaction rate coefficient k_r is usually calculated using the equilibrium constant $k_{eq} = \frac{k_f}{k_r}$ [35]. The total source term $\dot{\omega}_i$ in the species transport equation (2.17) contains the contribution of all reactions involving specie i, given by

$$\dot{\omega}_i = M_i \sum_{j=1}^{N_r} \nu_{ij} r_j, \tag{2.30}$$

where N_r is the total number of reactions. The reaction constants A, β and E_a are listed in a chemical reaction mechanism. For methane combustion, the chemical mechanism GRI3.0 presented by [34] is seen as most accurate mechanism. This mechanism contains 325 elementary reactions

and 53 species, including the formation of NO. Hence, the species transport equation given by Equation 2.17 must be solved for all 53 species. As a result the computational costs are large. Alternative chemical mechanisms with less species and elementary reactions are therefore sought. One way to reduce the chemical mechanism is by using a steady-state assumption for some particular reactions and species which are involved in fast processes. A quasi steady-state approximation states that for certain species the chemical reactions balance, which means for example for species i result in

$$\dot{\omega}_i = M_i \sum_{j=1}^{N_r} \nu_{ij} r_j = 0. \qquad (2.31)$$

As a result the number of species to be solved is reduced. The DRM19 mechanism is such a reduced chemical mechanism, which consists of 19 species and 84 elementary reactions [21]. The reduced mechanism was tested on laminar adiabatic premixed methane-air flames against the detailed mechanism GRI3.0. It was found that the adiabatic flame temperature T_{ad} computed with the reduced mechanisms was practically indistinguishable from that predicted by the GRI3.0 mechanism. Furthermore, the reduced mechanism was able to predict the laminar burning velocity within an 8% error for lean mixtures [21]. However, the formation of NO is not included in the DRM19 mechanism. Therefore, the Zeldovich mechanism is added to the DRM19 mechanism to include the formation NO. The Zeldovich mechanism is given by [39]:

$$N_2 + O \rightleftharpoons NO + N, \qquad (Z.1)$$

$$N + O_2 \rightleftharpoons NO + O, \qquad (Z.2)$$

$$N + OH \rightleftharpoons NO + H. \qquad (Z.3)$$

With these reactions, the extended DRM19 mechanism consists of 87 reactions and 21 species. Due to the strong triple bonding of N_2, reaction Z.1 has a high activation energy E_a. As a result the NO production by this mechanism occurs at a slower rate than the combustion of fuel and is extremely temperature sensitive. Hence, the Zeldovich mechanism is referred to as thermal NO mechanism. Which means thermal NO can be minimized by reducing the flame temperature.

Besides the thermal mechanism, the prompt NO mechanism is also responsible for NO formation. In this thesis prompt NO is referred to as all NO formed which are not produced by the thermal mechanism. Prompt NO producing pathways are more complicated than thermal NO, because these involve way more species and reactions. Prompt NO results from the radical CH. This radical is formed as an intermediate at the flame front and reacts with the nitrogen of air, forming hydrocyanic acid (HCN), which reacts further in to NO. Fenimore discovered that NO is formed rapidly in the flame zone before there would be time to form NO by the thermal mechanism [13]. This was called prompt NO, which is included in the GRI3.0 mechanism.

In Figure 2.10 the mass fraction NO in a methane-air flame at $\phi = 0.7$ is given. It can be seen that DRM19 mechanism with thermal NO under-predicts the NO formation. This large deviations can be explained by Figure 2.11, which shows the source term $\dot{\omega}_{NO}$ for the two mechanisms. The dotted line represents the NO formation due to the Zeldovich reactions in the GRI3.0 mechanism. It can be seen that the same Zeldovich route results in a larger source term in the reaction layer with the GRI3.0 mechanism. Furthermore, it can be seen that the thermal NO formation is not exclusively responsible for the formation of NO. Only 45 % of the total NO formed in this flame is due to the Zeldovich mechanism. Therefore, other NO mechanisms such as prompt NO contribute to the rest of the NO production. Prompt NO is formed near the reaction layer. Hence, the sharp peak in NO source term and mass fraction at the flame front. Further downstream in the flame, only thermal NO is responsible for NO production and the source terms are the same for both mechanism.
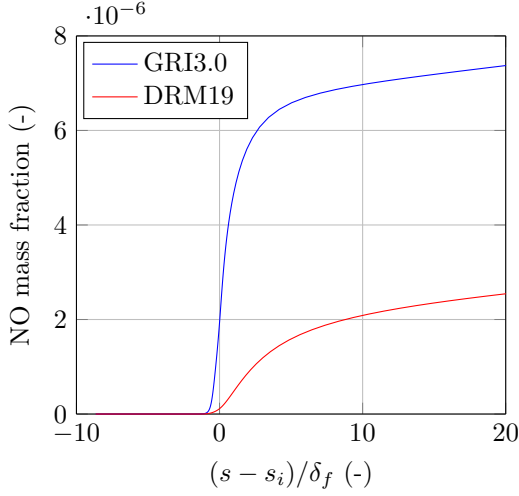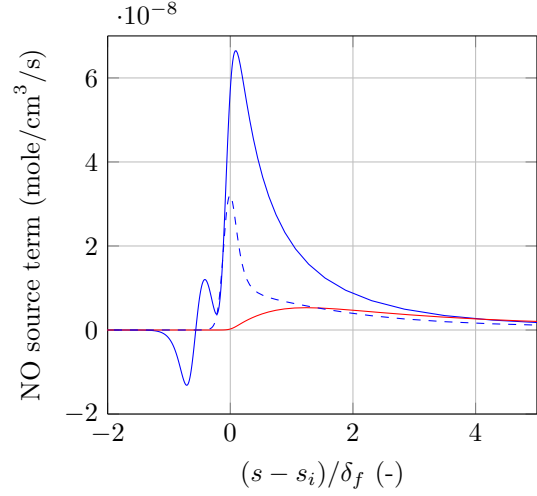
Figure 2.10: Mass fraction NO in the flame

Figure 2.11: Source term $\dot{\omega}_{NO}$ in the flame

2.5   Transport models

In this section three transport models are presented for the last unknown variable, the species diffusion velocity $\vec{V}_i$, which needs to be closed in order to solve the conservation equations. These transport models are presented in order of decreasing complexity and discussed in terms of performance on modeling the mass burning rate and NO mass fraction in 1D methane-hydrogen flames.

Diffusion models

The most advanced model is the multicomponent model. The species mass diffusion velocity V_i in the multicomponent model is given by

$$\vec{V_i} = \frac{1}{X_i \overline{M}} \sum_{j=i}^{N_s} M_j D_{ij} \vec{d_j} - \frac{D_i^T}{\rho Y_i T} \nabla T, \tag{2.32}$$

with

$$\vec{d_j} = \nabla X_j + (X_j - Y_j) \frac{1}{p} \nabla p. \tag{2.33}$$

Equation 2.32 shows that the mass diffusion is caused by a concentration gradient, pressure gradient or a temperature gradient. Diffusion due to a temperature gradient is called the Soret diffusion. In this equation X_i is the mole fraction of species and related to mass fraction by $X_i = Y_i \overline{M}/M_i$, D_{ij} and D_i^T are the generalized diffusion coefficients follow from solving the Stefan-Maxwell equations, given by

$$\nabla X_i = \sum_{j=1}^{N_s} \frac{X_i X_j}{\mathcal{D}_{ij}} (\vec{V_j} - \vec{V_i}) + \sum_{j=1}^{N_s} \left[\left(\frac{X_i X_j}{\rho \mathcal{D}_{ij}} \right) \left(\frac{D_{ij}^T}{Y_j} - \frac{D_i^T}{Y_i} \right) \nabla (\ln T) \right], \tag{2.34}$$

where $\mathcal{D}_{ij}$ are the binary diffusion coefficients. Since the diffusion of a specie depends on the concentration gradient of all species. solving the Stefan-Maxwell equation can be computational expensive. Therefore, the mixture-averaged diffusion model can be used as approximation. In the mixture-averaged diffusion model it is assumed that the diffusion velocity for each species is calculated by approximating all other species' velocities as the same. This means that instead of calculating the diffusion therm D_{ij} for each gas couple in the multicomponent model, only one

diffusion therm D_{im} is calculated for each species. The mixture-averaged model calculates the species diffusion velocity by a Fick-like expression

$$\vec{V_i} = -\frac{D_{im}}{Y_i}\nabla Y_i, \tag{2.35}$$

with D_{im} is the mixture-averaged diffusion coefficient, which describes the diffusion of species i in the mixture, expressed as

$$D_{im} = \frac{1 - Y_i}{\sum_{j \neq i}^{N} X_j / \mathcal{D}_{ij}}. \tag{2.36}$$

Which can be derived from the Stefan-Maxwell equation by assuming that all diffusion velocities between species obtain one value, $V_j = V$ for $j \neq i$ and neglecting Soret diffusion. The mixture-averaged diffusion model is a good approximation in premixed combustion with air, since Nitrogen is dominating [35]. The diffusion velocity can also described by using the constant Lewis number diffusion model. The Lewis number is defined in Equation 2.11 as the ratio of thermal to mass diffusion flux, which results in

$$Le_i = \frac{\lambda}{\rho D_{im} c_p}. \tag{2.37}$$

Hence, the species diffusion flux can be rewritten as

$$\rho \vec{V_i} Y_i = -\frac{\lambda}{Le_i c_p} \nabla Y_i, \tag{2.38}$$

and the heat flux results in

$$\vec{q} = -\frac{\lambda}{c_p} \nabla h - \frac{\lambda}{c_p} \sum_{i=1}^{N_s} \left(\frac{1}{Le_i} - 1 \right) \nabla Y_i. \tag{2.39}$$

Which shows that for non-unity Lewis number of species i, caused by different diffusion coefficients for mass and heat, species i and heat are redistributed and locally there is more or less mass and/or heat.

To check whether the results are influenced by the choice of diffusion model, simulations are performed by CHEM1D [35], which solves the governing equations for one-dimensional flames (flamelets) for the case of a freely propagating lean premixed methane/air flame enriched with 40% hydrogen at $\phi = 0.7$ by using the GRI3.0 mechanism. In Figure 2.12 the mass burning rate for the different diffusion models against the Karlovitz number is given. The Karlovitz number is a dimensionless number that corresponds to the ratio of chemical time scale and characteristic flow time scale, defined as

$$Ka = K\frac{\delta_f^0}{s_L^0}. \tag{2.40}$$

It can be seen that the mass burning rate is reduced by positive stretch with the constant Lewis number model, while mass burning rate is enhanced by positive stretch with the multicomponent and mixture-averaged model. Which means that in the later two diffusion models the effect of preferential diffusion to the positive stretched regions in the flame is higher than the mass loss due to the direct stretch effect. The constant Lewis model predicts a 1.9% smaller initial mass burning rate m_b^0 compared to the multicomponent diffusion model. It can be seen that at larger strain rates this error increases to 4%. A possible reason can be the Soret diffusion of the lighter species due to a temperature gradient, which is taken into account in the multicomponent diffusion mode.

Figure 2.13 shows the mass fraction NO at 2 cm against the Karlovitz number for three different diffusion models. It can be seen that the constant Lewis number diffusion model under-predicts the NO formation in the flame with respect to the multicomponent model by 11%. However, the constant Lewis number model captures the positive correlation of NO formation with stretch.
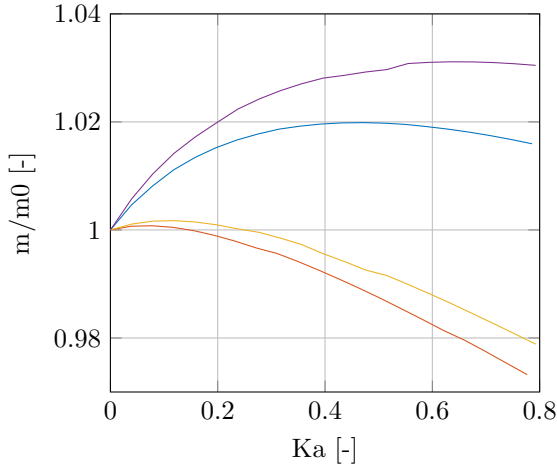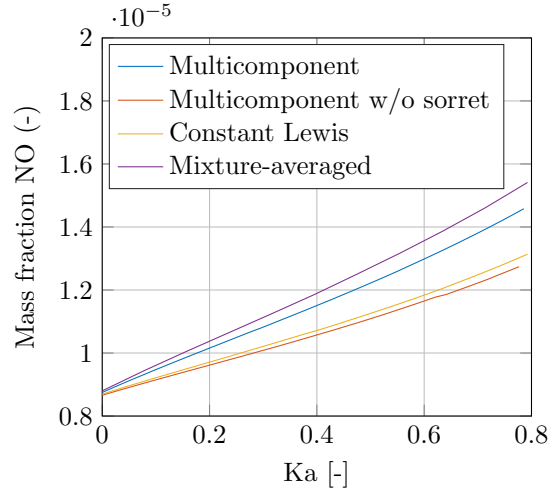
Figure 2.12: Mass burning rate with 40% H_2

Figure 2.13: peak mass fraction NO

Since hydrogen is a highly diffusive species with a Lewis number of $Le_{H_2} = 0.3$, the Soret effect has a larger influence in the hydrogen enriched flame compared to the methane-air flame. Zhen Zhou et. al. found that the effect of Soret diffusion on the mass burning rate of a lean hydrogen-air flame with increasing stretch rate results from coupling effects between preferential diffusion and Soret diffusion [41]. They concluded that the Soret diffusion leads to additional changes in the local redistribution of hydrogen due to the preferential diffusion. The lighter hydrogen specie tend to go to the higher temperature parts of the flame due to Soret diffusion.
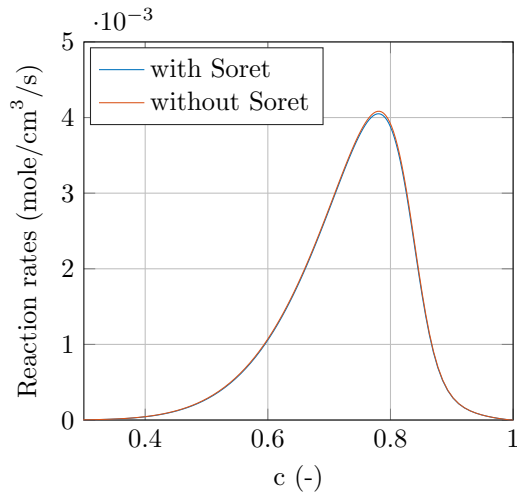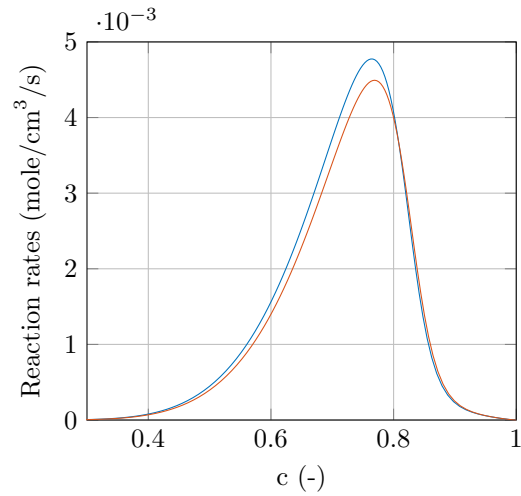
Soret Diffusion

To study the influence of the Soret diffusion on the hydrogen enriched flame, the multicomponent diffusion model is used without the last term in Equation 2.32. In Figure 2.13 it can be seen that less NO is formed without Soret diffusion. In Figure 2.12 the mass burning rate with and without Soret diffusion is given. It is observed that the mass burning rate is enhanced at low stretch rates due to Soret diffusion. The initial mass burning rate m^0 is 1.2% larger without Soret diffusion. Increasing the stretch rate results in enhanced H_2 and H concentrations and an increasing $\nabla T/T$ due to temperature rise by preferential diffusion. Therefore, more H_2 is diffused to the high temperature regions by Soret diffusion which increases the mass burning rate and thus local temperature and NO formation.

In Figures 2.14 and 2.15 the reaction rate of chain branching reaction $H + O_2 = OH + O$ is given as function of the normalized temperature for the respectively Ka = 0 and Ka = 0.7 . The normalized temperature is defined as

$$c = \frac{T - T_u}{T_b - T_u},\tag{2.41}$$

where T is the local temperature, T_b is the burned temperature and T_u is the unburned temperature. According to Zhen Zou et al., this chain branching reaction is a major relevant reaction affected by Soret diffusion of H [41]. It can be seen in Figure 2.14 that the reaction rate of the unstretched flame with Soret diffusion is almost similar than without Soret diffusion. However, in Figure 2.15 it is observed that the reaction rate of the stretched flame with Soret diffusion is higher than without Soret diffusion. In this case, the reaction rate is enhanced due to Soret diffusion.

Figure 2.14: Reaction rate with Ka = 0

Figure 2.15: Reaction rate with Ka = 0.7

Concluding, different diffusion model show different results for mass burning rate and NO formation. However, the constant Lewis number diffusion model under-predicts the NO formation with 11% and the mass burning rate with 5% compared to the multicomponent model at Ka = 0.8. Which is an acceptable error as the computational costs of multicomponent model and mixture-averaged model are much higher than the constant Lewis number approach. The main reason for these differences are due to Soret diffusion. Therefore, in the remainder of this thesis the constant Lewis number diffusion model is used. In the next section this model is used to study the influence of hydrogen mixed to methane-air flames .

2.6 Laminar 1D methane-hydrogen-air flames

Lean premixed combustion of methane has gained interest due to its advantages of high thermal efficiency and low NO emissions. However, leaner combustion results in lower flame temperature, which can reduce the flame stability or lead to flame quenching. To avoid these problems small amounts of hydrogen can be added to the fuel. The addition of hydrogen increases the laminar burning velocity and lowers the lean flammability limit of the flame [9]. Hydrogen has a Lewis number of 0.3, which is significantly lower than unity. As a result, the fuel has an effective Lewis number below unity and the flame encounters a preferential diffusion effect of hydrogen into positively curved and strained regions [26, 38]. In these regions the mixture is locally richer, which increases the burning velocity and temperature of the flame. Therefore, addition of H_2 might be expected to have a negative impact on NO levels from the Zeldovich thermal mechanism due to higher flame temperatures [39]. However this may be offset by the ability to burn an overall leaner mixture.

This is supported by performing a one dimensional simulation by using Chem1D [35], which solves the set of governing equations for laminar premixed freely propagating flames. Simulations are performed for different mixtures of CH_4/H_2 premixed with air at an equivalence ratio of $\phi = 0.7$. It is assumed that that air consist of 21% oxygen and 79% on mole basis. The DRM19 reaction mechanism is used [21], with a constant Lewis number diffusion model. A freely propagating premixed flame with an applied strain rate is used to study the interaction between methane-hydrogen-air mixtures and flame stretch.

In Figure 2.16 the laminar burning velocity for different methane-air flames enriched with hydrogen are presented. It can be seen that the laminar burning velocity is increased with the
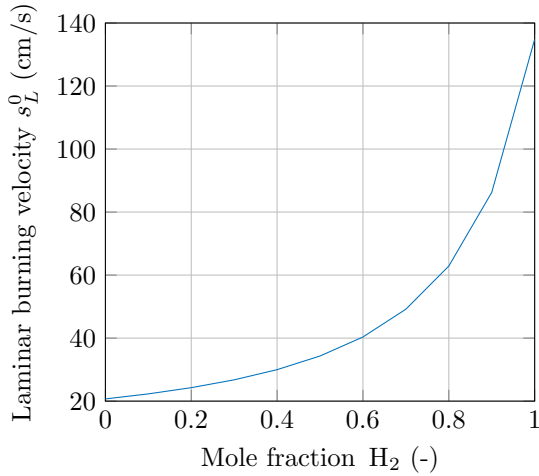
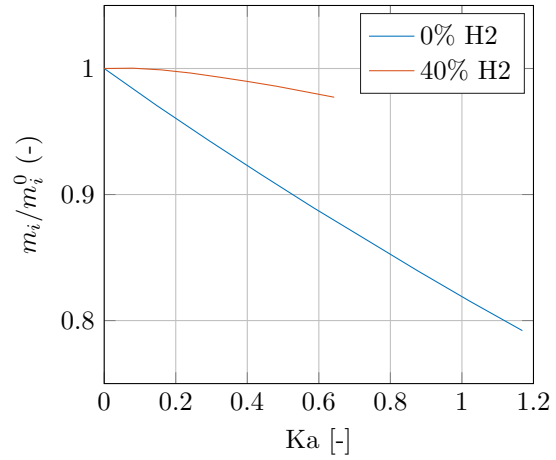Figure 2.16: The laminar burning velocity
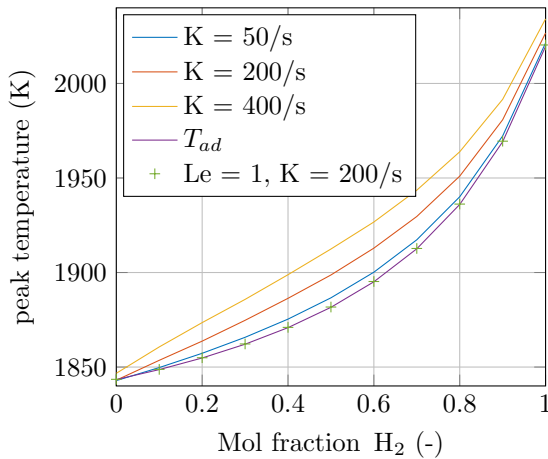

Figure 2.17: Normalized mass burning rate
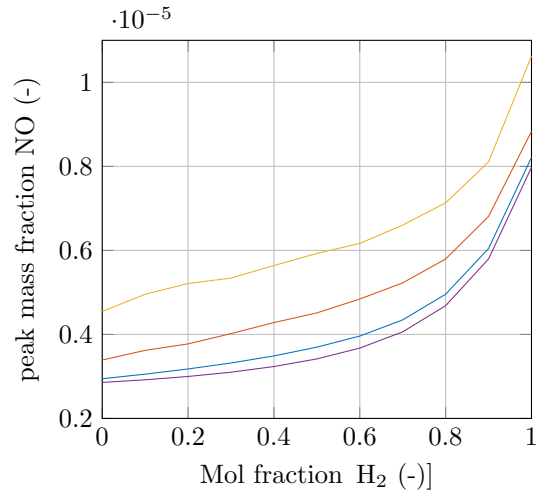

Figure 2.18: Maximum flame temperature

Figure 2.19: Peak NO mass fraction

addition of hydrogen. A gradual increase in laminar burning velocity is seen as the hydrogen mole faction is increased from 0 to 0.5. For hydrogen-dominating mixtures above a mole fraction of 0.5, the laminar burning velocity increases rapidly. In Figure 2.17 the normalized mass burning rate $\rho s_L / \rho s_L^0$ at the reaction layer for a methane-air flame and a methane-hydrogen air flame mixed 40% H_2 on mole basis is given as a function of the Karlovitz number. Te mass burning rate is decreased with strain in the pure methane case due to the direct effect of stretch, which results in loss of mass in the flamelet. However, the mass burning rate is decreasing faster for pure methane compared to the methane flame enriched with 40% H_2. This phenomenon is caused by preferential diffusion of H_2, which arises from an imbalance in diffusion rates in a stretched flame as explained previously. The addition of hydrogen gives the fuel a Lewis number below unity and thus locally higher hydrogen concentrations in the positive stretched flames. Therefore, the burning rates are enhanced by preferential diffusion of hydrogen into the reaction zone which counteracts the direct loss of mass due to strain.

The increase in mass burning rate due to preferential diffusion results in higher flame temperatures, as can be seen in Figure 2.18. The maximum flame temperature is given for different

methane-hydrogen mixtures. It is noted that the maximum flame temperature for strain rates K of 50, 200 and 400 s^{-1} is above the adiabatic flame temperature. Furthermore, it shows that the adiabatic temperature is increased by enriching the methane flame with hydrogen. The reason for this is the higher adiabatic flame temperature of hydrogen relative to methane. It can be seen that for a stretched flame with unity Lewis number, the peak flame temperature is similar to the adiabatic flame temperature since no preferential diffusion effect occurs. As a result of the increasing temperatures, the NO formation is enhanced due to the thermal NO mechanism. This is displayed in Figure 2.19, where it is shown that an increasing the peak mole fraction of NO are given for different mixtures of CH_4/H_2 with air.

Whether these effects occur in turbulent flow is subject of study in this theses. The influence of hydrogen enrichment in turbulent premixed methane-air flames is investigated by performing direct numerical simulations. The case setup for these stimulations is discussed in the next chapter.

Chapter 3

Case setup

In this chapter the case setup in the DNS code is discussed. First, the code is introduced followed by a discussion about the geometry of the computational domain and the initialization of the two flames. After that, the code is validated by comparing the laminar burning velocity and flame thickness with CHEM1D [35]. Finally, the turbulent case setup is presented. All simulations reported in the remaining part of this thesis concern two different lean premixed fuel/air mixtures at atmospheric pressure $p_u = 1$ bar and with an equivalence ratio $\phi = 0.7$. The first one is a lean premixed methane-air flame. The second flame is a lean premixed methane-hydrogen-air flame, where hydrogen is blended with methane at a ratio of 40% hydrogen and 60% methane on molar basis.

3.1   The DNS code

The DNS code is developed by [2, 37, 16]. The code solves the fully compressible governing equations for mass 2.12, momentum 2.13, species 2.17 and energy 2.15 in terms of respectively density ρ, velocity $\vec{v}$, species mass fraction Y_i and temperature T

$$\frac{\partial \rho}{\partial t} + \frac{\partial}{\partial x_i}(\rho v_i) = 0, \tag{3.1}$$

$$\rho \frac{\partial v_j}{\partial t} + \rho v_i \frac{\partial v_j}{\partial x_i} = -\frac{\partial p}{\partial x_j} + \frac{\partial \tau_{ij}}{\partial x_i}, \tag{3.2}$$

$$\rho \frac{\partial Y_i}{\partial t} + \rho v_i \frac{\partial Y_i}{\partial x_i} = \frac{\partial}{\partial x_i}(\frac{\lambda}{Le_i c_p}\frac{\partial Y_i}{\partial x_i}) + \dot{\omega}_i \qquad i = 1, ..., N_s - 1, \tag{3.3}$$

$$\rho c_v \frac{\partial T}{\partial t} + \rho c_v v_i \frac{\partial T}{\partial x_i} = \frac{\partial}{\partial x_i}(\lambda \frac{\partial T}{\partial x_i}) - p\frac{\partial v_i}{\partial x_i} + \tau_{ij}\frac{\partial v_i}{\partial x_j} + \frac{\partial}{\partial x_i}\left(\sum_{i=1}^{N_s-1} h'_i \frac{\lambda}{Le_i c_p}\frac{\partial Y_\alpha}{\partial x_i}\right)$$
$$- \sum_{i=1}^{N_s-1}(h'_i - R'_i T)\left[\dot{\omega}_i + \frac{\partial}{\partial x_i}\left(\frac{\lambda}{Le_i c_p}\frac{\partial Y_i}{\partial x_i}\right)\right]. \tag{3.4}$$

The pressure p is calculated with the ideal gas law in Equation 2.18, the viscous stress tensor τ by Equation 2.14 and thermal conductivity λ by Equation 2.24. The species transport equation 3.3 is solved for the first $N_s - 1$ species, since the mass fraction Y_{N_2} follows from $\sum_{i=1}^{N} Y_i = 1$. Furthermore, by introducing the enthalpy $h'_i = h_i - h_{N_2}$ and gas constant $R'_i = R_i - R_{N_2}$ and summing over $N_s - 1$ species, the diffusion correction in Equation 3.4 is taken into account. The diffusion fluxes of nitrogen balance the sum of the diffusion fluxes of the other species. To calculate the chemical source terms of species, two different reaction mechanism are used. The detailed chemical mechanism GRI3.0 [34] and the reduced mechanism DRM19 based on GRI1.2 [21]. The diffusion is modelled by using the constant Lewis number diffusion model, since it has

---

relative low in computational costs. The Lewis numbers are obtained by fitting the results to 1D-solutions of CHEM1D with the multicomponent diffusion model. In section 2.5 it was seen that preferential diffusion effects were include by using the constant Lewis number model. For the sake of efficiency, Soret and Dufour effects are neglected. Although it is supposed that these effects would enhance the conclusions presented in this thesis, since Soret diffusion promotes diffusion of light species toward hot regions in the flame. The governing equations are discretized by using the implicit sixth-order compact finite difference scheme [24] for the diffusion terms and the fifth-order method [10] for the convective terms. The time derivatives are calculated with an explicit compact-storage Runge-Kutta schema of third order.

3.2 Geometry and flame initialization

In order to study the interaction of turbulence with flames, a two and three dimensional computational domain is used as shown in Figure 3.1. In two dimensions this geometry has a rectangular shape and can be extended in the z-direction for 3D simulations. It consists of a cold premixed fuel/air core with width w surrounded by a hot stream of burnt gases flowing in x-direction with a velocity difference of ΔU. This profile is kept constant in z-direction for 3D simulations. This velocity difference create Kelvin-Helmholtz instabilities in the shear layer and therefore triggers mixing between the unburnt and burnt layers. A initial homogeneous and isotropic turbulence is applied to the cold premixed fuel/air core to develop initial vortices. An periodic boundary condition is used in x-direction (and z-direction in case of 3D simulations). Hence, gases flowing out of the domain on one side are flown back into the domain on the other side. A non-reflecting boundary condition is applied in y-direction. Initially the premixed mixture enters the domain with a temperature of $T_u = 300$ K and the co-flow of burnt gas flows with the adiabatic flame temperature T_{ad}.
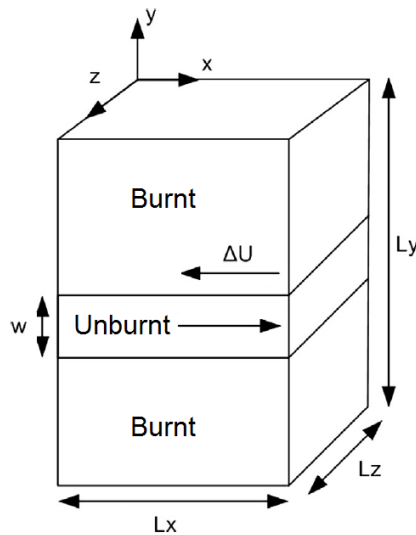

Figure 3.1: Computational domain

The species Y_i, temperature T and density ρ in the geometry are initialized by the profiles of a steady laminar flame. Two different premixed mixtures are used. The reference case consists of premixed methane-air flame. The profiles of species and temperature of this flame are obtained by CHEM1D, as shown in Figure 3.2. Furthermore, it is assumed that air consists of 79% N_2 and 21% O_2 on a molar basis. It can be seen that when methane CH_4 and oxygen O_2 start to reaction, the temperature starts to increase. At the end of the combustion process, the final products are left and the temperature obtains the adiabatic flame temperature T_{ad}. Oxygen is

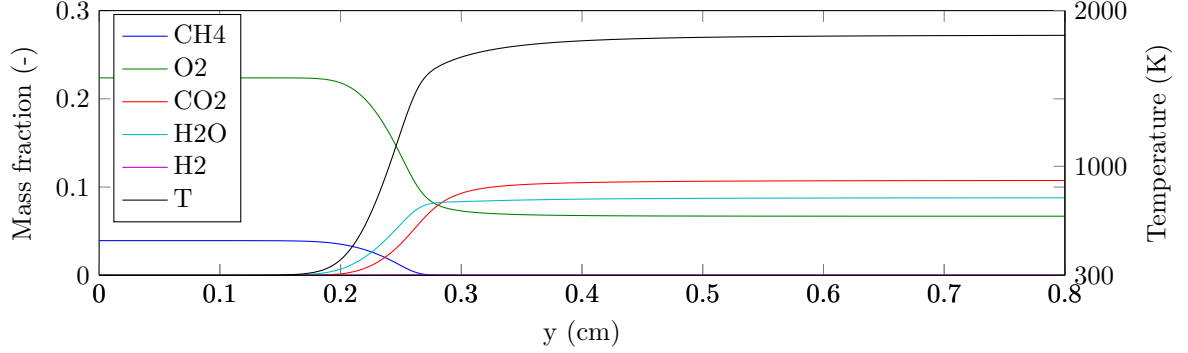one of the final products, since the equivalence ratio $\phi = 0.7$ is smaller than one.

Figure 3.2: The species and temperature profiles of the methane-air flame as function of distance in the flame.

Parameter	Symbol	Value
Unburnt layer width	w	4 mm
Domain size	L_x x L_y x L_z	8 mm x 16 mm x 4 mm
Velocity difference	ΔU	60 m/s

Table 3.1: Geometry parameters

The other mixture used in this study is a premixed methane-hydrogen-air flame, where methane is blended with 40% hydrogen on a molar basis. A addition of 40 % hydrogen is chosen such that methane is still dominating in the flame, but the effects of hydrogen addition are clearly visible. The temperature and species profile of this freely propagating flame is given in Figure 3.3. Despite hydrogen is added to the premixed methane/air with a ratio of 40% H_2 and 60% CH_4 on molar basis, this can be is barely seen in Figure 3.3. Hydrogen is a very light specie, therefore it's mass fraction Y_{H_2} is low. It can be seen that the addition of hydrogen leads to an increase of mass fraction H_2O and a decrease of CO_2 in the burnt products compared to the methane-air flame. The profiles of species, temperature and density for the two mixtures with $X_{H_2} = 0$ and 0.4 are projected in the (transverse) y-direction of the geometry and mirrored around the origin. This results in a domain length of $L_y = 2 \cdot 0.8$ cm $= 1.6$ cm and an unburnt fuel/air mixture core width
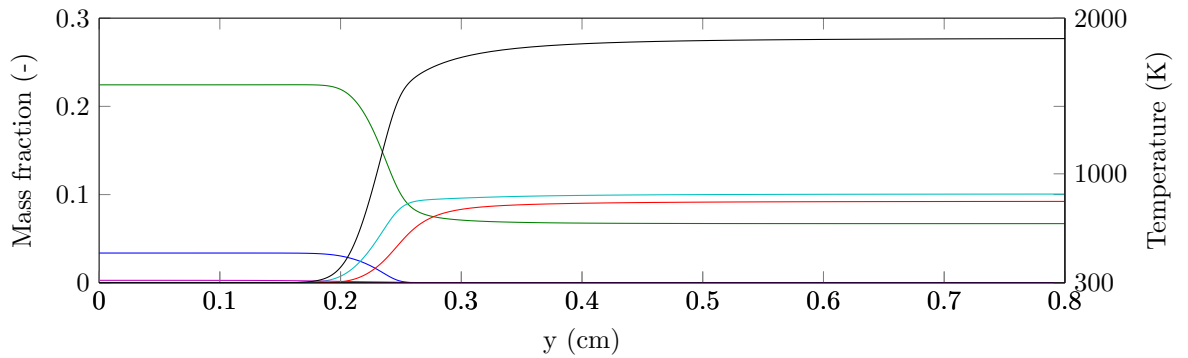
Figure 3.3: The species and temperature profiles of the methane-hydrogen-air flame with $X_{H_2} = 0.4$ as function of distance in the flame.

w of 4 mm. In Table 3.1 the geometry parameters are given as displayed in Figure 3.1 are given. The length in stream-wise direction is chosen to be $L_x = 0.8$ cm and for 3D simulations a length L_z of 0.4 cm in span-wise direction is chosen. In the next section the DNS code is validated by using a 2D geometry.

3.3   Validation of the DNS code

The DNS code is validated by comparing the laminar burning velocity of the methane-air and methane-hydrogen-air flame in the DNS code with the one-dimensional result given by CHEM1D[35]. The DRM19 mechanism is chosen as chemical mechanism. A domain length of $L_y = 1.6$ cm in y-direction and $L_x = 0.2$ cm in x-direction is used, which consists out of 801 by 201 grid points. This means an equally spaced resolution is found of $\delta = 2 \cdot 10^{-5}$ m $= 0.02$ mm. Simulations are performed by for 10^5 time steps of with a time step of $\Delta T = 10^{-8}$s. This temporal resolution is chosen such that it is small enough to capture the acoustic waves traveling with the speed of sound γ. This can be verified by checking the CFL condition

$$C = \gamma \frac{\Delta T}{\delta_x} < 1, \tag{3.5}$$

which results in Courant number $C = 343 \cdot \frac{10^{-8}}{0.2 \cdot 10^{-2}} = 0.172$ and must be smaller than one for explicit scheme's [5]. The code is initialized by the species and temperature profile of free adiabatic flame solutions, as given in Figures 3.2 and 3.3 for respectively the methane-air and methane-hydrogen-air flame. A constant velocity in stream-wise direction is applied to keep the flame laminar, thus $\Delta U = 0$. The laminar burning velocity of the DNS solution is calculated by taking the derivative of the flame displacement of the flame front with respect to time. The flame front is identified as the iso-surface of methane where the iso-level corresponds to the location of maximum heat release is a freely propagating laminar flame.
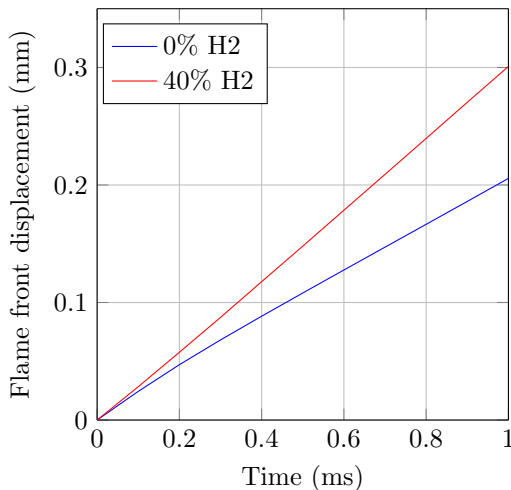

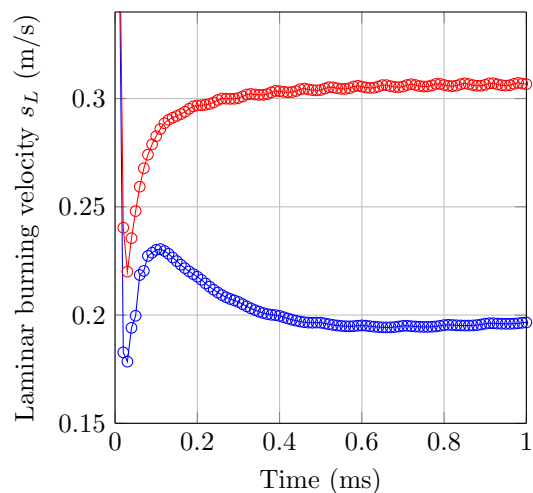Figure 3.4:   Flame front displacement as function of time.

Figure 3.5: Burning velocity s_L as function of time.

In Figure 3.4 the flame displacement of the flame front is given as function of time for the laminar flame with X_{H_2} 0.0 and 0.4. It can already be seen that the hydrogen enriched flames burns faster, since the slope is higher. In absence of a flow velocity field normal to the flame front, the derivative of the flame displacement with respect to time corresponds to the flame displacement
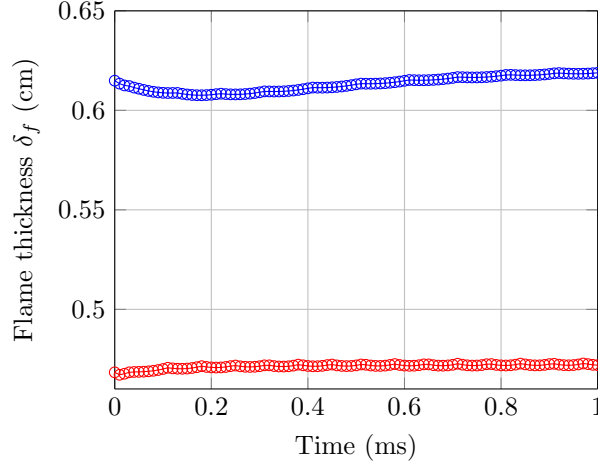
Figure 3.6: Flame thickness δ_f as function of time.

speed. Which is the laminar burning velocity in this case, since $\vec{v}_f = s_L \vec{n}$ in absence of a flow field. In Figure 3.5 the laminar burning velocity is given as function of time. It can be observed that the initial conditions have an effect on the burning velocity, but after some time a constant value is reached. This results in a laminar burning velocity of $s_L = 19.7$ cm/s and 30.6 cm/s, which is an error of 2% compared to the laminar burning velocity found by CHEM1D. In Figure 3.6 the flame thickness is given as function of time. The definition used for flame thickness is given in Equation 2.4. It can be seen that the flame thickness is $\delta_f = 0.62$ cm and 0.47 cm for the respectively methane-air and methane-hydrogen-air flame. This flame thickness deviates maximal 1.6% with the flame thickness found by CHEM1D.

3.4 Turbulent setup

The velocity of the unburt mixture is 30 m/s and the burnt mixture has a velocity of -30 m/s in x-direction. Which means a relative velocity of $\Delta U = 60$ m/s is applied. In order to make a smooth transition of the velocity from 30 m/s to -30 m/s a Sigmoid function is used, given by

$$U(y) = \frac{U_b - U_u}{1 + \exp \frac{y_0 - y}{\alpha}} + U_u. \tag{3.6}$$

This velocity difference creates shear layers between the unburnt and burnt mixture. To trigger mixing between the shear layers, an initial homogeneous and isotropic turbulence is applied to the cold premixed fuel/air core. These perturbations are added to the mean velocity of in the flow and help to develop initial vortices between the layers. The intensity I of the turbulent perturbations is defined as

$$I = \frac{u'_{rms}}{\Delta U}, \tag{3.7}$$

where u'_{rms} is the root mean square of the velocity fluctuations u'. These fluctuations are calculated by taking the velocity and subtract the mean velocity, $u' = u - \bar{u}$. Two different nominal turbulent intensities of $I = 5\%$ and 10% are used in the simulations. In Figure 3.7 the velocity profile u in stream-wise direction is presented for a cross-section in the transverse direction, the y-direction. It can be seen that the unburnt premixed fuel/air is turbulent with a mean velocity of $u = 30$ m/s. Furthermore, a smooth transition is made to the burnt mixture which flow with a velocity of $u = $ -30 m/s. The difference in turbulent intensity in displayed is Figure 3.8, which shows the velocity fluctuations v' for a cross-section in y-direction for the two different intensities. It is shown that the turbulent fluctuations are similar, but differ a factor 2 in magnitude.
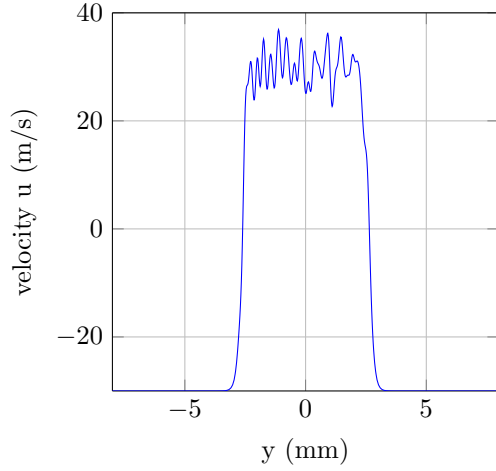
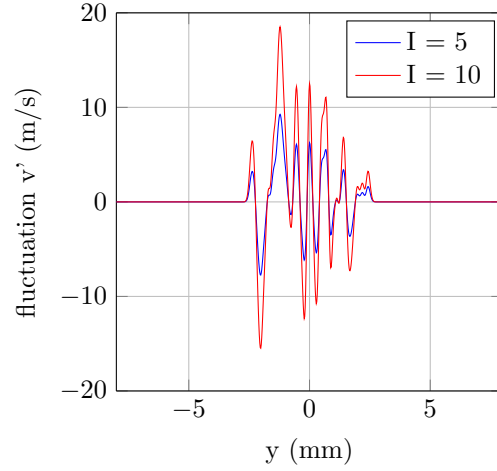Figure 3.7: Cross-section in y-direction of the velocity u.

Figure 3.8: Cross-section in y-direction of fluctuations v'.

The size of the largest eddies in the flow is given by L_T, while the size of smallest eddies are by η. The largest eddies account for most of the transport and momentum. The size of these eddies L_T is often referred to as the integral length scale. The integral length scale is calculated by using a two-point velocity correlation, and is defined as

$$L_T = \int_0^\infty f(r)dr, \tag{3.8}$$

with r the distance between two points and $f(r)$ the normalized two-point velocity correlation, given by

$$f(r) = \frac{< u'(x)u'(x+r) >}{u'_{rms}{}^2}. \tag{3.9}$$

In Figure 3.9 the normalized two-point velocity correlation at $y = 0$ is shown in stream-wise direction for a methane-air flame at t = 1.0 ms. Equation 3.8 requires an integration till infinity. However, the x-domain is finite. Therefore, to calculate the integral length scale the integration is performed until $f(r)$ reaches the first zero. The kinetic energy is transferred in a process from large scale eddies with size L_T to a smaller scale eddies until it is dissipated by viscosity at the smallest scale η. For the smallest flow scales the frictional forces are important as kinetic energy is dissipated into thermal energy. The smallest scales where energy dissipation ϵ occurs are called the Kolmogorov scales, where it's length scale η is given by

$$\eta = \left(\frac{\nu^3}{\epsilon}\right)^{1/4}, \tag{3.10}$$

with ν is the kinematic viscosity [27]. This can be related to the largest flow scales The kinetic energy of the flow is proportional to $u'_{rms}{}^2$ and the large eddy turn over time t_L can be estimated as L_T/u'_{rms}. From this the dissipation rate ϵ can be estimated by

$$\epsilon \sim \frac{u'_{rms}{}^3}{L_T}. \tag{3.11}$$

Together with Equation 3.10, the estimate for the Kolmogorov length scale becomes

$$\eta = \left(\frac{\nu^3 L_T}{u'_{rms}{}^3}\right)^{1/4}. \tag{3.12}$$

As result the ratio between largest and smallest length scales in the flow can be estimated by

$$\frac{L_T}{\eta} \sim (\frac{u'_{rms}L_T}{\nu})^{3/4} = Re_T^{3/4}. \tag{3.13}$$

The turbulent scales are determined at 1.0 ms for the 2D simulations with two different turbulent intensities of I = 5 and 10. The results for the flames calculated with the GRI3.0 mechanism are given in Table 3.2. It can be seen that the Kolmogorov length scale η is in the same order of magnitude as the grid spacing δ, which justifies the choice of spacial resolution in terms of turbulence. Furthermore, Figure 3.10 shows that the turbulent fluctuations decay over time due viscous dissipation.

Table 3.2: turbulent properties at t = 1.0 ms

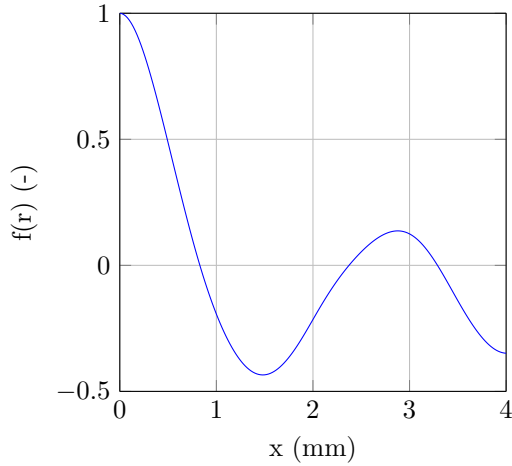| Case	I (-)	X_{H_2} (-)	u_{rms} (m/s)	L_T (mm)	t_L (ms)	η (mm)	Re_T (-)
H0-2D	5	0.0	1.85	0.47	0.25	0.0235	54
H40-2D	5	0.4	1.69	0.53	0.31	0.0256	56
H0-2D-High	10	0.0	4.32	0.87	0.20	0.0145	235
H40-2D-High	10	0.4	4.02	0.61	0.15	0.0140	153

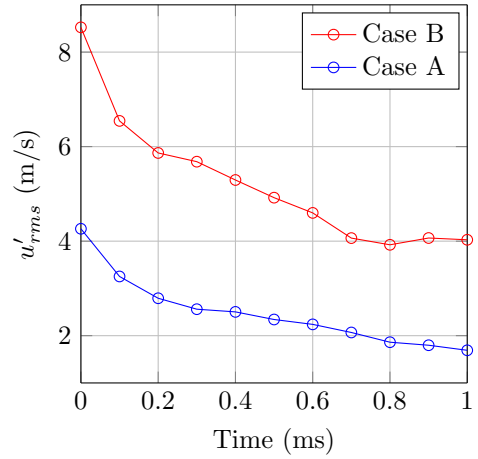Figure 3.9: Normalized two-point velocity correlation

Figure 3.10: Turbulent fluctuations decay over time

With the turbulent properties known, the flames can be categorized in a turbulent combustion regimes as proposed by Peters [28], see Figure 2.4. In Table 3.3 the flame properties of the methane-air and methane-hydrogen air flames are given. For all four cases the combustion takes place in the thin reaction zone regime. Hence, the smallest eddies η can not penetrate the reaction layer and this remains undisturbed. However, it can be seen that the flame thickness δ_f is larger than size of the smallest eddies η. Which means the eddies can penetrate and disturb the preheating zone within the flame.

Table 3.3: Flame properties by using the GRI3.0 mechanism

Case	I (-)	X_{H_2}	s_L (cm/s)	δ_f (mm)	τ_f (ms)	T_{ad} (K)	u_{rms}/s_L (-)	L_f/δ_f (-)
H0	5	0	19.13	0.666	3.45	1843	9.7	0.72
H40	5	0.4	27.0	0.530	1.96	1868	6.3	1.00
H0-High	10	0	19.13	0.666	3.45	1843	22.6	1.32
H40-High	10	0.4	27.0	0.530	1.96	1868	14.9	1.15

Chapter 4

Flame turbulence interaction

In this Chapter the flame-turbulence interaction is discussed by analysing the results of the DNS simulations. First, a surface based post-processing is performed, to get a better understanding of the results. After which the results are presented for the three-dimensional simulations. Then, the two-dimensional results are compared with the 3D simulations and the influence of turbulent intensity is investigated. Finally, the impact of turbulent methane-hydrogen-air flames on NO emissions is discussed.

4.1 Surface based post-processing

To analyse the results of the DNS simulations, surface-based post-processing of the data is performed. The flame front is defined as the iso-surface of mass fraction methane, which corresponds to the maximum source term location s_i in a laminar flame. The flame surface is extracted by interpolation over the cells. The flame surface area A is computed by taking the sum of surfaces of each rectangular cell on this iso-surface. A rectangular cell can be seen as two triangle's. The area of a triangle spanned by the vectors $\vec{x}$ and $\vec{y}$ equals $\frac{1}{2}|\vec{x} \times \vec{y}|$. Hence, the area dA of the triangular iso-surface with vertices's $(\vec{P}_0, \vec{P}_1, \vec{P}_2)$ is calculated by

$$dA_i = \frac{1}{2}|(\vec{P}_1 - \vec{P}_0) \times (\vec{P}_2 - \vec{P}_0)|. \tag{4.1}$$

The flame front, represented by flame surface, can be stretched. In this section, flame stretch definition 2.6 of the fractional rate of change of area of an infinitesimal surface element of the flame surface A is used. By definition, flame stretch contributions are due to curvature $s_d(\nabla \cdot \vec{n})$ of a moving flame front and tangential flame strain, determined by

$$a_t = \nabla \cdot \vec{v}_{||} = (\delta_{ij} - \vec{n}_i \vec{n}_j)\frac{\partial v_i}{\partial x_j}, \tag{4.2}$$

where δ_{ij} is the Kronecker delta function, which is equal to 1 if i = j and 0 otherwise. The unit normal vector of the flame front in direction of the reactants is defined as

$$\vec{n} = \frac{\nabla Y_{CH_4}}{|\nabla Y_{CH_4}|}. \tag{4.3}$$

As a result, curvature is positive in elements convex towards the unburnt mixture. Due to flame stretch, preferential diffusion effects occur. The element mass fraction Z_j is a useful parameter to describe these effect, since it is conserved in chemical reactions. It is defined as

$$Z_j = \sum_{i=1}^{N_s} w_{ji}Y_i \ \ \text{for j} = 1,..,N_j, \tag{4.4}$$

where Y_i is the mass fraction of species i and w_{ji} the mass of element j per mass of species i. In the next section 3D results are analysed by this surface based post-processing method.

4.2   3D results

In this section three different results are discussed. First some snapshots of important specie are given for the 3D case. In addition to show the effect of hydrogen addition to the methane-air mixture, two different fuels are compared. The methane-air and methane-hydrogen-air flames are referred to as case H0-3D and H40-3D computed with the DRM19 mechanism. Finally, the 3D case is compared with a similar case in 2D in terms of turbulent burning velocity and generated flame surface area.

In Figure 4.1 the contours of the instantaneous mass fraction H_2, CH_4 and NO are given at cross sections $z = 0$. This gives an expression of the shape of the 3D flame. The first two species form the fuel in the mixture. The flame front is located in the thin region where the mass fractions vary. It can be seen that the variations of hydrogen are smoother compared to methane. This can be explained by the fact that Lewis number of hydrogen is relatively low (Le = 0.3) compared to methane (Le = 0.97). Therefore, hydrogen has a large molecular diffusion. Furthermore, a slow increase of NO mass fraction is observed and occurs in the burnt side of the flame. The maximum value of NO is small, because the combustion is lean and prompt NO is not included in the DRM19 mechanism.

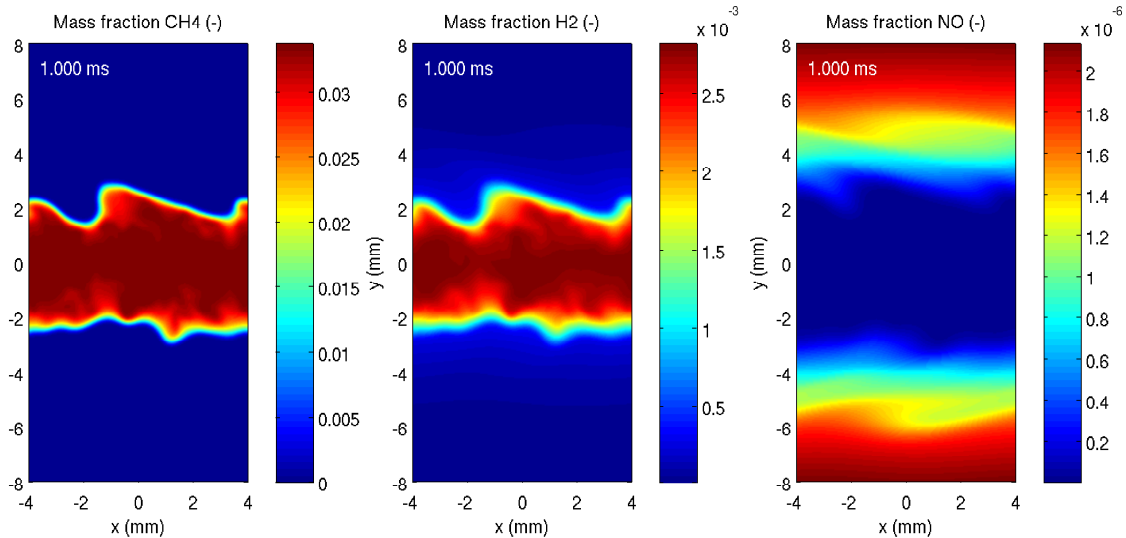Figure 4.1: Contours of the instantanous (t = 1 ms) mass fractions of CH_4, H_2 and NO in the cross section $z = 0$ mm for simulations of H40-3D

To analyse the effect of preferential diffusion on the flame further, the turbulent burning velocity can be calculated by

$$s_T = \frac{1}{\rho_0 Y_0 A_0} \int \int \int \dot{\omega}_{CH_4} dA, \qquad (4.5)$$

where ρ_0 is the unburnt density of the mixture, Y_0 is the mass fraction methane in the unburnt mixture and A_0 is the initial flame surface area. The integration is taken over the entire domain, therefore the turbulent burning velocity is a global parameter. It can be decomposed into contribution from the generated flame surface area A, the laminar burning velocity and a factor I accounting for turbulent influences on the turbulent burning velocity per unit area,

$$s_T = s_L^0 \cdot A \cdot I. \qquad (4.6)$$

It was already shown that the laminar burning velocity s_L^0 of the methane-hydrogen-air flame was a factor 1.5 higher than the methane-air flame. To make it easier to compare the two mixtures,

the turbulent burning velocity is made dimensionless by the laminar burning velocity. In Figure 4.2 the dimensionless turbulent burning velocity s_T/s_L^0 of the 3D flames are given as function of time. It can be seen that both flames show an enhanced turbulent burning velocity over time. At t = 1.0 ms the turbulent burning velocity is increased by approximately a factor 1.3. The flame surface area is the main factor for this increase.
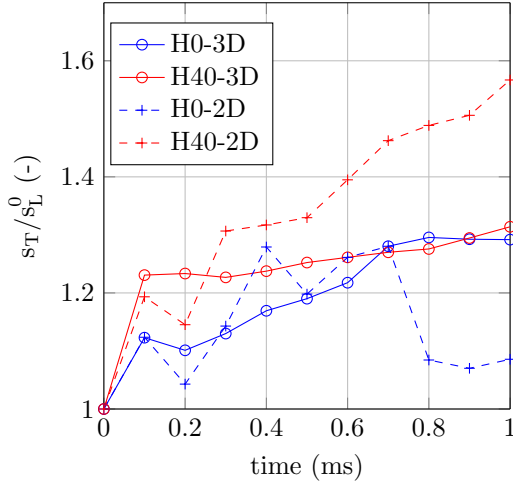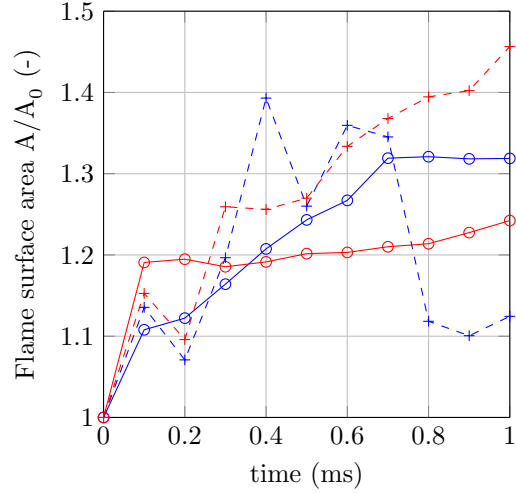

Figure 4.2: Turbulent burning velocity

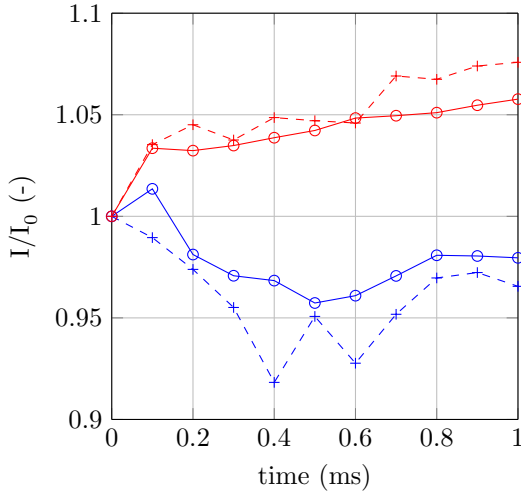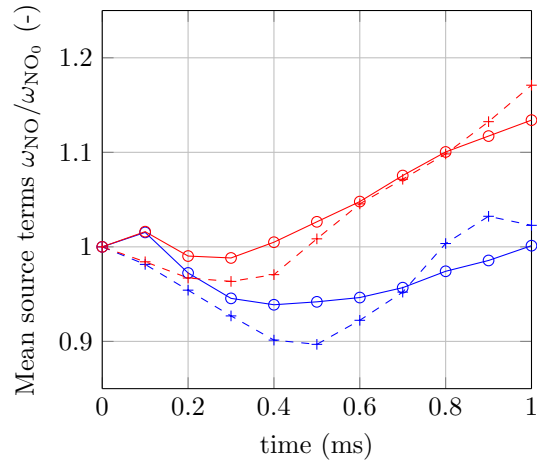Figure 4.3: Generated flame surface area

Figure 4.4: Turbulent influences on s_T per unit area

Figure 4.5: Normalized source term NO in the domain

In Figure 4.3 the increase in flame surface area is given. It is shown that flame surface is increased for both cases due to turbulence, but more flame surface is generated in the H0-3D case. Since the turbulent burning velocities where similar, a difference exists in turbulent-flame interaction between the cases. This can be seen in Figure 4.4 where the factor I is shown. In case H40-3D, the turbulence has on a positive effect on the turbulent burning velocity per unit area. The flames fall in the thin reaction zone regime, where small turbulent eddies can penetrate the preheat zone but do not influence the reaction layer. Sankaran et. al. simulated a spatially developing 3D Bunsen flame using a derived efficient detailed CH4air chemical mechanism [32]. They found thickening of the preheat zone due disturbance of turbulent eddies, despite the presence of a mean positive

strain rate. However, turbulence introduces flame stretch due to a curved and strained flame front. Therefore, preferential diffusion effects occur at the flame front. In hydrogen-enriched flames, the hydrogen is focused into regions of positive stretch. This leads to a locally higher equivalence ratio and thus a higher burning rate, which influences the turbulent burning velocity positively with a factor 1.06 at 1.0 ms.

The effect of preferential diffusion is illustrated by Figure 4.6, where the element mass fraction H at the flame front is given for the two different fuels. The element mass fraction H is normalized by it's laminar value on the flame front. It is shown that the element mass fraction H differs in regions in the methane-hydrogen-air flame. An increase of element mass fraction H is observed in regions convex towards the unburnt mixture (positive curvature). A decrease is seen in regions concave towards to unburnt mixture (negative curvature). However, these fluctuations in element mass fraction H are not seen in the methane-air flame where on average of slight decrease in element mass fraction H is seen, because in this flame the mass and heat diffusion are approximately equal.
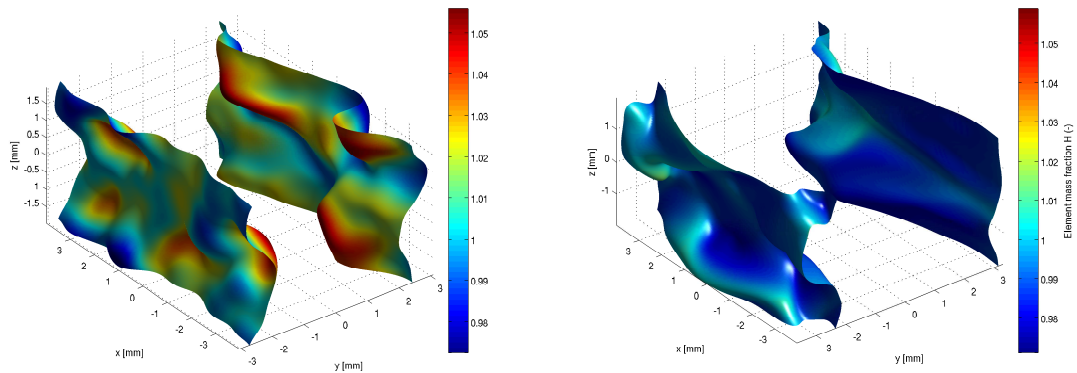

Figure 4.6: Normalized element mass Fraction H at flame front at t=1.0ms. Left: H40-3D. Right: H0-3D.

In Figure 4.5 the mean source terms of NO in the entire domain are given. It can be seen that the methane-hydrogen-air flame produces more NO than the methane-air flame. An initial decrease in NO production is visible for case H0-3D. This can be explained by the fact that more flame surface area in created with on average a negative curvature. As a result the unburnt fuel/air core, where source term NO are zero, increases compared to the burnt products layer. On the other hand, the increase of flame surface area results in a larger surface where NO can be produced. However, in the DRM19 mechanism only thermal NO is included, which is mainly produced at the burnt side of the flame. Therefore, the results in Figure 4.5 show little correlation with the generated flame surface area in Figure 4.3. It was already shown in section 2.4 that NO formation is under-predicted by the DRM19 mechanism with thermal NO, due to the absence of prompt NO production. Prompt NO is formed near the flame front. Therefore, a switch to the GRI3.0 mechanism is necessary to accurately predict the NO formation at the flame front. On the other hand, the GRI3.0 mechanism involves much more species and reactions compared to DRM19, which increases the computational costs.

4.3 2D results

Three-dimensional simulations are extremely computational expensive. To limit computational time, the same simulations are performed in two dimensions. The 2D results in terms of turbulent burning velocity and flame surface area are given in respectively Figure 4.2 and 4.3 together with the 3D results. It can be seen that the burning velocity clearly shows a different behaviour in 2D. This can be explained by the difference in generated flame surface area, which shows again a clear correlation with the turbulent burning velocity. It should be noted that 2D turbulence differs from 3D turbulence, since the vortex stretching mechanism is absent in 2D. Vortex stretching enhances vorticity and is the essential mechanism in the energy cascade from the large scale L_T to the small scale eddies η in turbulence [27]. Without vortex stretching, the energy cascade process is reversed. Kinetic energy is transferred from small to large eddies. However, in this thesis we are interested in the fundamental interaction between turbulence and flame and in particular on the difference between the two flames. In Figure 4.4 it can be seen that the influence of turbulent stretch on turbulent burning rate per unit area is well captured in the 2D simulations. Furthermore, the NO production, given in Figure 4.5, show quite similar results between 2D and 3D simulations. Two-dimensional simulations is necessary to limit the computational costs, especially since detailed chemistry is used. Therefore, in the remainder of this thesis only 2D flames are considered.

Hawkes and Chen performed 2D direct numerical simulations to study the influence of the hydrogen enrichment in turbulent premixed methane-air flames at $\phi = 0.52$ used a reduced chemical model consisting of 19 chemical species and 15 reaction steps [29]. They concluded that the turbulent burning velocity of the 29% hydrogen enriched flame is substantially higher than pure methane. This result was explained by three contributions. Firstly, the laminar burning velocity is increased in the enriched case, which is also found in this case. Secondly, they found an increase in generated flame area. Furthermore, it was found the turbulent factor I was enhanced by a factor 1.2 in the hydrogen-enriched flame. However, Hawkes and Chen used a swirl-stabilized combustor geometry where a constant mass flow of premixed fuel flows into a turbulent flow field, while a shear layer geometry is studied in this thesis. Hence, fuel burns away over time and eventually only complete burnt products are left in the domain. This can be seen in Figure 4.7, where the turbulent burning velocity is given until 3 ms. It can be seen that initially the turbulent burning velocity equals the laminar burning velocity. Furthermore, the hydrogen-enriched case burns faster than the methane-air flame and the flame surface, given in Figure 4.8 is strongly correlated with the turbulent burning velocity.
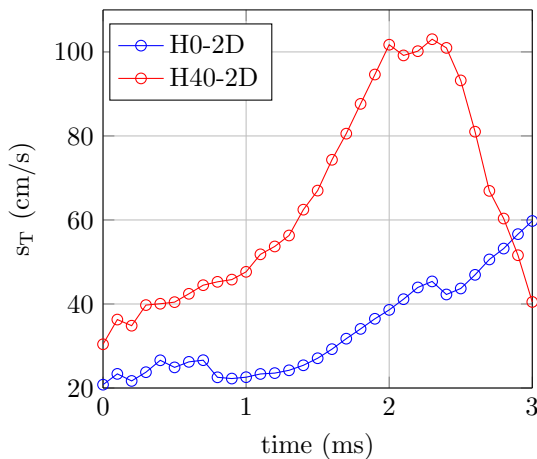

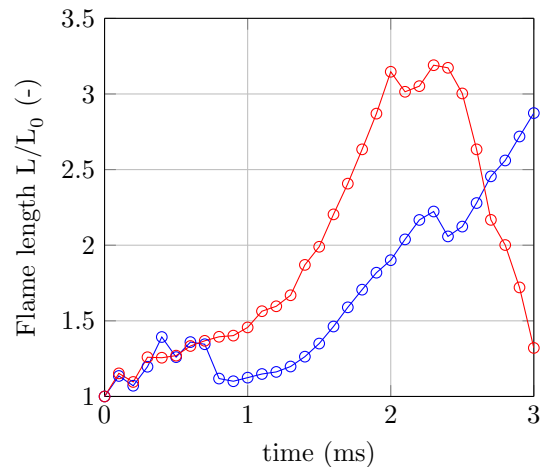Figure 4.7: The turbulent burning velocity.

Figure 4.8: Generated flame surface.

It might be expected that the hydrogen-enriched case always results in more flame surface area,

since preferential diffusion of H_2 into the positively curved regions enhance the local burning rate which leads to deeper cusps, broader curvature distribution and more flame surface area as found by Hawkes et. al. [29] and Zhu et. al [33]. However, in this study the turbulent unburnt fuel-air mixture triggers Kelvin-Helmholtz instabilities in the shear layer. This means that the flow field is inherently unstable [27]. Therefore, large flow structures will eventually always emerge and the flame surface will grow. On the other hand, it is shown in Figure 4.8 that the hydrogen enriched flame generates flame area faster than the pure methane flame, which contributes to a higher turbulent flame speed. Since turbulent burning velocity is higher, it is expected that the flame surface area is eventually less due to the greater rate of flame surface area consumption. This can be seen around 2 ms, where the amount of fuel left in the H40-2D case is such that the flame surface area can no longer sustain, causing the flame surface area and thus turbulent burning velocity to decrease. Therefore, time-averaging is not possible, since statistical stationarity is never achieved. It is therefore recommended to study the combined effects of unstable flow, preferential diffusion and difference in burning velocity on the generated flame surface area in a constant mass-flow case where time-averaging is possible, for instance in a Bunsen flame as done by Vreman et. al. [38] and Sankaran et. al. [32] or in a swirl-stabilized combustor as done by Hawkes et. al. [29] and Zhu et. al. [33].

4.4 Preferential diffusion effects

In this section preferential diffusion effects are discussed by comparing the turbulent methane-air flame with the methane-hydrogen-air flame. In Figure 4.9 the dimensionless element mass fraction Z_H/Z_H^0 is given for the turbulent flames. It can be seen that the methane-air flame shows almost no preferential diffusion of Z_H. However, in the methane-hydrogen-air flame clear preferential diffusion effects are visible, due to addition of the highly diffusive specie H_2. It can be seen that the element mass fraction H is enhanced in regions convex toward the reactants (positive curvature) and reduced in concave toward the reactants (negative curvature).
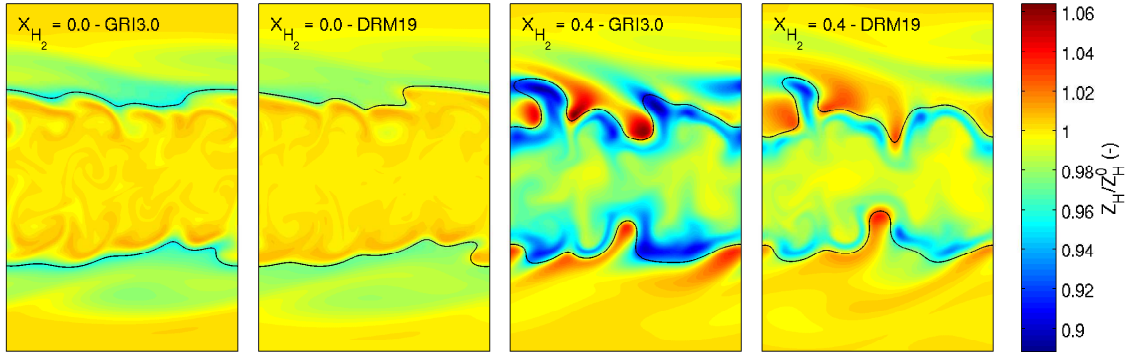

Figure 4.9: Element mass fraction Z_H/Z_H^0 of turbulent methane-hydrogen-air flames at the same flow time scale, t = 1.0 ms. The black line represents the inner layer.

This effect can be seen in Figure 4.10, which shows the mean interval average of the element mass fraction Z_H/Z_H^0 at the inner layer as function of curvature, $\kappa = \nabla \cdot \vec{n}$, for the simulations with the GRI3.0 mechanism. A clear positive trend is visible for the hydrogen enriched flame, while the methane-air case shows no trend. This positive correlation in the methane-hydrogen flame is due to preferential diffusion of H_2 in the positive curved areas. This can be verified in Figure 4.11, where the mass fraction Y_H normalized with the mass fraction Y_H^0 is presented versus curvature of the burnt flame front. In burnt flame front, most hydrogen reactions take place. The location of burnt flame front is here defined as the location where source term $\dot{\omega}_{CH_4}$ has decreased to 5% of its maximum value in the laminar flame.
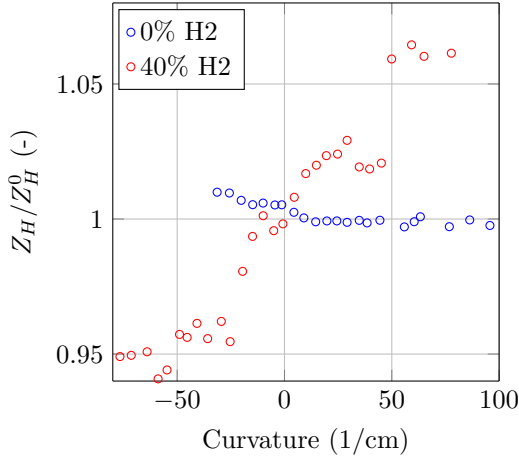
Figure 4.10: Element mass fraction Z_H/Z_H^0 at the inner layer as function of curvature
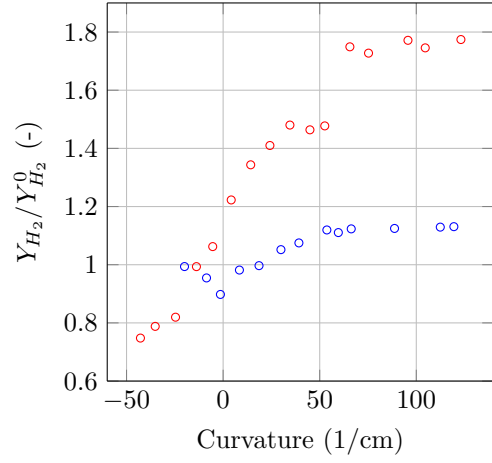

Figure 4.11: Mass fraction $Y_{H_2}/Y_{H_2}^0$ at the burnt side as function of curvature

As a result of preferential diffusion of species H_2, the reaction rates are influenced. This can be seen in Figure 4.12, where the mean interval average of the normalized source term of hydrogen $\dot{\omega}_{H_2}/\dot{\omega}_{H_2}^0$ is given at the burnt flame front. In positive curved areas of the flame the reaction rates are enhanced, while it is reduced in areas of negative curvature. The positively stretched parts of the flame become richer, which leads to a higher temperatures and turbulent burning rate of hydrogen. In Figure 4.14 the source terms of H_2 normalized by its laminar value are given in the domain. It can be seen that for in methane-hydrogen-air flame the source term can locally be increased by a factor 2.5, while the source terms of the methane-air flames stay close to unity. In the methane-air flame, hydrogen is an intermediate specie. Hence, it must first be created before it can be consumed. Therefore, the magnitude of source term $\dot{\omega}_{H_2}$ and species Y_{H_2} is in general lower than in the hydrogen enriched case. Furthermore, it is shown that methane-hydrogen-air flame is more curved than the methane-air flame due to the local difference burning rates. A higher/lower burning rate in the positive/negative curved regions increases curvature. From the Figures 4.10-4.13, it is visible that the hydrogen-enriched case has a broader curvature distribution. Hence, preferential diffusion effects enhance curvature.
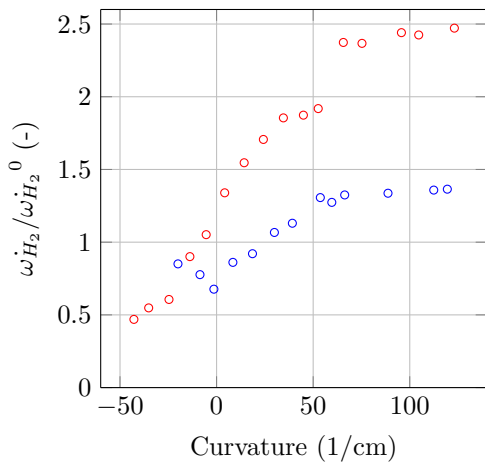

Figure 4.12: Source term $\dot{\omega}_{H_2}/\dot{\omega}_{H_2}^0$ at the burnt side as function of curvature
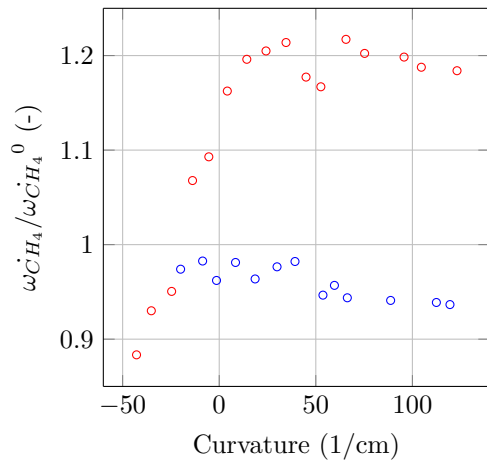

Figure 4.13: Source term $\dot{\omega}_{CH_4}/\dot{\omega}_{CH_4}^0$ at the burnt side as function of curvature

Preferential diffusion also effects the reaction rate of methane in a similar way. The enhanced temperatures due to local higher burning rate of H_2 results in a increase of the reactions rates in the region. This is amplified by the increased radical levels of H. In Figure 4.13 it can be seen that the source term of methane is positively correlated with curvature for the methane-hydrogen-air flame. However, the methane-air flame shows no correlation. This can be explained by the fact that methane has almost a unity Lewis number. Therefore, the preferential effects are small. In Figure 4.15 the source terms of CH_4 normalized by its laminar value are given. It can be seen that for the methane-hydrogen-air flame the source term can locally be increased by a factor 1.4, while the source terms of the methane-air flames stay close to unity.
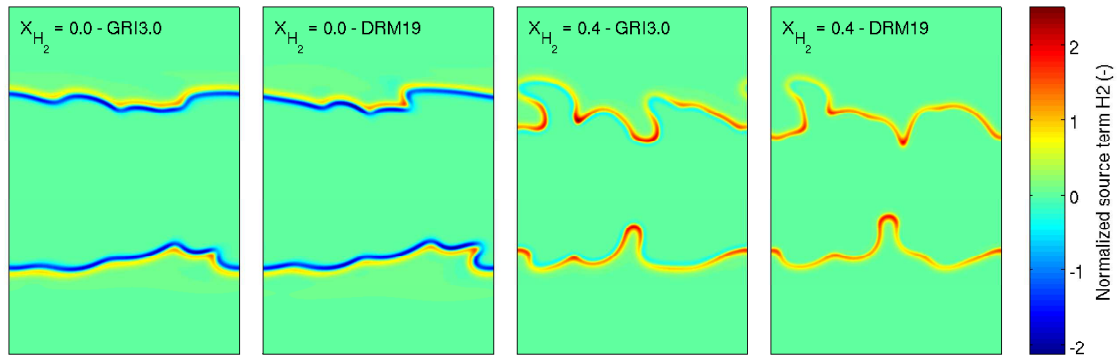

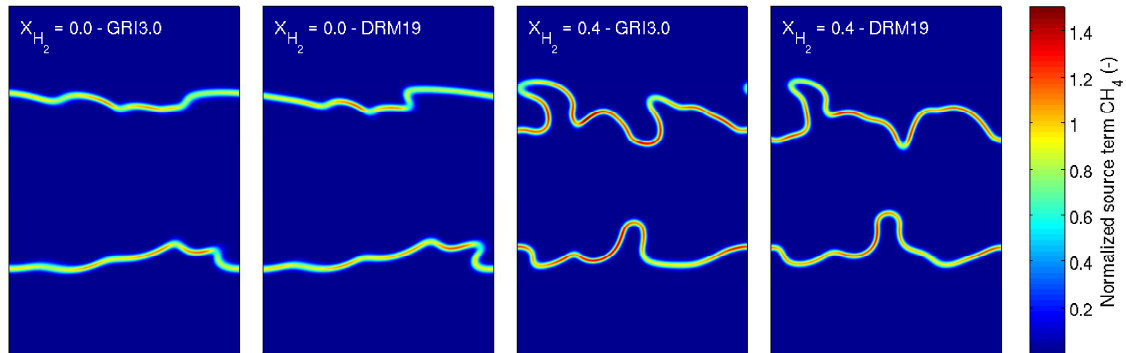Figure 4.14: Source term $\dot{\omega}_{H_2}/\dot{\omega}_{H_2}^0$ at the same flow time scale, t = 1.0 ms.

Figure 4.15: Source term $\dot{\omega}_{CH_4}/\dot{\omega}_{CH_4}^0$ at the same flow time scale, t = 1.0 ms.

4.5 Influence of turbulent intensity

To study the effect of turbulence to the flame, the initial turbulent intensity is increased by a factor 2. In the remainder of this chapter the simulations are performed using the detailed GRI3.0 mechanism, since this mechanism can accurately predict the NO formation with acceptable computational costs in two dimensions. In Figure 4.16 the turbulent burning velocity is given for the reference cases H0-2D, H40-2D and increased turbulent cases H0-2D-High, H40-2D-high, all computed with the GRI3.0 mechanism. It can be seen that when the turbulent intensity is doubled, the burning velocity is increased by a factor 4.3 and 2.6 compared to respectively the reference cases H0-2D and H40-2D. It is shown in Figure 4.17 that the enhanced flame surface area has the largest contribution to the turbulent burning velocity. A twice as large turbulent intensity results in a non-linear increase in flame surface area in both flames.
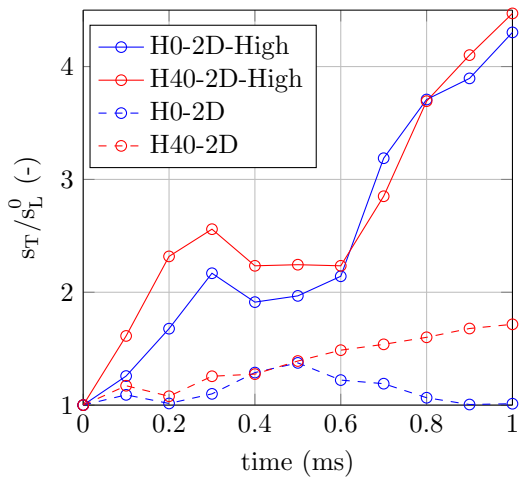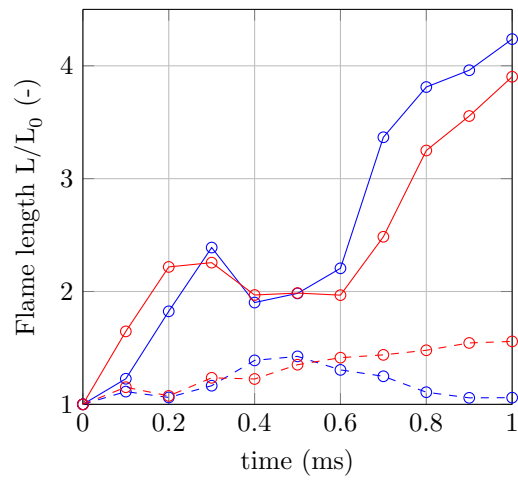

Figure 4.16: The turbulent burning velocity   Figure 4.17: Generated flame surface area
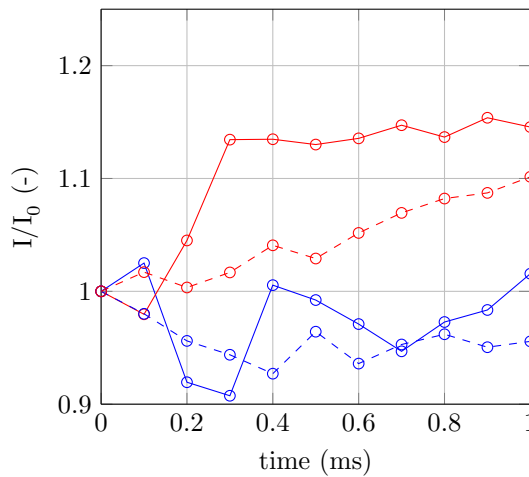
Figure 4.18: Turbulent influences on s_T per unit area

At high turbulence levels the fuel/air mixtures show a quite similar trend in terms of generated flame surface area, which might be an indication that the generated flame surface area is dominated by the flow due to the faster development of Kelvin-Helmholtz instabilities. Nevertheless the turbulence has still a positive effect on the burning velocity per rate of area in the hydrogen

enriched case, as is shown in Figure 4.18. It can be seen that the positive effect of turbulence on the turbulent burning velocity is larger for the higher turbulent intensity case. This is due to the higher stretch rates in the flame.

In Figure 4.19 the flame-area-weighted average stretch of the flame front due to strain and curvature $(s_d \nabla \cdot \vec{n})$ is given for the high and low turbulent intensity. It can be seen that the initially the flame front is unstretched. Furthermore, the stretch contributions are approximately of equal magnitude with a different sign. The flame stretch contributions are higher in the higher turbulent cases. The flame-area-weighted mean stretch rate of the hydrogen enriched case H40-2D (K = -377/s) and H40-2D-High (K = -144/s) is higher compared to the methane-air case H0-2D (K = -255/s) and H0-2D-High (K = -42.8/s). This is due to higher flame displacement speeds s_d and preferential diffusion effects in the methane-hydrogen-air flame, which tends to enhance the curvature and reduces the flame stability as discussed in more detail in Chapter 5. A decay of the stretch contributions over time is observed, which is due to the decay of turbulent intensity as shown in Figure 3.10. In Figure 4.24 the time evolution is given for case H0-2D-High. It can be seen that the initial turbulence vortices develop small wrinkled flame structures, which are relatively high strained and curved. These flame structures disturb the shear layer and triggers the Kelvin-Helmholtz instability. Therefore, a transition is seen from the initial turbulence dominated flame to larger flame structures.
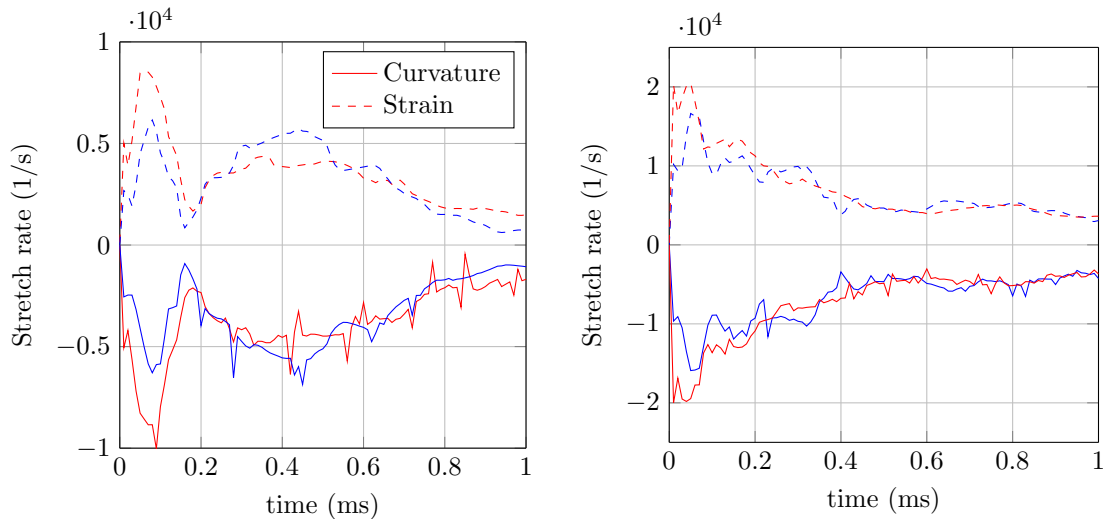

Figure 4.19: Contributions to flame stretch due to strain (dotted line) and curvature (solid line). Left: Case H0-2D (blue) and H40-2D (red). Right: Case H0-2D-High (blue) and H40-2D (red).

The curvature contributions in Figure 4.19 shows discontinuities. These peak occur due to locally extremely curved flame surface elements. In some cases this leads to a flame annihilation event. In Figure 4.20 an example of such a event in the H0-2D flame is given, where due to downstream interaction a pocket of reacting material is pinched off the flame front. The term downstream interaction is related to the situation where a flame element is sufficiently close to another flame element such that the two flame elements experience an interaction.

The difference in downstream interaction between the methane-air and methane-hydrogen-air flames can be studied by performing 1D simulations of stretched premixed flames in a planar stagnation flow in CHEM1D. In this flame topology, as seen Figure 4.23, two identical premixed fuel-air jets are impacted on each other and a stagnation plane is formed at x = 0. Only the negative x-values in the plane are considered, because the problem is symmetric. In Figures 4.21 and 4.22 the profiles of mass fraction CH_4 and CO are given for a laminar methane-hydrogen-air flame as function of distance in the plane with a relatively low and high applied strain rate. It can
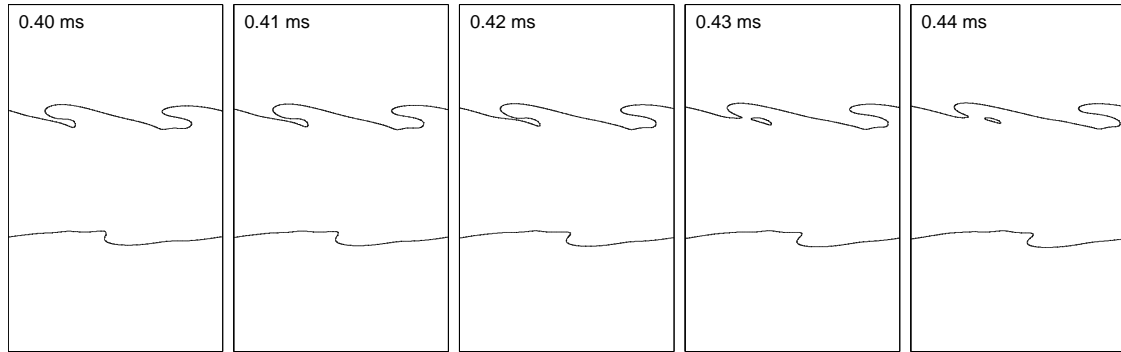
Figure 4.20: Pinch-off event in case H0-2D

be seen that for a low strain rate (K = 200/s) the flame is stabilized around x = -4 mm. At this strain rate the symmetric flames do not experience any downstream interaction from each other and the burning velocity remains almost unchanged, while for a high strain rate (K = 2000/s) the flame is pushed towards the stagnation plane and stabilizes within 0.5 mm from the stagnation plane. It can be seen that the oxidation of CO to CO_2 can no longer take place. The symmetric reaction layers interact and the burning velocity is reduced due to this incomplete combustion. Further increasing the strain rate above a critical value results in flame extinction.
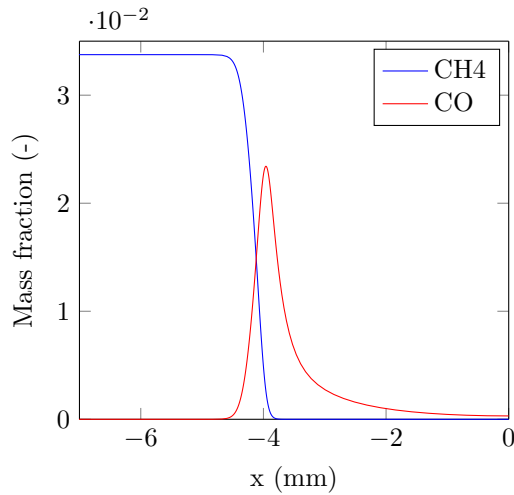
Figure 4.21: Low strain: K = 200/s
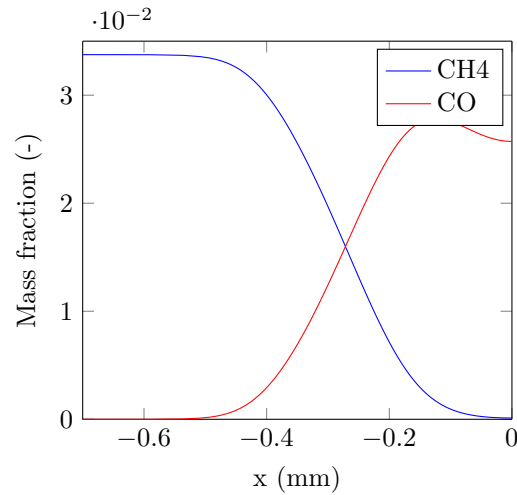
Figure 4.22: High strain, K = 2000/s

The extinction strain rate of the flames is determined by performing steady simulations with an increasing strain rate in CHEM1D. It is found that the critical strain rate of the methane-air flame is K = 1190/s, which is a factor 2.5 lower than the critical strain rate of K = 2950/s found for the methane-hydrogen-air flame. The reason for this large difference is partly flame timescale related. The methane-hydrogen-flame has a smaller flame timescale τ_f, which means the residence time of the flame in areas of high strain is smaller. By correcting for the difference in flame timescale $Ka = K\tau_f{}^0$, extinction occurs at Ka = 4.1 and Ka = 5.8 for the respectively methane-air and methane-hydrogen-air flame. The steady counterflow flow configuration is useful to point out the difference in extinction stretch rates. However, the flame-turbulence interaction introduce addition effects, due to unsteady flow and the relation between the turbulent length scale compared to that of the flame [25]. As a result the extinction Karlovitz number can differ. By assuming equal diffusivity for all species and isotropic homogeneous turbulence, the Karlovitz number can

be written as [11]

$$Ka = \left(\frac{v'_{rms}}{s_L}\right)^{3/2} \left(\frac{\delta_f}{L_T}\right)^{1/2}. \tag{4.7}$$

Hence, smaller turbulent eddies with turbulent length scale L_T should be more effective at quenching flames than larger eddies, since the stretch rate scales with δ_f/L_T. However, smaller sized eddies of the same order as the flame thickness δ_f are less capable of introducing curvature-induced stretch rates. Furthermore, due to heat release at the flame front, the viscosity is significantly increased. Consequently u'_{rms} is reduced due to high viscous dissipation in the preheat zone [25]. Therefore, small scale eddies in front of the flame vanish as they propagate across the flame.

It is shown in Figure 4.19 that the flames strain rates can be higher than their extinction strain rate. This is because a flamelet which experience no downstream interaction of another flamelet never extinguishes. This is confirmed by performing simulations of a stretched premixed flame impacted on it's hot burnt products (unburnt-to-burnt configuration) in CHEM1D, which is shown in Figure 4.23. It is found that the reaction zone is maintained at high strain rates due to the hot temperatures of the combustion products. Hence, a flamelet can differ in flame topology and stretch rate. In Figure 4.24 it can be seen that flamelets differ in flame configuration in the domain and as function of time. In the next section it is investigated how these turbulent methane-hydrogen-air flames influences the NO emissions.
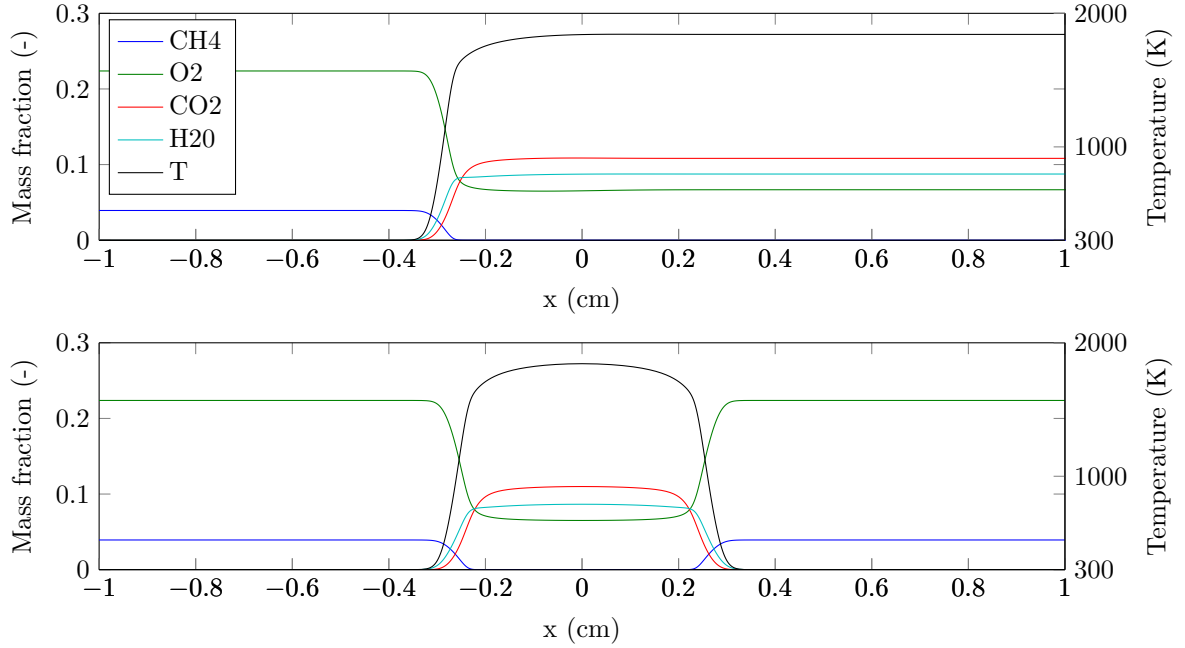

Figure 4.23: Different flame topologies of a methane-air flame. The stagnation plane is located at x = 0 mm. Top: the counterflow unburnt-to-burnt configuration at strain rate $a = 200/s$. Bottom: the counterflow twin jet configuration at $a = 200/s$
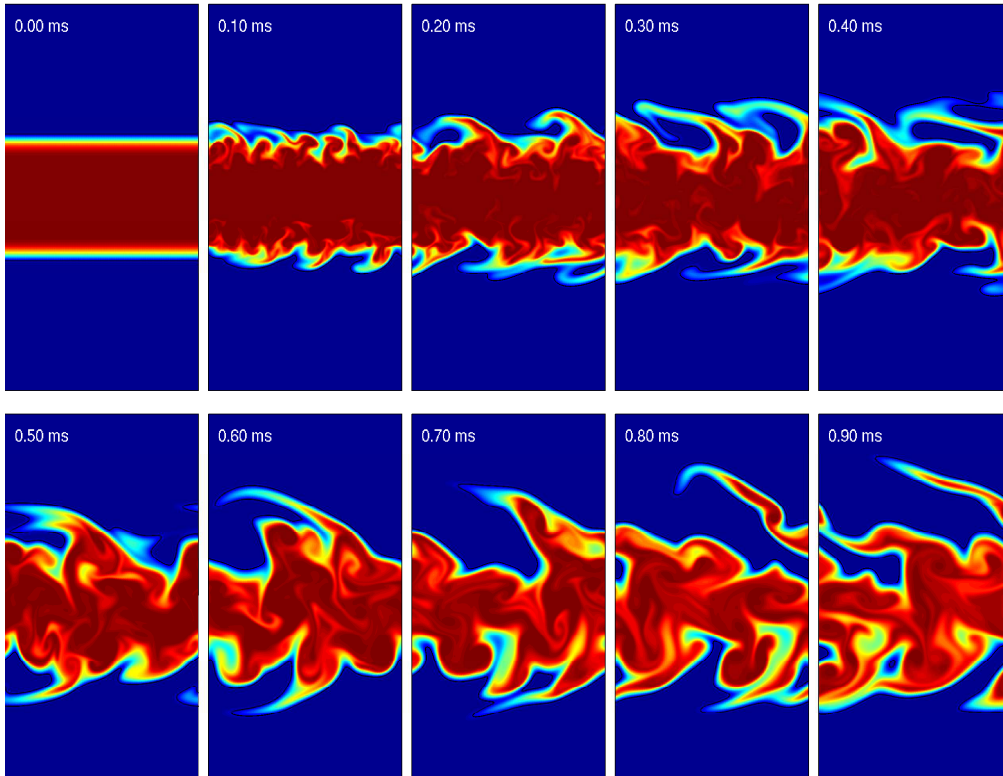
Figure 4.24: Case H0-2D-High: Development of the mass fraction CH_4 over time.

4.6   NO emissions

In this section the differences between methane-air and methane-hydrogen-air flames are discussed in terms of NO formation. In the previous section it was shown that the burning rates per unit area in methane-hydrogen-air flames is higher due changes in H_2 concentration. This affects the local equivalence ratio and thus local flame temperature and NO production. Hence, the addition of hydrogen to the fuel might have a negative impact on NO emissions, which is confirmed in this section.

In Figure 4.25 the mean source term of NO in the entire domain normalized by its initial value is given as function of time. It can be seen that the mean source term of the hydrogen-enriched cases H40-2D-High and H40-2D are higher than the pure methane-air cases H0-2D-High and H0-2D respectively. This is partly due to the increase of flame surface area, since prompt NO is produced near the flame front. In Figure 4.26 the mean source term is corrected for the difference in flame surface area. It shows that at on average more NO is produced in the methane-hydrogen-air flames. Over time, the mean source terms of the methane-hydrogen-air case H40-2D-High are 1.5 times higher compared to H0-2D-High, while for lower turbulence case H40-2D an increase of 1.12 is seen compared to H0-2D. These difference in NO production between the two flames indicate that the mean source term NO in the domain not only effected by the generated flame surface area.

To study the differences in more detail a progress variable is defined. Most NO emissions are formed at the burnt side further downstream in the flame, i.e. at high temperatures. This means a continuously increasing progress variable is sought. The mass fraction CH_4 alone is not a suitable progress variable, since no methane is left at the burnt side of the flame. By adding the mass
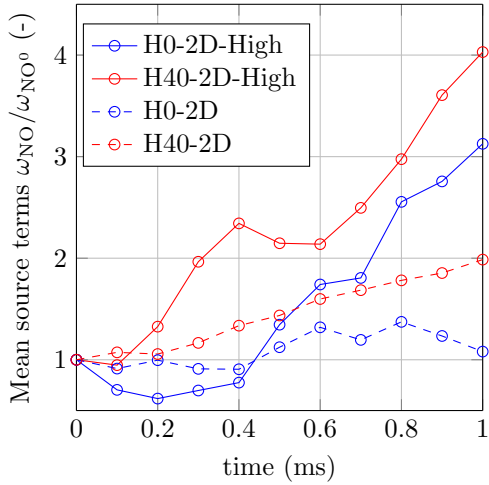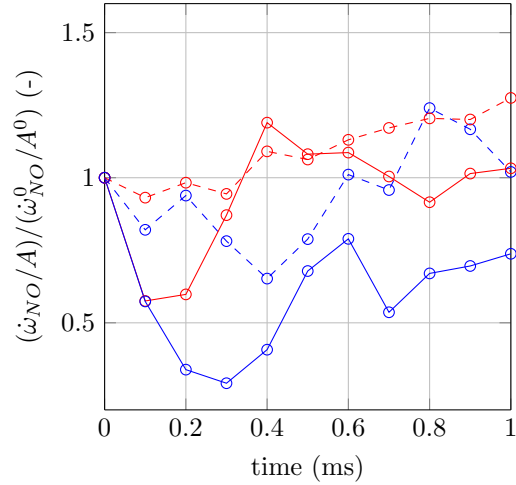
Figure 4.25: Mean source term $\dot{\omega}_{NO}/\dot{\omega}_{NO}^0$

Figure 4.26: Mean source term per unit area

fraction CO_2 the progress variable is continuously increasing at the burnt side of flame. Hence, the progress variable is given by

$$\mathcal{Y}^* = Y_{CO_2} - Y_{CH_4}, \tag{4.8}$$

and is scaled between 0 and 1 by

$$\mathcal{Y} = \frac{\mathcal{Y}^* - \mathcal{Y}_u^*}{\mathcal{Y}_b^* - \mathcal{Y}_u^*}, \tag{4.9}$$

such that it equals 0 at the unburnt and equals 1 at the completely burnt side. In Figure 4.27 and 4.28 the profiles of source term NO as function of the progress variable are given for the respectively methane-air flames and methane-hydrogen-air flames at t = 1.0 ms. For the DNS simulations, the data is averaged over intervals of $\mathcal{Y}$. By performing a mean interval average data scatter is reduced. It is shown that a negative part in the NO source exists. NO formed in the reaction zone of the flame diffuses towards the unburnt side, where the NO is consumed. It can be seen that the laminar unstretched methane-air flame produces less NO in general than the methane-hydrogen air flame, due to a higher flame temperature in the methane-hydrogen-air flame. However, in this thesis the equivalence ratio is fixed at $\phi = 0.7$. The methane-hydrogen-air flame potentially allows leaner combustion at lower equivalence ratio's, which leads to lower flame temperatures and thus lower NO emissions.

Furthermore, it can be seen that in Figure 4.27 that on average the turbulent methane-air flames shows no significant increase in NO source term compared to the laminar flame. On the other hand, the NO production in the turbulent methane-hydrogen-air flames is enhanced. It is shown in Figure 4.28 that an increase in turbulence leads to a higher source term NO at the burnt side. The average peak value at the burnt side in case H40-2D-High and H40-2D is respectively 1.7 and 1.3 times higher than in the laminar flame. This can be explained by the fact that due to preferential diffusion in the hydrogen-enriched cases, regions in the flame are locally richer. This results in higher radical levels, flame temperatures and thus an enhanced NO production. It is noted that local changes in equivalence ratio are not only caused by preferential diffusion, but can arise from imperfect mixing of the fuel and air in the unburnt premixed mixture [30].

In Figure 4.29 the influence of temperature difference on the source term NO at the value $\mathcal{Y}$ corresponding to the maximum source term NO is given. It can be seen that in both cases a higher temperature results in a higher source term NO. Furthermore, in Figure 4.30 the mean interval average of mass fraction of radical O is given as function of normalized source term NO. It is shown that on average more O radicals are formed in the H40-2D case. The O radical is
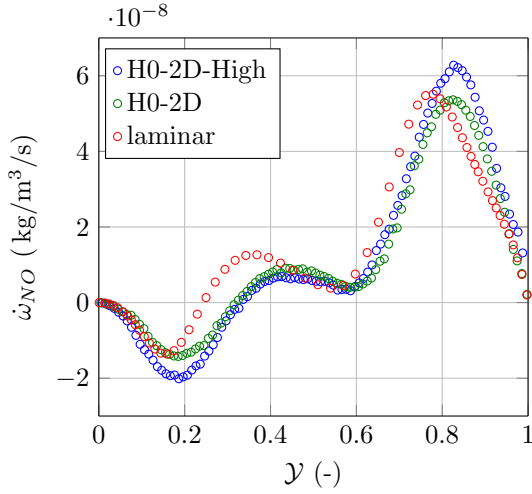
Figure 4.27: Source term $\dot{\omega}_{NO}$ versus $\mathcal{Y}$
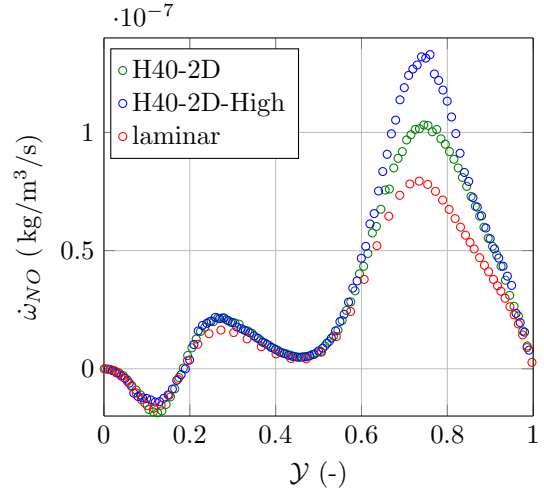
Figure 4.28: Source term $\dot{\omega}_{NO}$ versus $\mathcal{Y}$

an important specie in converting N_2 to NO [39] and positive correlation is seen between mass fraction O and source term NO for both cases. A similar trend is found for the radicals H and OH.
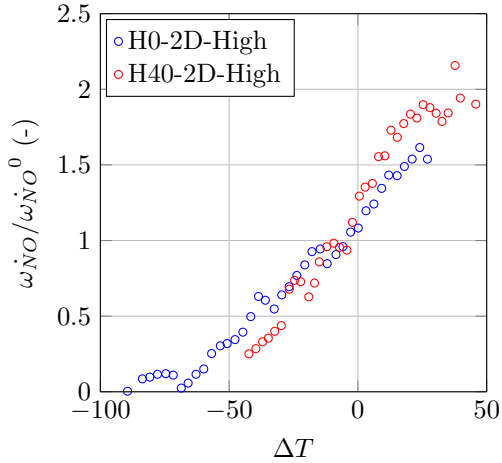
Figure 4.29: Scaled source term NO versus temperature difference at the burnt side of the flame
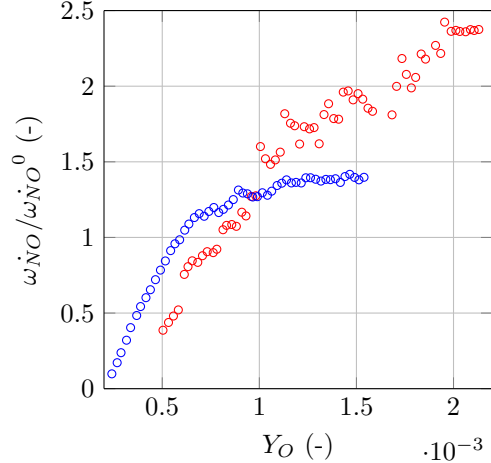
Figure 4.30: Normalized source term NO versus Mass fraction O at the burnt side of the flame

In Figure 4.31 the normalized NO source term is seen in the domain as function of time for the H0-2D and H40-2D case. The black line indicates the location of the flame front (maximum source term $\dot{\omega}_{CH_4}$). It is confirmed that most NO is produced further downstream. It can be seen that in case H40-2D, the NO source term is locally increased by a factor 2.1 compared to the maximum source term in the laminar hydrogen-enriched flame, while in the methane-hydrogen-air flame only a local increase of 1.3 is seen. Furthermore, it is shown that the increased levels of the source term NO in the methane-hydrogen-air flame are located in the positive curved regions of the flame (convex towards the unburnt mixture) or in areas with downstream interaction.

The influence of higher turbulence is clearly visible in Figure 4.32, where the source term NO of case H0-2D-High and H40-2D-High is displayed. Much larger flame structures are formed com-

Figure 4.31: The time evolution of source term NO normalized by it's maximum laminar value. Top: H0-2D. Bottom: H40-2D. Black line: Flame front.

pared to the cases H0-2D and H40-2D and as a result the ratio of reactants to products area is increased. This is the reason that the mean source term of NO per unit flame area in the entire domain, as given in Figure 4.26, is below unity for both cases. In the hydrogen-enriched case H40-2D-High the maximum source term levels are again seen in areas of positive curvature or downstream interaction. The maximum source term in the domain is 2.6 times higher than the maximum source term of the laminar flame. The formation of NO is a relative slow process compared the other chemical reactions [36]. Due to the enhanced source terms, more NO is produced which is convected away from the flame by the flow of burnt gases. Eventually the mass fraction NO in the flame is increased. This is shown in Figure 4.33 for case H40-2D-High, where at from 0.8 ms an increase in mass fraction NO is seen above the initial maximum mass fraction NO in the domain. After 1.0 ms the mass fraction NO is increased by 15%. For the other cases an increase in NO mass fraction is not observed. Furthermore, the methane-hydrogen-air flames seems more stretched than the methane-flames which might indicate a reduced flame stability. In the next Chapter the difference between the flames are discussed in terms of flame stability and preferential diffusion is investigated in more detail.
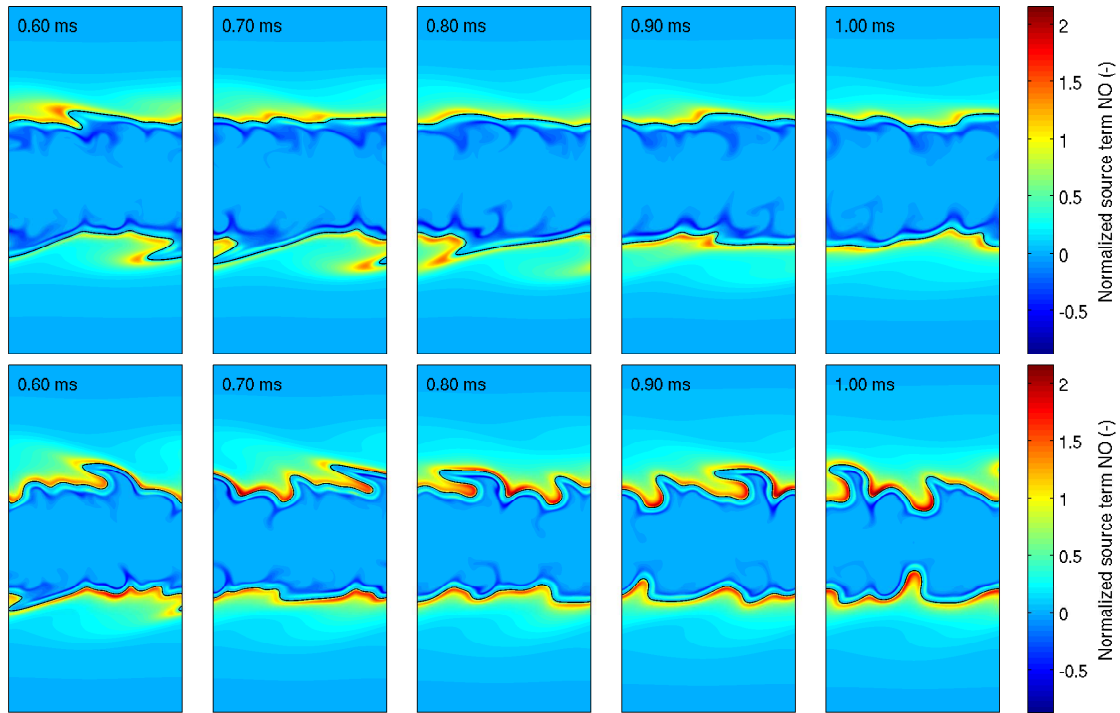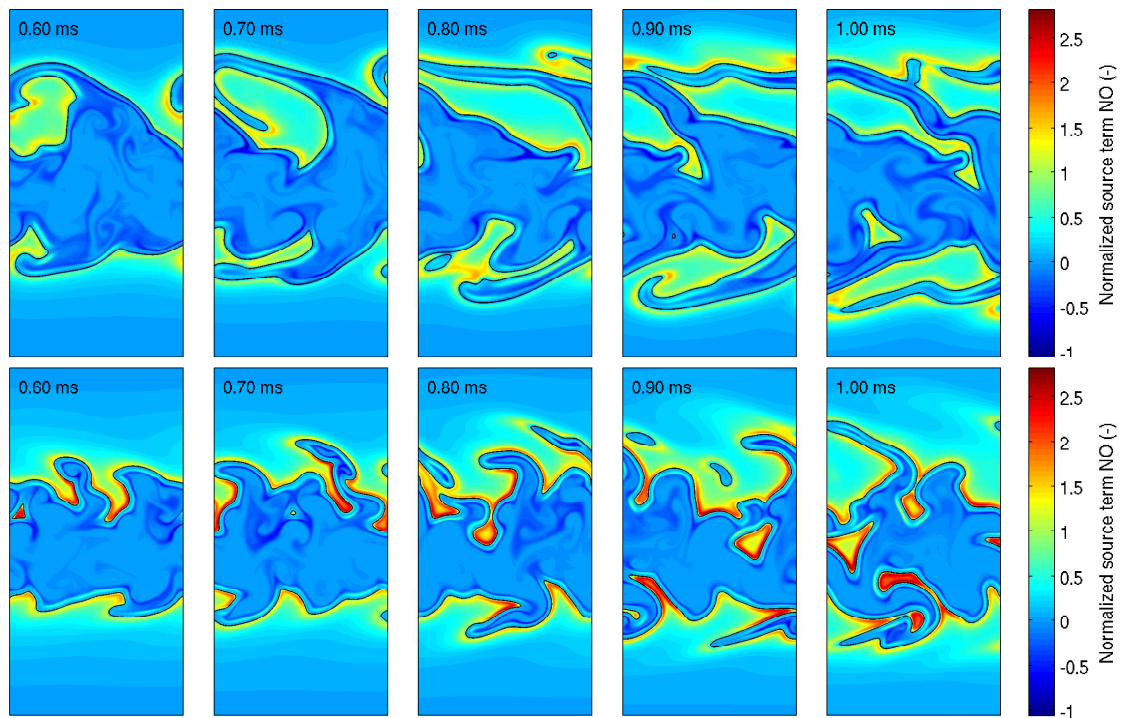
Figure 4.32: The time evolution of source term NO normalized by it's maximum laminar value. Top: H0-2D-High. Bottom: H40-2D-High. Black line: Flame front
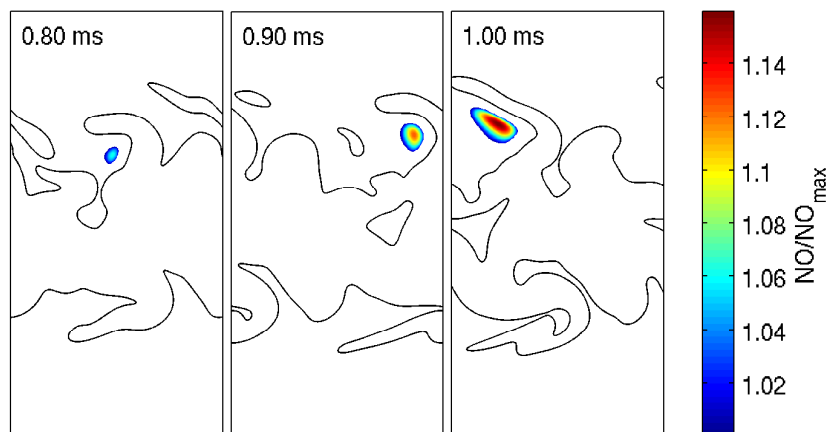

Figure 4.33: Time evolution of mass fraction NO scaled by the maximum mass fraction NO in the initial domain for case H40-2D-High. Only results where $NO/NO_{max}^0 > 1$ are shown. Black line: Flame front.

Chapter 5

Flame stretch and stability

In this chapter flame stretch and preferential diffusion effects are discussed. First, the flamelet equations following the stretch theory introduced by de Goey et al.[9] is presented. From these equations a model is derived to predict the mass burning rate for weakly stretched flames. In this model the stretched mass burning rate is related to the unstretched one as function of flame stretch and preferential diffusion terms. This model is validated by performing 1D simulations in CHEM1D [35] and the difference between methane-air and methane-hydrogen-air flames is discussed. Then, turbulent flamelets are extracted from 2D flame simulations and the effect of hydrogen addition on the mass burning rate and flame stability is investigated.

5.1   Flame Stretch Theory

A set of flamelet equations of premixed flames based on the full set of 3D unsteady conservation equations is derived by De Goey and Ten Thije Boonkkamp [7]. The flame is described in terms of iso-planes of a progress variable $\mathcal{Y}$, which can be any combination of species mass fractions. The progress variable is scaled to range from 0 in the unburnt mixture and 1 in the burnt mixture. The motion of a iso-surface of $\mathcal{Y}$ is given by the kinematic equation [26]:

$$\frac{\partial \mathcal{Y}}{\partial t} + \vec{v}_f \cdot \nabla \mathcal{Y} = \frac{\partial \mathcal{Y}}{\partial t} + \vec{v} \cdot \nabla \mathcal{Y} - s_d |\nabla \mathcal{Y}| = 0, \tag{5.1}$$

where the local velocity of the flame surface $\vec{v}_f$ is given by the sum of fluid velocity $\vec{v}$ and the local burning velocity $s_d \vec{n}$, $\vec{v}_f = \vec{v} + s_d \vec{n}$ and the local burning velocity s_d is defined as the displacement speed at the unburnt side of a flame. Furthermore, the unity normal vector is directed towards the unburnt mixture, defined as $\vec{n} = -\nabla \mathcal{Y}/|\nabla \mathcal{Y}|$. The stretch field K is defined as the relative rate of change of the mass M in a small control volume V moving with v_f inside the flame:

$$K = \frac{1}{M} \frac{dM}{dt} \text{ with } M = \int_{V(t)} \rho dV, \tag{5.2}$$

as defined in [8].With the kinematic Equation 5.1 and the definition of stretch K, the conservation equations of mass and $\mathcal{Y}$ can be rewritten in a orthogonal flame-adapted coordinate system [7]

$$\frac{\partial}{\partial s}(\sigma m) = -\sigma \rho K, \tag{5.3}$$

$$\frac{\partial}{\partial s}\left(\sigma m \mathcal{Y} - \sigma \frac{\lambda}{Le_i c_p} \frac{\partial \mathcal{Y}}{\partial s}\right) = \sigma \dot{\omega}_{\mathcal{Y}} - \sigma \rho K \mathcal{Y}. \tag{5.4}$$

where $m = \rho s_d$ is the mass burning rate, s is the arc length through a flamelet, λ is the thermal conductivity , c_p is the specific heat at constant pressure and σ is the surface area. The surface

area is related to local curvature by

$$\kappa = \nabla \cdot \vec{n} = -\frac{1}{\sigma}\frac{\partial \sigma}{\partial s}. \tag{5.5}$$

It can be seen that the left hand side of Equation 5.3 corresponds to mass convection, where the right hand side of Equation 5.3 for mass conservation within a flamelet represents the leaking/gain of mass in the two directions perpendicular to the flame surfaces. Furthermore, the first and second term in Equation 5.4 corresponds to convection and diffusion of $\mathcal{Y}$. The term involving $\dot{\omega}_{\mathcal{Y}}$ represents the source term, since $\mathcal{Y}$ is consumed/created by chemical reactions and the last term represents the leaking/gain of $\mathcal{Y}$ due to stretch. The full one dimensional quasi-steady conservation equation of species Y_i is given by [7]

$$\frac{\partial}{\partial s}(\sigma m Y_i) - \frac{\partial}{\partial s}\left(\sigma \frac{\lambda}{Le_i c_p}\frac{\partial Y_i}{\partial s}\right) = \sigma \dot{\omega}_{\mathcal{Y}} - \sigma \rho K h + \sigma Q_i, \tag{5.6}$$

where Q_i accounts for the diffusive transport along the flamelet and unsteady behaviour of species Y_i with respect to $\mathcal{Y}$ in the reference frame, given by

$$Q_i = \frac{dY_i}{dt} + \nabla \cdot (\frac{\lambda}{Le_i c_p}\nabla_{\|}Y_i), \tag{5.7}$$

in which $\nabla_{\|}$ is the gradient operator in tangential direction. Note that species Y_i is steady in the flame adapted coordinate system when it shows the same transient behaviour as $\mathcal{Y}$. The second term in Q_i describes transport in the flame surface which arise when the local iso-surfaces of Y_i are not parallel to the iso-surface of $\mathcal{Y}$. The unsteady effects Q_i in Equation 5.7 can be neglected in the laminar flames [7]. As a result the equation is steady and fully 1D [7]. For turbulent flames categorized in the thin reaction zone regime[28], the diffusive transport term in Q_i is still much smaller than the stretch term and can be neglected [26]. However, the time derivative has the same order of magnitude as stretch and can be written in the flame adapted coordinate system as [26]

$$\frac{dY_i}{dt} = \frac{\partial Y_i}{\partial t} + \vec{v}_f \cdot \nabla Y_i = (\vec{v}_f - \vec{v}_f^i) \cdot \nabla Y_i, \tag{5.8}$$

where $\vec{v}_f^i$ is the velocity of the iso-surfaces of Y_i. Which means that when species Y_i move with respect to $\mathcal{Y}$, a time derivative arises. In most cases, the order of magnitude of the time derivative is smaller because it is related to a velocity difference. It is assumed that in the remainder of this chapter that all the Q terms can be neglected. However, this quasi-steady state assumption might not be justified as shown in a later section.

The conservation of enthalpy h is given by

$$\frac{\partial}{\partial s}(\sigma m h) - \frac{\partial}{\partial s}\left(\sigma \frac{\lambda}{c_p}\frac{\partial h}{\partial s}\right) - \frac{\partial}{\partial s}\left(\sigma \frac{\lambda}{c_p}\sum_{i=1}^{N_s}\left(\frac{1}{Le_i}-1\right)h_i\frac{\partial Y_i}{\partial s}\right) = -\sigma \rho K h, \tag{5.9}$$

where again the left hand side represents convection and diffusion of enthalpy and the right hand side the leaking/gain of enthalpy within the flamelet. Note that enthalpy is always conserved, but local difference in enthalpy arise for non-unity Lewis numbers. Furthermore, stretched flamelets cause leakage of enthalpy along the flame surface.

A similar result is seen for the conservation of element mass fraction Z_j, which has the same structure as the conservation of enthalpy h conservation and is given by

$$\frac{\partial}{\partial s}(\sigma m Z_j) - \frac{\partial}{\partial s}\left(\sigma \frac{\lambda}{c_p}\frac{\partial Z_j}{\partial s}\right) - \frac{\partial}{\partial s}\left(\sigma \frac{\lambda}{c_p}\sum_{i=1}^{N_s}\left(\frac{1}{Le_i}-1\right)W_{ji}\frac{\partial Y_i}{\partial s}\right) = -\sigma \rho K Z_j, \tag{5.10}$$

where the right hand side represents the leaking of element j along the flame surface due to stretch. The Equations 5.3, 5.4, 5.6, 5.9 and 5.10 for respectively the conservation of mass, progress variable, species, enthalpy and element mass fraction are the full set of quasi-1D equations, named the Strongly Stretched Flamelet Equations. These equations form the basis for analysis of the influence of stretch on the mass burning rate.

5.2   Mass burning rate of 1D stretched flames

In this section the model introduced by De Goey and Ten Thije Boonkkamp [7] is presented. In this model it is assumed that the reaction layer is infinitely thin, which is valid when the reaction layer is much thinner than the preheating zone. The location of the inner layer is defined as the position in the flame where the chemical source term $\dot{\omega}_{\mathcal{Y}}$ is maximal. Integration of the mass conservation Equation 5.3 of a stretched flame results in

$$(\sigma m)_b - (\sigma m)_u = -\int_{s_u}^{s_b} \sigma \rho K ds, \tag{5.11}$$

with s_u the unburnt and s_b the burnt flame boundaries. In the same way Equations for enthalpy 5.9 and element mass fraction 5.10 can be integrated along the flamelet, where it has been used that all diffusive fluxes vanish in the unburnt and burnt gases

$$h_b - h_u = \frac{-1}{(\sigma m)_b} \int_{s_u}^{s_b} \sigma \rho K (h - h_u) ds, \tag{5.12}$$

$$Z_{j,b} - Z_{j,u} = \frac{-1}{(\sigma m)_b} \int_{s_u}^{s_b} \sigma \rho K (Z_j - Z_{j,u}) ds. \tag{5.13}$$

These equations show that mass, enthalpy and elements are not conserved in a flame path. By assuming an infinitely thin reaction layer and using the quasi-one-dimensional equation 5.4 for $\mathcal{Y}$, an approximation for the mass burning rate at the burnt side is found [9]

$$m_b(\mathcal{Y}_u, h_b, Z_{j,b}) \approx (1 - Ka) \, m_b^0(\mathcal{Y}_u, h_b, Z_{j,b}), \tag{5.14}$$

with Ka the Karlovitz integral given by:

$$Ka = \frac{1}{(\sigma m^0)_b} \int_{s_u}^{s_b} \sigma \rho K \mathcal{Y} ds. \tag{5.15}$$

Which shows that the stretched mass burning rate is related to the laminar mass burning rate with the burnt enthalpy and composition by the Karlovitz integral. However, the laminar mass burning rate m_b^0 still depends on the surface area $\sigma(s)$. It has been shown by Groot et al. [17] that the mass burning rate m^0 depends on the position s in the flame, but at the position of the inner layer s_i the mass burning rate m_i^0 is independent of curvature effects $\sigma(s)$. Also, the mass burning rate at the inner layer is more relevant, since most chemical activity takes place at the inner layer. By integrating the continuity Equation 5.3 between s_i and s_b and using $m_i^0 = m_b^0$, the following relation for the mass burning rate m_i at the inner layer is found

$$m_i = m_b + \int_{s_i}^{s_b} \sigma \rho K ds. \tag{5.16}$$

This then gives

$$\frac{m_i}{m_i^0} \approx (1 - Ka_i), \tag{5.17}$$

where m_i depends on the enthalpy h_i and element composition $Z_{j,i}$ at the inner layer and the Karlovitz integral given by

$$Ka_i = \frac{1}{(\sigma m^0)_i} \left(\int_{s_u}^{s_b} \sigma \rho K \mathcal{Y} ds - \int_{s_i}^{s_b} \sigma \rho K ds \right). \tag{5.18}$$

Which can be rewritten as

$$Ka_i = \frac{1}{(\sigma m^0)_i} \int_{s_u}^{s_b} \sigma \rho K \tilde{\mathcal{Y}} ds, \tag{5.19}$$

with $\tilde{\mathcal{Y}}$ a modified progress variable, defined as

$$\tilde{\mathcal{Y}} = \mathcal{Y} - H(s - s_i). \tag{5.20}$$

In which $H(s - s_i)$ is the Heaviside function that is equal to zero when $s < s_i$ and equal to 1 when $s > s_i$. This derivation is valid for all stretch rates under the assumption that the inner layer is infinitely thin.

For weak stretch rates, $Ka_i << 1$, the changes in enthalpy $h_i = h_i^0 + \Delta h_i$ and element composition $Z_{j,i} = Z_{j,i}^0 + \Delta Z_{i,j}$ are small. By using the simplification that flame surface $\sigma(s)$ is constant inside the flamelet $\sigma(s) = \sigma_i$, an Taylor expansion of Equation 5.17 can be derived, resulting in

$$\frac{m_i}{m_i^0} = 1 - Ka_i + \Delta\psi_i \cdot \frac{\partial \ln m_i^0}{\partial \psi_i} + h.o.t., \tag{5.21}$$

with $\Delta\psi_i = \psi_i - \psi_i^0$ the enthalpy and element distortion vector at the inner layer. Which yields:

$$\frac{m_i}{m_i^0} = 1 - Ka_i + \Delta h_i \frac{\partial}{\partial h_i^0}(\ln m_i^0) + \sum_{j=1}^{N_e-1} \Delta Z_{j_i} \frac{\partial}{\partial Z_{j_i}^0}(\ln m_i^0) + h.o.t., \tag{5.22}$$

where the sensitivity coefficients $(\partial \ln m_i^0)/(\partial \psi_i)$ are given in Table 5.1, taken from [26]. The first term on the right hand side of Equation 5.21 represents the direct stretch effect, due to a loss/gain of mass inside a flamelet due to positive/negative stretch. The second term on the right hand side in Equation 5.21 represent the preferential diffusion effect. Which is related to the changes in enthalpy Δh_i and element mass fraction ΔZ_{j_i} of C,H and O.

Table 5.1: Coefficients $(\partial \ln m_i^0)/(\partial \psi_i)$ for methane-air mixtures [26]

ψ_i	$\phi = 0.6$	$\phi = 0.8$
Z_C	100	45
Z_H	400	190
Z_O	2.3	4.7
h (J/kg)	3.8	2.2

5.3 Comparison with numerical results

To analyse the role of the preferential diffusion terms in Equation 5.21, numerical simulations are performed of freely adiabatic stretched methane-hydrogen-air flames with the GRI3.0 mechanism at a equivalence ratio of 0.7. The sensitivity coefficients in Table 5.1 are taken from van Oijen [26]. To obtain the sensitivity coefficients for $\phi = 0.7$, the values in Table 5.1 are linear interpolated.

In Figure 5.1 the changes in enthalpy and element mass fraction multiplied by the sensitivity coefficients are given as function of the Karlovitz integral. It can be seen that the changes in Z_C and enthalpy have the largest contribution to the mass burning rate of the lean methane air flame, while the changes in Z_H and Z_O are negligible. Furthermore, the change in element mass fraction Z_C and enthalpy have an opposite effect on the mass burning rate. However, the sum of the contributions results in a nett positive effect on the mass burning rate. When 40% hydrogen

is added to the fuel, the contribution of Z_H is significantly increased, while the contribution of Z_C decreases. This results in a net larger total positive effect on the mass burning rate compared to the methane-air flame.
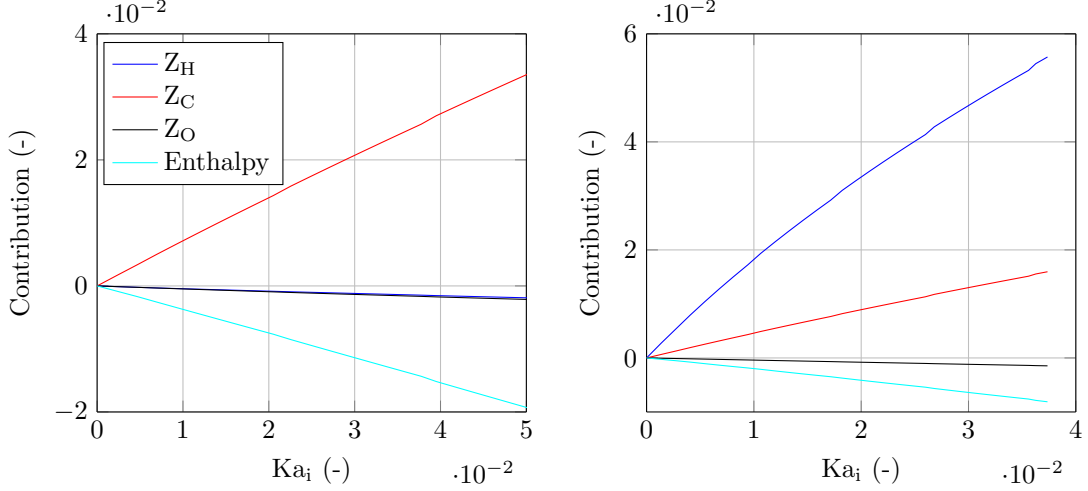

Figure 5.1: Contribution $\Delta\psi_i(\partial \ln m_i^0)/(\partial\psi_i)$ to mass burning rate m_i/m_i^0. Left: stretched methane-air flame. Right: stretched methane-hydrogen-air flame with $X_{H_2} = 0.4$

In Figure 5.2 the normalized mass burning rated of the methane-hydrogen-air flame with $X_{H_2} = 0$ and 40% is given as function of dimensionless stretch. It can be seen that the numerical results of the methane-air flame agree well with the theory. Furthermore it can be seen that the mass burning rate of the methane-air flame decreases with stretch. Which means the direct stretch effect, due to the first term in Equation 5.21 is larger than the preferential diffusion contributions. Visa versa is seen for the case with hydrogen added. The preferential diffusion effect is larger than the direct stretch effect. For the methane-hydrogen-air flame the theory over-predicts the mass burning rate. The reason might be related to the sensitivity coefficients used in Table 5.1, which are optimized for pure methane-air flames.
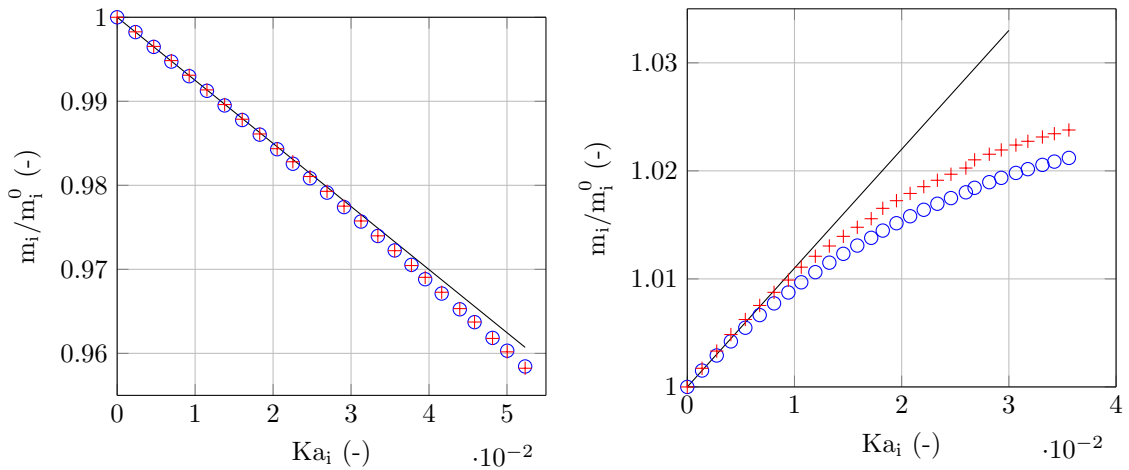

Figure 5.2: Normalized mass burning rate at the inner layer versus stretch. Left: methane-air flame. Right: methane-hydrogen-air flame with $X_{H_2} = 0.4$. Blue dots: Numerical solutions of stretched free flame. Red marker: Theory. Black line: $1\text{-}\mathcal{M}Ka_i$

For weak stretch the preferential diffusion terms be written as a linear function of Ka_i,

$$\Delta h_i \frac{\partial}{\partial h_i^0}(\ln m_i^0) + \sum_{j=1}^{N_e-1} \Delta Z_{j_i} \frac{\partial}{\partial Z_{j_i}^0}(\ln m_i^0) = CKa_i, \tag{5.23}$$

which results in

$$\frac{m_i}{m_i^0} = 1 - (1-C)Ka_i = 1 - \mathcal{M}Ka_i, \tag{5.24}$$

where $\mathcal{M}$ is the Markstein number, which describes the sensitivity of the mass burning rate to stretch. The Markstein number is determined by taking the slope at $Ka_i = 0$. This results in $\mathcal{M}$ = 0.75 and -0.11 for respectively the flame with $X_{H_2} = 0$ and 0.4. In Figure 5.2 the normalized mass burning rate predicted by Equation 5.24 is shown. It can be observed that the mass burning rate of the methane-air flame has a more linear relation as function of stretch compared to the mass burning rate of the methane-hydrogen-air flame. However, for weak stretch $Ka_i < 0.01$ the mass burning rate can be predicted by Equation 5.24.

As a results it can be concluded that when hydrogen ($Le_{H_2} = 0.3$) is blended with methane ($Le_{CH_4} = 0.97$), the preferential diffusion effect becomes stronger. Due to stretch the element mass fraction H is significant increased in the flamelet. The preferential diffusion effect becomes larger than the direct stretch effect. As a result the Markstein number changes sign. Therefore, the thermal-diffusive stability of the methane-hydrogen-air flame is vanished and the flame is unstable. Which might lead to sharper cusps, an increased flame surface area and cellular structures in turbulent flames. Hence, the relation between flame stretch and preferential diffusion determine whether a flame is stable or unstable.

5.4 Flame stability

The stability of a flame depends on the flame speed and flow velocity. The local mass burning rate determines the local flame speed. In the previous section we have seen that the local mass burning rate is influenced by changes in enthalpy and element mass fraction due to preferential diffusion. Darrieus and Landau showed that all flames are in the basis unstable due to thermal expansion in the flame [6, 23].
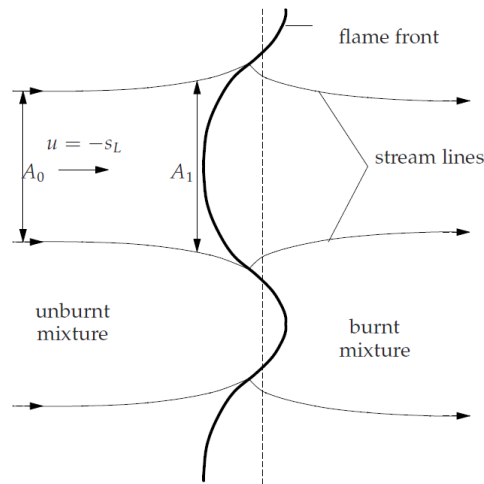

Figure 5.3: The Landau-Darrieus instability, taken from de Swart[11]

In Figure 5.3 the hydro-dynamic instability of Landau en Darrieus is displayed. Thermal expansion in the flame front causes the streamlines to bent towards the local normal vector to the front

and causes the flow velocity perpendicular to the front to increase. As a result the flow diverges in front of the flame front regions convex towards the unburnt mixture (positive curvature), causing the local velocity ahead of the front to decrease. When the flow velocity decreases and becomes smaller than the burning velocity s_d, the positive curved region will grow. Visa versa for the flame front regions concave towards the unburnt mixture (negative curvature). Hence, the flame is hydro-dynamically unstable.

However, in practice stable flames exist. In the previous section it was shown that the mass burning rate can locally differ in a flame due to stretch. Therefore, flame stretch can have a stabilizing effect on the flame when the burning velocity decreases in positive stretched flames. If $Le > 1$, preferential diffusion amplifies the stabilizing effect, while a flame with $Le < 1$ the instability is enhanced in positive stretched regions due to preferential diffusion [11]. By blending hydrogen ($Le = 0.3$) with methane ($Le = 0.97$), the Lewis number of the fuel is reduced. In the laminar case this results in a change of sign in the Markstein number. This response might enhance the hydrodynamic instability and cause an unstable flame. In a turbulent flame with $Le << 1$, the burning velocity is relatively high in regions convex toward the reactants (positive curvature) and low in regions concave toward the reactants (negative curvature). Consequently curvature and flame surface area grow. This will not occur when the mass burning rate is respectively lower and higher in the convex and concave regions, which is the case for flames with $Le \geq 1$. [38].

In Figure 5.4 and 5.5 different iso-contours of methane are given for the turbulent case H0-2D and H40-2D. It can be seen that at the same flow time scale, the turbulent methane-hydrogen-air flame shows sharper cusps and a larger flame surface area compared to the methane-air flame. The same result can be seen at the same flame time scale. Which indicates that the flame stability is also reduced in turbulent flames. To investigate this effect further, turbulent flamelets are extracted to compute the mass burning rate and Markstein number as function of dimensionless flame stretch.
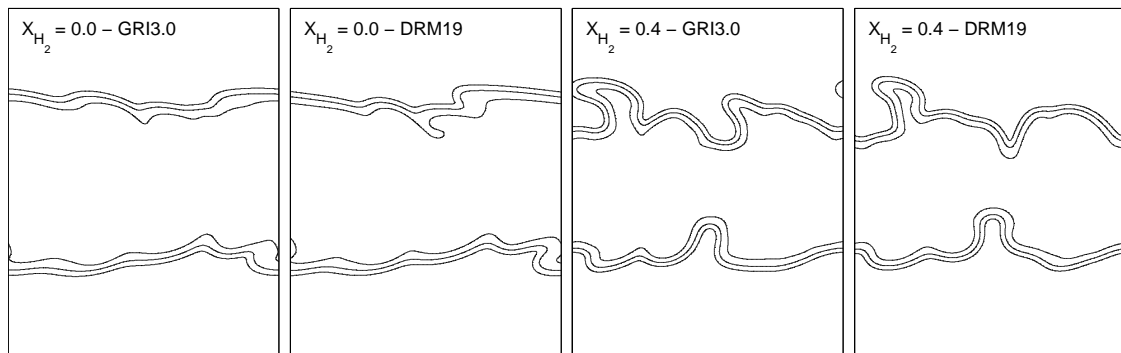

Figure 5.4: Iso-contours of $\mathcal{Y}_{CH_4}$ of turbulent methane-hydrogen-air flames at the same flow time scale, t = 1.0 ms.
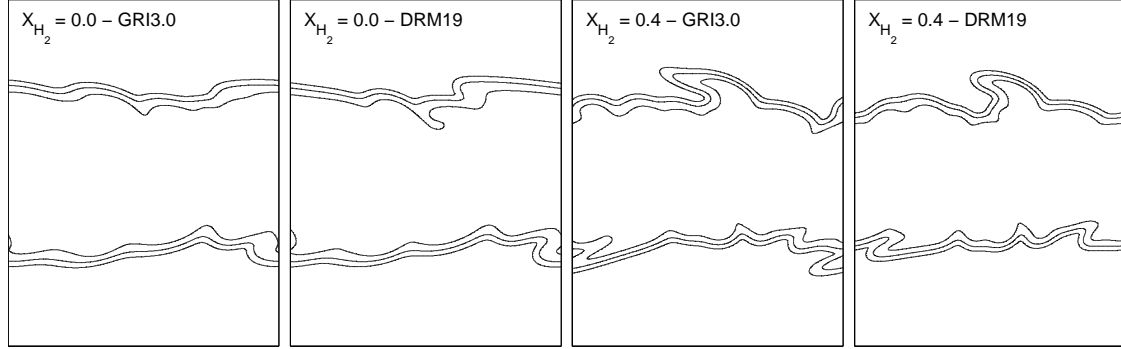
Figure 5.5: Iso-contours of $\mathcal{Y}$ of turbulent methane-hydrogen-air flames at the same flame time scale, $t/\tau_f = 0.28$.

5.5 Turbulent flamelet extraction

As presented in the previous sections, the strong stretch theory introduced by De Goey and Ten Thije Boonkkamp [7] shows that the local mass burning rate is related to the unstretched mass burning rate m_i^0 and dimensionless stretch rate, given by the Karlovitch integral Ka_i. In order to determine the influence of hydrogen-enrichment to the flame stability, the DNS results of case H0-2D and H40-2D are used. In this section a flamelet analysis is performed as described in the previous sections. Therefore, flamelets are extracted from 4 simulations, two different mixtures of methane-hydrogen-air, $X_{H_2} = 0$ and X_{H_2} with the two chemical mechanism, DRM19 and GRI3.0, as displayed in Figure 5.4.

The flamelet path $\vec{x}(s)$ is determined by identifying cells where the inner layer is located. The progress variable has the a certain value $\mathcal{Y} = \mathcal{Y}_i$, which corresponds to the position where the source term of the progress variables $\dot{\omega}_{\mathcal{Y}}$ reaches its maximum value in the laminar flame. As a result an iso-surface of the progress variable can be found. As mentioned before, the stretch theory assumes a infinitely thin reaction zone. Methane is consumed fast in a thin reaction layer. Which means the chemical source term $\dot{\omega}_{CH_4}$ has a negligible influence on the preheat zone. For this reason methane is chosen as progress variable, given by

$$\mathcal{Y}_{CH_4} = \frac{Y_{CH_4} - Y_{CH_4,u}}{Y_{CH_4,b} - Y_{CH_4,u}}, \tag{5.25}$$

which is scaled such that it equals 0 at the unbunt side and 1 at the burned side. For a flame of finite thickness, enclosed between iso-surfaces $\mathcal{Y}(\vec{x}, t) = \mathcal{Y}_u$ and $\mathcal{Y}(\vec{x}, t) = \mathcal{Y}_b$, flamelet paths $\vec{x}(s)$ are extracted as curves crossing the from the unburnt side to the burnt side in the flame in the direction of the normal $\vec{n}$

$$\vec{x}(s) = \vec{x}_u - \int_{s_u}^{s} \vec{n} ds', \tag{5.26}$$

which are generally not straight lines ($\sigma \neq 1$). Each extracted flamelet consists of 1000 grid points, interpolated between the cells by using a fourth order polynomial interpolation. When the flame path is known, the local mass burning rate can be determined by using the conservation of progress variable $\mathcal{Y}$

$$\rho \frac{\partial \mathcal{Y}}{\partial t} + \rho \vec{v} \cdot \nabla \mathcal{Y} - \nabla \cdot (\frac{\lambda}{Le_i c_p} \nabla \mathcal{Y}) = \dot{\omega}_{\mathcal{Y}}. \tag{5.27}$$

By using the kinematic Equation 5.1 this results in

$$\rho s_d |\nabla \mathcal{Y}| = \nabla \cdot (\frac{\lambda}{Le_i c_p} \nabla \mathcal{Y}) + \dot{\omega}_{\mathcal{Y}}, \tag{5.28}$$

where ρs_d is defined as the local mass burning rate m. Hence, the local mass burning rate depends on the chemical source term of $\mathcal{Y}$ and the local diffusion flux, given by

$$m = \frac{\nabla \cdot (\frac{\lambda}{Le_i c_p} \nabla \mathcal{Y}) + \dot{\omega}_{\mathcal{Y}}}{|\nabla \mathcal{Y}|}. \tag{5.29}$$

Furthermore, the stretch field is calculated by combining the continuity Equation 2.12 with the mass-based stretch Equation 2.9

$$K = \frac{1}{\rho}\frac{d\rho}{dt} + \nabla \cdot \vec{v_f}, \tag{5.30}$$

and by using the relation $\vec{v_f} = \vec{v} + s_d\vec{n}$. Which results in the following equation for stretch K

$$\rho K = \nabla \cdot (m\vec{n}). \tag{5.31}$$

Flamelets are extracted at t = 1.0 ms for cases H0-2D and H40-2D, from which some iso-contour levels are shown in Figure 5.4. In Figure 5.6 the profiles of the progress variable $\mathcal{Y}$, the dimensionless stretch rate $\rho_u K \delta_f / m_i^0$ and scaled flame surface area σ/σ_i are presented for different flamelets simulated with the GRI3.0 mechanism. The arc-length s of each flamelet is scaled with the flame thickness δ_f. The left and right side of Figure 5.6 corresponds to the results of respectively case H0-2D and H40-2D. It can be seen that in the preheating zone, the profiles of $\mathcal{Y}$ are disturbed by turbulent eddies compared with laminar profile indicated with red. For the methane-hydrogen-air flame this effect is stronger and more variations in flame thickness can be seen. This is due to the smaller flame thickness of the hydrogen-enriched flame compared to the methane-air flame. Furthermore, the profiles of $\mathcal{Y}$ are almost not changed near the inner layer $s=s_i$. This is a property of the thin reaction zone where the smallest flow structures can not penetrate the reaction layer, since the flame thickness is smaller than the largest eddies in the flow [28].

Moreover, it can be seen that in both cases the stretch rates varies a lot as function of s. Flame stretch is only defined in the area where unit normal vector $\vec{n} = -\nabla \mathcal{Y}/|\nabla \mathcal{Y}|$ is not zero, see definition 5.31. The dimensionless stretch rate $\rho_u K \delta_f / m_i^0$ is in the order of 10, which means the flame experiences relative large stretch rates. As a result, the weak stretch approximation for the mass burning rate m_i given by Equation 5.22 no longer hold and the stretch rate can not be neglected in the Karlovitz integral Ka_i. Note that although the stretch rates are relative high, they vary al lot in a flame let. Therefore, integrating these stretch rates over the arc-length does not necessary result in a high Karlovitch integral Ka_i.

Furthermore, it is shown in Figure 5.6 that the flame surface area σ/σ_i varies as function of arc-length s. For some flamelets the derivative of σ with respect to s/δ_f is larger than δ_f^{-1}. The derivative of σ is related to curvature κ by Equation 5.5. Which means the flame thickness is larger than the curvature radius, $\delta_f > 1/\kappa$, and the flame surface area σ can not be neglected in the Karlovitz integral Ka_i.

As a result the complete profiles of progress variable $\mathcal{Y}$, the stretch rate K and scaled flame surface area σ/σ_i are required to calculate the Karlovitz integral of each flamelet, given by Equation 5.19. The integral boundaries s_u and s_b are chosen at the location where $\mathcal{Y}$ is respectively $\mathcal{Y} = 0.05$ and $\mathcal{Y} = 0.99$. The Karlovitz integral can be used to investigate the influence of flame stretch to the mass burning rate for different turbulent methane-hydrogen-air flames, presented in the next section.
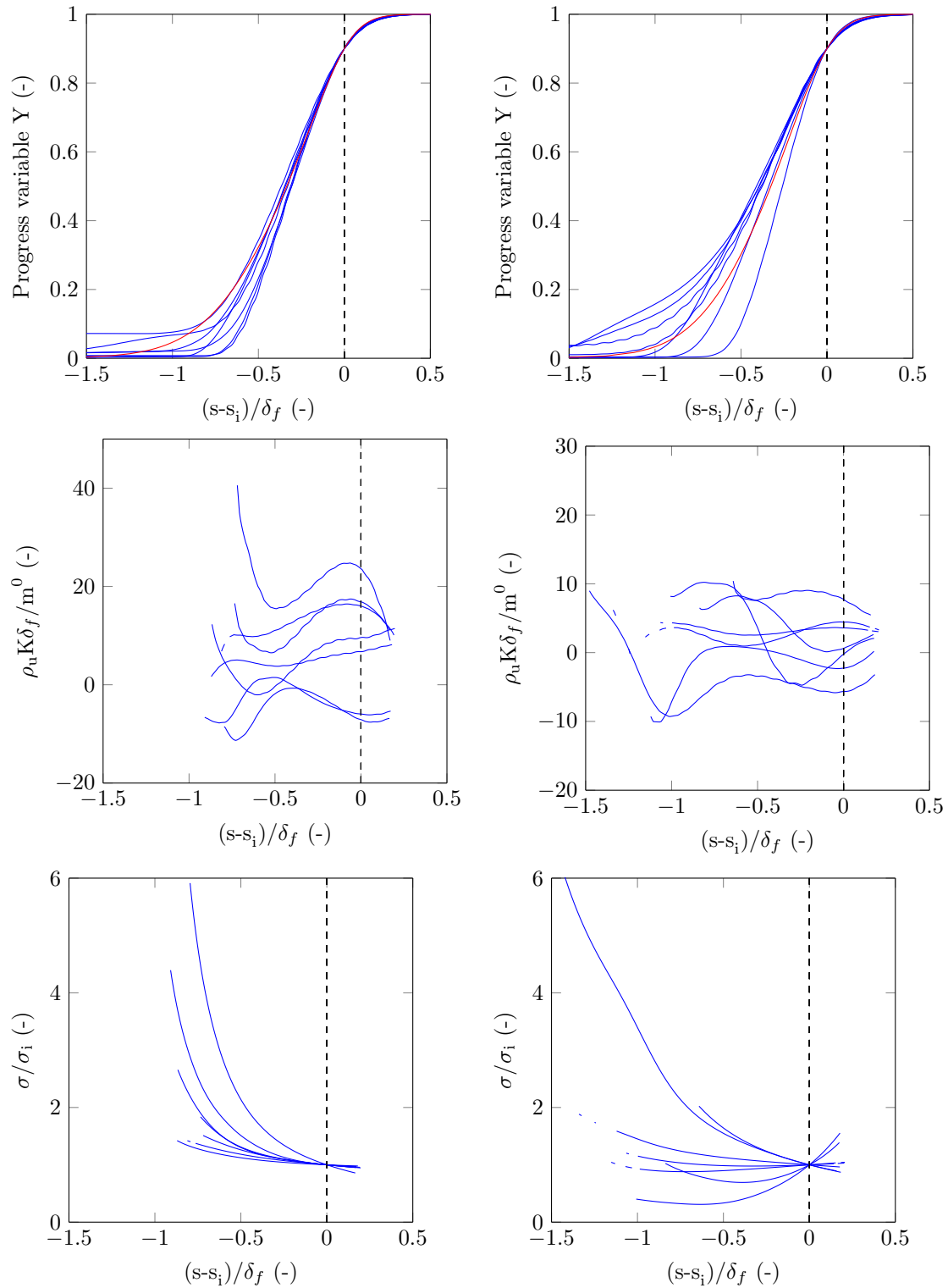
Figure 5.6: Profiles of the progress variable $\mathcal{Y}$, dimensionless stretch rate $\rho_u K \delta_f / m_i^0$ and scaled flame surface area σ/σ_i versus dimensionless flame path $(x - x_i)/\delta_f$. Left: methane-air flame. Right: methane-hydrogen-air flame.

5.6   Mass burning rate of turbulent flames

In this section the influence of flame stretch on the mass burning rate of a turbulent methane-air and methane-hydrogen-air flame is investigated. The sensitivity of the mass burning rate to flame stretch indicates flame stability. The extracted flamelets from case H0-2D and H40-2D, as explained in the previous section, are used. The Karlovitz integral and mass burning rate at the inner layer is determined for each flamelet ($\approx 10^2$).

In Figure 5.7 the dimensionless mass burning rate m_i/m_i^0 is given as function the Karlovitz integral Ka_i. The left side and right correspond respectively to the methane-air and methane-hydrogen-air flame. It shows a clear correlation between Ka_i and m_i/m_i^0. The mass burning rate decreases with positive stretch. When no preferential diffusion is present ($Le = 1$), the theory would predict a slope of -1, $m_i/m_i^0 = 1 - Ka_i$. It is shown that for both flames preferential diffusion effects are present, where the slope can be seen as the Markstein number. The Markstein number $\mathcal{M}$ is computed by performing a square linear fit through all the 2D DNS data points. This results in Markstein number of $\mathcal{M} = 0.69$ and $\mathcal{M} = 0.74$ for the turbulent methane-air flame with respectively the GRI3.0 and DRM19 mechanism. This is in good agreement with the Markstein number of the 1D steady laminar flame of $\mathcal{M} = 0.75$, found in section 5.3.
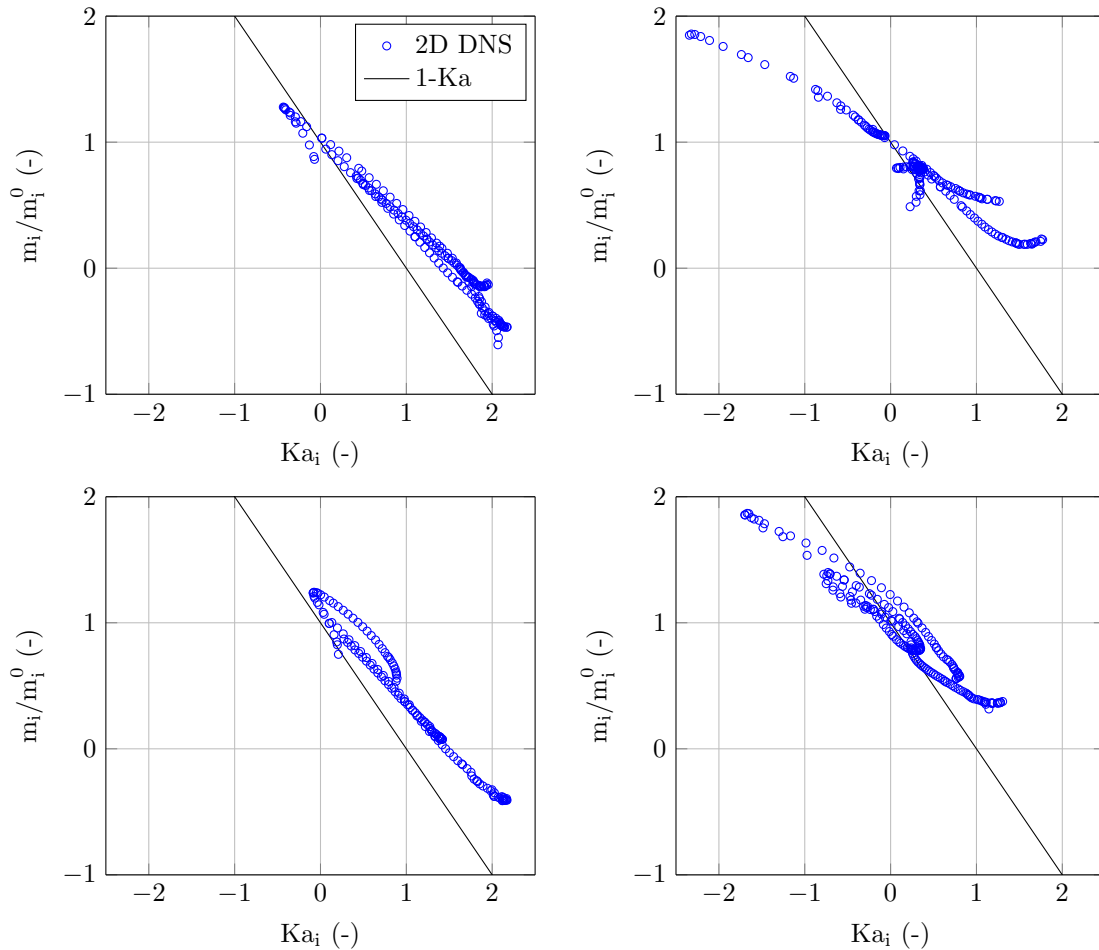

Figure 5.7: mass burning rate m_i/m_i^0 versus stretch at t=1.0 ms. Left: methane-air flame with GRI3.0 and DRM19. Right: methane-hydrogen-air flame with GRI3.0 and DRM19

Table 5.2: Average at t = 1.0 ms

GRI3.0	$X_{H_2} = 0$	$X_{H_2} = 0.4$
$< Ka_i >$	1.27	0.34
$< m_i/m_i^0 >$	0.17	0.78
$\mathcal{M}$	0.69	0.48
DRM19		
$< Ka_i >$	1.03	0.18
$< m_i/m_i^0 >$	0.38	0.89
$\mathcal{M}$	0.74	0.55

Furthermore, Figure 5.7 shows a different slope for the methane-hydrogen-air flames. The Markstein number decreases to $\mathcal{M} = 0.48$ and $\mathcal{M} = 0.55$ for the GRI3.0 and DRM19 mechanism respectively. For all four cases the results are summarized in Table 5.2. Note that the turbulent methane-hydrogen-air flame is more negatively stretched. Consequently, the average mass burning rate m_i/m_i^0 is closer to one. Furthermore, addition of hydrogen does result in a decrease of the Markstein number due to preferential diffusion. As a result the flame stability is reduced compared to the methane-air flame. However, the change in $\mathcal{M}$ appears to be much smaller than in the steady laminar case, where a change of sign in $\mathcal{M} = $ -0.11 is seen. This indicates that the preferential diffusion effects in the turbulent methane-hydrogen-air flame is weaker than in the steady laminar flame. The influence of the highly diffusive specie H_2 is reduced in a turbulent environment. In the turbulent flames, the changes in element mass fraction $\Delta Z_{j,i}$ are smaller than in similar steady laminar flames with the same stretch rate, which is shown in Figure 5.8. It can be seen that the changes in element mass fraction Z_H and Z_C are lower than in the steady laminar flame. This is due to the unsteady behaviour of stretch K and curvature σ in turbulent flames. The methane-hydrogen-air flame is less sensitive for stretch fluctuations than the methane-air flame, due to the lower characteristic flame time-scale $\tau_f = \delta_f/s_L$ [25].
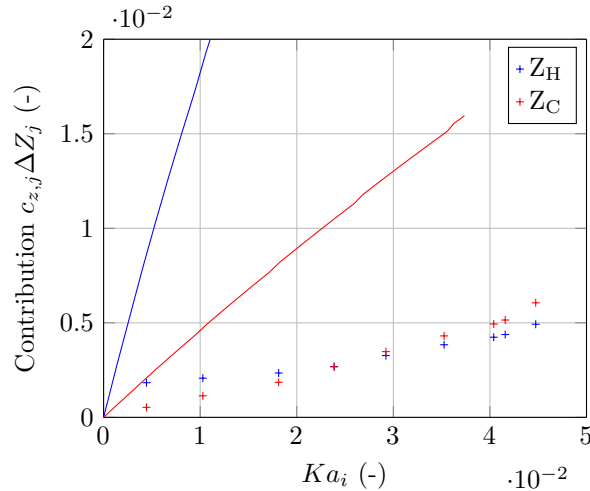
Figure 5.8: Contribution to m_i/m_i^0. Solid line: 1D steady flame. Dots: 2D DNS of H40-2D

In Figure 5.9 the step-response of the laminar methane-hydrogen-air flames subjected to a step-input in stretch rate is given. Initially the flames are unstretched and at $t = 0$ ms the flames are subjected to a stretch rate of $K = 2000$/s, 5000/s and 10000/s. It can be seen that the element mass fractions change with a finite time response. When a flame is subjected to a stretch rate of $K = 5000$/s, it takes the element mass fractions 0.5 flame time scale τ_f before a steady state is reached. However, the finite time response of the flame subjected to a step-input of $K = 2000$/s

is about 1 flame time scale τ_f (t = 1.9 ms). The difference before steady-state values are obtained is partly flow time scale related. This is displayed in right side of Figure 5.9, where the time is made dimensionless by multiplying it with the subjected stretch rate K.
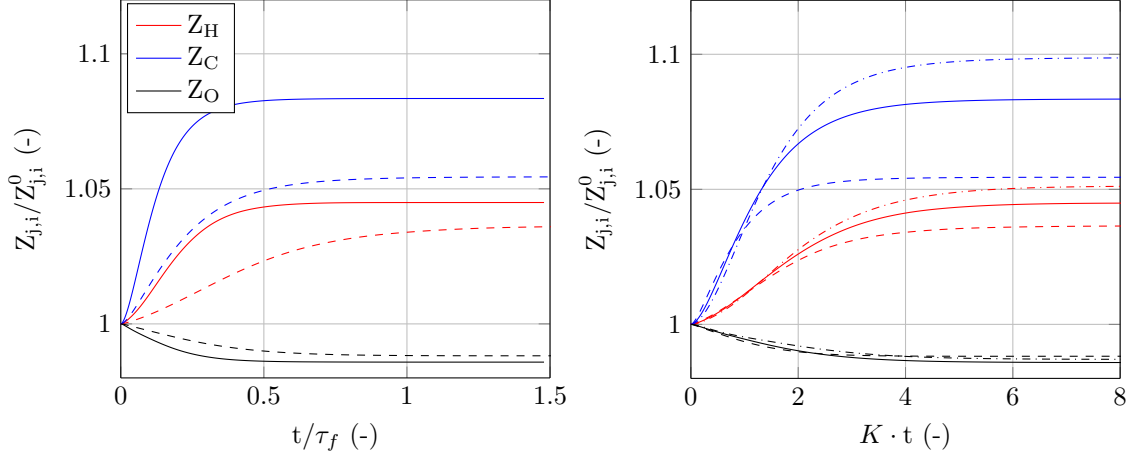

Figure 5.9: Transient response of element mass fraction $Z_{j,i}/Z_{j,i}^0$ in the methane-hydrogen-air flame which is subjected to a step input in stretch rate at $t = 0$ from $K = 0/s$ to 2000/s, 5000/s and 10000/s. Dotted line: K=2000/s. Solid line: K = 5000/s. Dashed-Dotted line: K = 10000/s.

This finite time response of the flame acts as a low pass filter on the changes in element mass fraction. Hence, this transient behaviour in turbulent flames averages out the effect of unsteady stretch rate fluctuations K. In Figure 5.10 the Karlovitz integral is given as function of time for three different points at the flame front of turbulent methane-air flame moving in time with the tangential flame velocity $\vec{v}_{f,||}$. It can be seen that the Karlovitz integral changes, since the stretch K and flame surface area σ are unsteady in the DNS simulations.
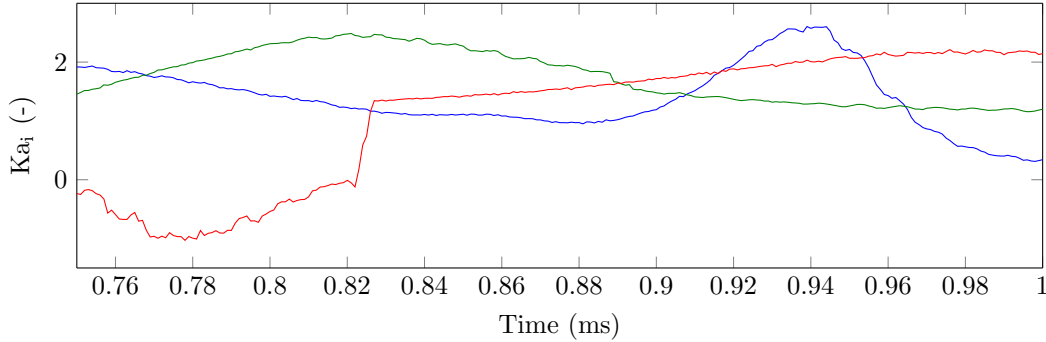
Figure 5.10: The Karlovitz integral for three points moving on the flame front with the tangential flame velocity.

This was also found by De Swart et. al. [12], who performed DNS simulations of lean methane-hydrogenair mixtures with FGM chemistry. They studied three different methanehydrogen ratios in 2D simulations of turbulent flames. A similar stretch analysis was performed as described in this thesis. It was found that Markstein numbers decrease with increasing hydrogen content. Furthermore, they also found a much smaller change in Markstein number than in the steady laminar flames, in line with the results presented in this Chapter. It is shown in theory [4] and by performing simulations [22] of one-dimensional strained flame that preferential diffusion effects

disappear in for high fluctuating strain rates. The general trend is that the flame speed response to strain rate fluctuation reduces as the frequency exceeds the inverse of the characteristic flame time [18]. Note that in Equation 5.13 for $\Delta Z_{j,b}$ the transient response is not included, since the unsteady terms are neglected in the derivation.

Furthermore, the one-dimensional profiles of stretch and curvature are extracted from the 2D DNS results. These profiles in the flamelets are determined based on the normal vector of $\mathcal{Y}$. Normals of other values than $\mathcal{Y}$ do not necessarily follow this same path and therefore differences may arise. Note that in the derivation based on the flamelet equations, all the Q-terms are neglected. In Figure 5.11 the mass fraction H in a high curved part of the H40-2D flame is given. It can be seen that the mass fraction H is focussed in the positively curved region in the flame. In the figure iso-contour levels of $\mathcal{Y}$ from the unburnt to burnt side of the flame are shown. It can be seen that the difference in mass fraction along the iso-contour levels is small compared to difference perpendicular to the iso-contour levels. Therefore, it is expected that the diffusive transport processes along the flame front are small compared to the stretch terms, which justifies the initial assumption to neglect the Q-terms.
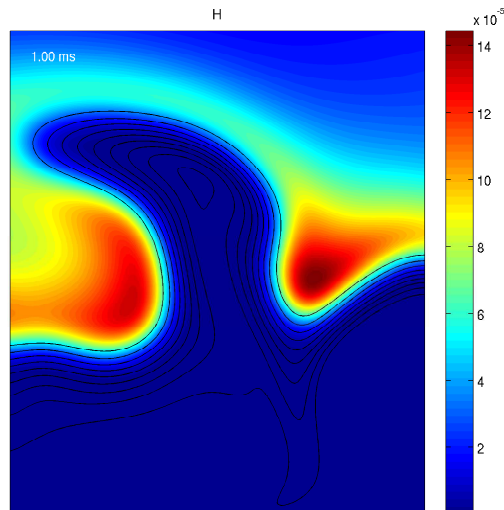
Figure 5.11: Mass fraction Y_H in a part of the H40-2D flame. Black lines: different iso-contour levels of $\mathcal{Y}$ from unburnt to burnt.

Concluding, the addition of hydrogen to methane-air flames results in reduction of the Markstein number. Hence, the methane-hydrogen-air flame becomes less stable for hydrodynamic instabilities. However, the reduction of the Markstein number is much smaller than found in steady laminar flames. This is the result of unsteady stretch and curvature effects in turbulent flames, where these rates vary a lot as function of time at the flame front. When these variables change in time, the element mass fractions follows with a finite response time. Therefore, the change in element mass fraction is less in turbulent methane-hydrogen-air flame compared to steady 1D flame at a similar stretch rate. As a result, preferential diffusion effects are reduced and the turbulent flame is more stable compared to the 1D steady flame.

Chapter 6

Conclusion and Recommendations

In this thesis the effects of flame stretch in combination with preferential diffusion were studied on hydrogen addition to turbulent methane-air flames. Direct numerical simulations have been used to study the effects of hydrogen addition on lean premixed methane-air flames. The simulations are performed for a methane-air flame and a methane-hydrogen-air flame with 40% hydrogen on volume basis. A detailed chemistry is used in the simulations in order to include the diffusion rates of each specie.

It is shown that flame stretch and preferential diffusion causes a local redistribution of enthalpy and species. This effects the local stoichiometry and temperature. Hydrogen is a highly diffusive specie (Le $<<$ 1). This is seen in 1D simulations where the hydrogen-enriched flame encounters a preferential diffusion effect of hydrogen. However, in methane-air flame it was seen that preferential diffusion effect are small. The results of the flame-turbulence interaction in DNS showed local focusing of H_2 concentrations in the regions convex toward the reactants of the turbulent methane-hydrogen-air flame and defocussing in regions concave toward the reactants. In addition, preferential diffusion effects were shown to enhance curvature of the flame front. It was shown that this results in locally richer mixture and enhanced turbulent burning velocity per unit area. This effect is amplified in case of higher turbulent intensity.

Owing to higher flame temperatures, the NO emission are higher in the laminar methane-hydrogen-air flame. Comparing the amount of NO production at the burnt side of the turbulent flame to the amount of NO at the burnt side of the laminar flame showed on average a similar amount in the methane-air flame. However, an increase in NO production was found at the burnt side of the turbulent methane-hydrogen-flame relative the laminar flame. Increasing the turbulent intensity resulted in even higher production rates. It is shown that NO emissions are influenced by local differences in temperature and radical concentrations, which is enhanced due to preferential diffusion. It was observed that the peak levels of NO production in the hydrogen-enriched flame are located in areas of positive curvature. It was found that the on average 12% more NO is produced per unit area over time in the methane-hydrogen-flame relative to the methane-air flame. Increasing the turbulent intensity results in 50% more NO production per unit area for the methane-hydrogen-air flame compared to the methane-air flame.

However, in this thesis the equivalence ratio is fixed at $\phi = 0.7$. The methane-hydrogen-air flame potentially allows leaner combustion at lower equivalence ratio's, which leads to lower flame temperatures and thus lower NO emissions [15, 39]. Therefore, for future research it is recommended to perform numerical simulations of hydrogen-enriched flames closer to their lean flammability limit. Furthermore, in the gas-turbine applications the flames encounter elevated pressures which most change the way of NO production pathways. The NO formation due to thermal NO becomes more dominant [14]. It is suggested to perform calculations at gas turbine operating conditions.

Flame stability was studied in terms of sensitivity of the mass burning rate to flame stretch. Without preferential diffusion effects, the mass burning rate decreases with positive flame stretch, which corresponds to a Markstein number of one. This counteracts the hydrodynamics instability and results in a stable flame. For weak stretch, it was possible to predict the stretched mass burning rate as function of the Karlovitz integral and the unstretched mass burning rate. It was observed that changes in enthalpy and element mass fraction ΔZ_j have an impact on the response of the mass burning rate to a stretch. It was found that changes in element mass fraction ΔZ_h and ΔZ_c have largest influence on the sensitivity of the mass burning rate to flame stretch. In case of the laminar methane-air flame, a stable flame was found. However, in the stretched 1D methane-hydrogen-air flame it was seen that the preferential diffusion effects are larger than the direct stretch effect. This result in an unstable flame. Furthermore, it was found that the hydrogen-enriched flame was more resistant to extinction due to downstream interaction.

To compare the flame stability of laminar flames with the stability of turbulent flames, one-dimensional profiles of stretch and curvature are extracted from the two-dimensional DNS study. The Karlovitz integral is calculated based on the strong stretch theory introduced by de Goey and ten Thije Boonkkamp [8]. It was found that the addition of hydrogen to methane-air flames makes the flame less sensitive to flame stretch, leading to a reduction of the Markstein number. Hence, the stabilizing effect of flame stretch is reduced in the methane-hydrogen-air flame. However, the reduction of the Markstein number is much smaller than found in the steady laminar flame. It was shown that changes in element mass fraction ΔZ_h and ΔZ_c are reduced in turbulent methane-hydrogen-air flame compared to the steady 1D flame at a similar stretch rate. This is the result of a finite time response of the element mass fractions in the turbulent flame on the fluctuating stretch rates. As a result, preferential diffusion effects are reduced and the turbulent flame is more stable compared to the one-dimensional steady flame.

Further research should include also the effect of hydrogen-addition on the flame stability and mass burning rate for increasing turbulent intensities. It is possible that the preferential diffusion effects will vanish in a high turbulent environment. For the higher turbulent intensity case in this study, it was not possible to obtain isolated flamelets. Furthermore, the Markstein number is not a property of the mixture, but depends on the flow. Therefore, it is recommended to perform further research in a geometry closer to a gas turbine combustor.

Bibliography

[1] S. Gordon B. McBride and M.A. Reno. *Coefficients for Calculating Thermodynamic and Transport Properties of Individual Species.* National Aeronautics and Space Administration, Glenn Research Center, 1993. 12, 13

[2] R. Bastiaans, L Somers, and H de Lange. Innovation and intellectual property rights. *Modern simulation strategies for turbulent flow*, 2001. iii, 21

[3] S.H. Chung and C.K. Law. An invariant derivation of flame stretch. *Combustion and Flame*, 55:123–125, 1984. 8

[4] P. Clavin and G. Joulin. High-frequency response of premixed flames to weak stretch and curvature: a variable-density analysis. *Combustion Theory and Modelling*, 1(4):429–446, 1997. 59

[5] R. Courant, K.O. Friedrichs, and H. Lewy. *On the partial difference equations of mathematical physics.* Leopold Classic Library, 1956. 24

[6] G Darrieus. Propagation d'un front de flamme. *La Technique Moderne and Congrs de Mcanique Applique Paris*, 1938. 52

[7] L.P.H. de Goey and Thije Boonkkamp. A flamelet description ofpremixed laminar flames and the relation with flame stretch. *Combustion and Flame*, 119:253–271, 1999. 47, 48, 49, 54

[8] L.P.H. de Goey and Thije and Boonkkamp. A mass-based definition of flame stretch for flames of finite thickness. *Combustion Science and Technology*, 122:399–405, 1997. 3, 8, 47, 62

[9] L.P.H. de Goey, R.T.E. Hermanns, and R.J.M. Bastiaans. Analysis of the asymptotic structure of stoichiometric premixed CH4H2air flames. *Proceedings of the Combustion Institute*, 31:1031–1038, 2007. 18, 47, 49

[10] H. C de Lange. Acoustic upwinding for sub- and super-sonic turbulent channel flow at low Reynolds number. *International Journal for Numerical Methods in Fluids*, 55:205–223, 2007. 22

[11] J.A.M. de Swart. *Modeling and analysis of flame stretch and preferential diffusion in premixed flames.* PhD thesis, Technische Universiteit Eindhoven, 2009. 1, 8, 9, 40, 52, 53

[12] Joost A. M. de Swart, Rob J. M. Bastiaans, Jeroen A. van Oijen, L. Philip H. de Goey, and R. Stewart Cant. Inclusion of preferential diffusion in simulations of premixed combustion of hydrogen/methane mixtures with flamelet generated manifolds. *Flow, Turbulence and Combustion*, 85(3):473–511, Dec 2010. 59

[13] C.P. Fenimore. Formation of nitric oxide in premixed hydrocarbon flames. *Symposium (International) on Combustion*, 1970. 14

[14] Felix Gthe Fernando Biagioli. Effect of pressure and fuelair unmixedness on nox emissions from industrial gas turbine burners. *Combustion and Flame*, 151:274–288, 2007. 61

[15] J.L. GAUDUCHEAU, B. DENET, and G. SEARBY. A numerical study of lean ch4/h2/air premixed flames at high pressure. *Combustion Science and Technology*, 137(1-6):81–99, 1998. 1, 61

[16] GRA Groot. *Modelling of propagating spherical and cylindrical premixed flames*. PhD thesis, Technische Universiteit Eindhoven, 2003. iii, 21

[17] G.R.A. Groot and L.P.H. de Goey. A computational study on propagating spherical and cylindrical premixed flames. *Proc. Combust. Inst.*, 29:1445–1451, 2002. 49

[18] Hong G. Im and Jacqueline H. Chen. Effects of flow transients on the burning velocity of laminar hydrogen/air premixed flames. *Proceedings of the Combustion Institute*, 28(2):1833 – 1840, 2000. 60

[19] F. Leon Ballard Adolfo Banti John D. Morris, Richard A. Symond. Combustion aspects of application of hydrogen and natural gas fuel mixtures to ms9001e dln-1 gas turbines. *ASME 1998 International Gas Turbine and Aeroengine Congress and Exhibition*, 3(98), 1998. 1

[20] F. Leon Ballard Adolfo Banti John D. Morris, Richard A. Symond. Enhanced gas turbine combustor performance using h2-enriched natural gas. *ASME 1998 International Gas Turbine and Aeroengine Congress and Exhibition*, 1999. 1

[21] A. Kazakov and M. Frenklach available at `http://www.me.berkeley.edu/drm/`. 14, 18, 21

[22] Omar M. Knio and Habib N. Najm. Effect of stoichiometry and strain rate on transient flame response. *Proceedings of the Combustion Institute*, 28(2):1851 – 1857, 2000. 59

[23] L. D Landau. On the theory of slow combustion. *Acta Physicochim*, 1944. 52

[24] S.K. Lele. Compact finite difference schemes with spectral-like resolution. *Journal of Computational Physics*, 103:16–42, 1992. 22

[25] Tim C. Lieuwen. *Unsteady Combustor Physics*. Georgia Institute of Technology, 2012. 39, 40, 58

[26] J.A. Oijen, A. Donini, R.J.M. Bastiaans, J.H.M. ten Thije Boonkkamp, and L.P.H. de Goey. State-of-the-art in premixed combustion modeling using flamelet generated manifolds. *Progress in Energy and Combustion Science*, 57:30–74, 2016. 1, 9, 11, 18, 47, 48, 50

[27] I. Cohen P. Kundu. *Fluid Mechanics*. Elsevier Science, 1990. 26, 33, 34

[28] N Peters. *Turbulent Combustion*. Cambridge University Press, 2000. 7, 27, 48, 55

[29] Evatt R. Hawkes and Jacqueline H. Chen. Direct numerical simulation of hydrogen-enriched lean premixed methane-air flames. *Combustion and Flame*, 138:242–258, 2004. 33, 34

[30] W. J.S. Ramaekers, J. A. van Oijen, and L. P.H. de Goey. Stratified turbulent bunsen flames: flame surface analysis and flame surface density modelling. *Combustion Theory and Modelling*, 16(6):943–975, 2012. 42

[31] J.-Y. Ren, F. N. Egolfopoulos, and T. T. Tsotsis. No x emission control of lean methane-air combustion with addition of methane reforming products. *Combustion Science and Technology*, 174(4):181–205, 2002. 1

[32] Ramanan Sankaran, Evatt R. Hawkes, Jacqueline H. Chen, Tianfeng Lu, and Chung K. Law. Structure of a spatially developing turbulent lean methane-air Bunsen flame. *Proceedings of the Combustion Institute*, 31:1291–1298, 2007. 31, 34

[33] Zhu Shengrong and Acharya Sumanta. Effects of hydrogen addition on swirl-stabilized flame properties. *ASME Turbo Expo 2010: Power for Land, Sea, and Air*, 2, 2010. 34

[34] Gregory P. Smith, David M. Golden, Michael Frenklach, Nigel W. Moriarty, Boris Eiteneer, Mikhail Goldenberg, C. Thomas Bowman, Ronald K. Hanson, Soonho Song, William C. Gardiner, and Vitali V. Lissianski Jr., and Zhiwei Qin available at `http://www.me.berkeley.edu/gri_mech/`. 13, 21

[35] Bart Somers. *The Simulation of Flat Flames with Detailed and Reduced Chemical Models.* PhD thesis, Technische Universiteit Eindhoven, 1994. 2, 13, 16, 18, 21, 24, 47

[36] R. Stephen Turns. *An Introduction to Combustion: concepts and applications.* McGraw-Hill, 2000. 44

[37] J. van Oijen, R. Bastiaans, and L. de Goey. Low-dimensional manifolds in direct simulations of premixed turbulent flames. *Proceedings of the Combustion Institute*, 31:1377–1384, 2007. iii, 21

[38] A.W. Vreman, J.A. van Oijen, L.P.H. de Goey, and R.J.M. Bastiaans. Direct numerical simulation of hydrogen addition in turbulent premixed Bunsen flames using flamelet-generated manifold reduction. *International journal of hydrogen energy*, 34:2778–2788, 2009. 1, 18, 34, 53

[39] J. Warnatz, U. Maas, and R.W. Dibble. *Combustion.* Springer, 1996. chap. 17. 13, 14, 18, 43, 61

[40] F.A. Williams. *Combustion theory.* Addison-Wesley, 1985. 1

[41] Zhen Zhou, Francisco Hernndez-Prez E., Yuriy Shoshin, Jeroen A. van Oijen, and Laurentius P.H. de Goey. Effect of soret diffusion on lean hydrogen/air flames at normal and elevated pressure and temperature. *Combustion theory and modelling*, 2017. 17